

1225-0767(ISSN Print)
2287-6715(ISSN Online)
한국연구재단 우수등재학술지

Journal of Ocean Engineering and Technology

Vol. 37, No. 6 (Serial Number 175)

December 2023

한국해양공학회지



www.joet.org



The Korean Society of Ocean Engineers

Editor-in-Chief

Choung, Joonmo Inha University, Korea

Editorial Board

Incecik, Atilla	University of Strathclyde, UK	Lee, Woo Dong	Gyeongsang National University, Korea
Jeffrey Harris	Ecole des Ponts ParisTech, France	Li, Binbin	Tsinghua University, China
Jeong, Byongug	University of Strathclyde, UK	Li, Chun Bao	Whuhan University of Technology, China
Jin, Chungkuk	Florida Institute of Technology, USA	Lim, Youngsub	Seoul National University, Korea
Kang, Hooi-Siang	Universiti Teknologi Malaysia, Malaysia	Oterkus, Erkan	University of Strathclyde, UK
Kim, Do Kyun	Seoul National University, Korea	Park, Hyoungsu	University of Hawaii at Manoa, USA
Kim, Jinwhan	Korea Advanced Institute of Science and Technology, Korea	Park, Jong Chun	Pusan National University, Korea
Kim, Kwon-Hoo	Pukyong National University, Korea	Shin, Sungwon	Hanyang University, Korea
Kim, Moo Hyun	Texas A&M University, USA	Srinil, Narakorn	Newcastle University, UK
Kim, Sang Jin	National Sun Yat-sen University, Taiwan	Tayyar, Gökhan Tansel	Istanbul Technical University, Türkiye
Kim, Taeseong	Technical University of Denmark, Denmark	Yu, Zhaolong	Norwegian University of Science and Technology, Norway
Koo, Weoncheol	Inha University, Korea		

Journal Publication Committee

Ahn, Seokhwan	Jungwon University, Korea	Kim, Seungjun	Korea University, Korea
Bae, Yoon Hyeok	Hongik University, Korea	Kim, Yeon-Joong	Korea Environment Institute, Korea
Cho, Gyeung	Tongmyong University, Korea	Kim, Yeulwoo	Pukyong National University, Korea
Choi, Seongim	Gwangju Institute of Science and Technology, Korea	Kim, Younghun	Kyungnam University, Korea
Choi, Sung-Woong	Gyeongsang National University, Korea	Lee, Jooyong	Gyeongsang National University, Korea
Do, Kideok	Korea Maritime and Ocean University, Korea	Lee, Kangsu	Korea Research Institute of Ships & Ocean Engineering, Korea
Ham, Seung-Ho	Changwon National University, Korea	Lee, Tak Kee	Gyeongsang National University, Korea
Jeong, Se-Min	Chosun University, Korea	Nam, Bo Woo	Seoul National University, Korea
Jung, Dongho	Korea Research Institute of Ships & Ocean Engineering, Korea	Paik, Kwang-Jun	Inha University, Korea
Kang, Choonghyun	Gyeongsang National University, Korea	Seo, Jung Kwan	Pusan National University, Korea
Kang, TaeSoon	GeoSystem Research Corp., Korea	Song, Chang Yong	Mokpo National University, Korea
Kim, Hyun-Sik	Tongmyong University, Korea	Woo, Joohyun	Korea Maritime and Ocean University, Korea
Kim, Jeong-Hwan	Dong-A University, Korea	Yoon, Hyeon Kyu	Changwon National University, Korea

Research Ethics Committee

Kim, Jinwhan	Korea Advanced Institute of Science and Technology, Korea	Lee, Jin Ho	Pukyong National University, Korea
Kim, Joon-Young	Korea Maritime and Ocean University, Korea	Lee, Kangsu	Korea Research Institute of Ships & Ocean Engineering, Korea
Ko, Jae-Yong	Mokpo National Maritime University, Korea		

Published on December 31, 2023
Published by The Korean Society of Ocean Engineers (KSOE)
Room 1302, 13, Jungang-daero 180beon-gil, Dong-gu, Busan, 48821, Korea
TEL: +82-51-759-0656 FAX: +82-51-759-0657 E-mail: ksoehj@ksoe.or.kr URL: http://www.ksoe.or.kr
Printed by Hanrimwon Co., Ltd., Seoul, Korea E-mail: hanrim@hanrimwon.co.kr
ISSN(print) 1225-0767 **ISSN(online)** 2287-6715

This journal was supported by the Korean Federation of Science and Technology Societies (KOFST) grant funded by the Korean government.

© 2023 by The Korean Society of Ocean Engineers (KSOE)

This is an open access article distributed under the terms of the creative commons attribution non-commercial license (<http://creativecommons.org/licenses/by-nc/4.0>) which permits unrestricted non-commercial use, distribution, and reproduction in any medium, provided the original work is properly cited.

Journal of Ocean Engineering and Technology

한국해양공학회지

CONTENTS

Volume 37, Number 6

December, 2023

<Original Research Articles>

- CFD Study for Wave Run-up Characteristics Around a Truncated Cylinder with Damper
Zhenhao Song and Bo Woo Nam 225
- Dynamic Behavior Assessment of OC4 Semi-submersible FOWT Platform Through Morison Equation
Chungkuk Jin, Ikjae Lee, JeongYong Park and MooHyun Kim 238
- Point Cloud-Based Spatial Environment Development for Near Real-Time Erection Simulation in Shipyards
Yeon-Jun Kim, SeungYeol Wang, Jaewon Jang, Bon-Yeong Park, Dong-Kun Lee and Daekyun Oh 247
- Numerical Method for Calculating Fourier Coefficients and Properties of Water Waves with Shear Current and Vorticity in Finite Depth
JangRyong Shin 256

<Technical Article>

- Economic Feasibility Analysis According to Seam Location of Ship Pieces
Hyun-Seong Do and Tak-Kee Lee 266
- Structural Response Analysis for Multi-Linked Floating Offshore Structure Based on Fluid-Structure Coupled Analysis
Kichan Sim, Kangsu Lee and Byoung Wan Kim 273

<Corrigendum>

- Corrigendum to: Investigation of Applying Technical Measures for Improving Energy Efficiency Design Index (EEDI) for KCS and KVLCC2
Jun-Yup Park, Jong-Yeon Jung and Yu-Taek Seo 282

GENERAL INFORMATION

The “**Journal of Ocean Engineering and Technology**” (JOET) was launched in 1987 and is published bimonthly in February, April, June, August, October, and December each year by “The Korean Society of Ocean Engineers (KSOE).” Its ISO abbreviation is “J. Ocean Eng. Technol.” JOET publishes original research articles, technical articles, and review articles on all aspects of ocean engineering, including experimental, theoretical, numerical, and field observations. All manuscripts undergo peer-review by two or more reviewers.

The scope of JOET encompasses the following research areas:

- **Ships and offshore engineering:**

Design of ships and offshore structures; Resistance and propulsion; Seakeeping and maneuvering; Experimental and computational fluid dynamics; Ocean wave mechanics; Fatigue strength; Plasticity; Optimization and reliability; Arctic technology and extreme mechanics; Noise, vibration, and acoustics; Concrete engineering; Thermodynamics and heat transfer; Hydraulics and pneumatics; Autonomous and unmanned ship; Greenship technology; Digital twin of ships and offshore structures; Marine materials

- **Coastal engineering:**

Coastal, port, and harbor structures; Waves transformation; Coastal and estuary hydrodynamics; Sediment transport and morphological change; Subsea geotechnics; Coastal groundwater management; Prevention or mitigation of coastal disaster; Coastal zone development and management; Shore protection technique; Coastal environmental process; Beach safety

- **Ocean energy engineering:**

Offshore wind turbines; Wave energy platforms; Tidal current energy platforms; Floating photovoltaic energy platform; Small modular reactor; Combined energy platforms

- **Marine robot engineering:**

Robot sensor system; Autonomous navigation; Robot equipment; Marine robot control; Environment mapping and exploration; Underwater communication and networking; Design of marine robots

JOET is an open-access journal distributed under the terms of the creative commons attribution non-commercial license. It is indexed in databases such as the Korean Citation Index (KCI), Google Scholar, Science Central, Korea Science, and the Directory of Open Access Journals (DOAJ). JOET offers PDF or XML versions for free on its website (<https://www.joet.org>). For business matters, authors need to contact KSOE Secretariat by email or phone (e-mail: ksoehj@ksoe.or.kr or Tel: +82 51 759 0656). Correspondences for publication matters can be asked via email to the Editor-in-Chief (e-mail: heroeswise2@gmail.com).

CFD Study for Wave Run-up Characteristics Around a Truncated Cylinder with Damper

Zhenhao Song¹ and Bo Woo Nam²

¹Graduate Student, Department of Naval Architecture and Ocean Engineering, Seoul National University, Seoul, Korea

²Professor, Department of Naval Architecture and Ocean Engineering, Seoul National University, Seoul, Korea

KEYWORDS: Wave run-up, CFD, Truncated cylinder, Damper, Stokes waves, Volume of fluid

ABSTRACT: In this study, numerical simulations for a single fixed truncated circular cylinder in regular waves were conducted to investigate the nonlinear wave run-up under various dampers and wave period conditions. The present study used the volume of fluid (VOF) technique to capture the air-water interface. The unsteady Reynolds-averaged Navier-Stokes (URANS) equation with the $k-\epsilon$ turbulence model was solved using the commercial computational fluid dynamics (CFD) software STAR-CCM+. First, a systematic spatial convergence study was conducted to assess the performance and precision of the present numerical wave tank. The numerical scheme was validated by comparing the numerical results of wave run-up on a bare truncated cylinder with the experimental results, and a good agreement was achieved. Then, a series of parametric studies were carried out to examine the wave run-up time series around the truncated cylinder with single and dual dampers in terms of the first- and second-order harmonic and mean set-up components. Additionally, the local wave field and the flow velocity vectors adjacent to the cylinder were evaluated. It was confirmed that under short wave conditions, the high position of the damper led to a noticeable increase in the wave run-ups with significant changes in the first- and second-order harmonic components.

1. Introduction

The offshore wind energy industry has undergone rapid and substantial growth, marking a significant expansion over the past decades. Forecasts from reputable sources indicate that the global offshore wind energy sector has the potential to reach a capacity range of 380 GW to 394 GW by the year of 2032, which would represent a six-fold increase in offshore wind capacity over the next decade (Musial et al., 2023). Nowadays, platform developers prefer to select deep-water regions (over 60 meters) to install floating offshore wind turbines (FOWTs) because of the abundant wind resources. On the other hand, the harsh environment in deep water regions may pose a risk to offshore structures. Therefore, depending on the installation site, various floating offshore structures, such as semi-submersible platforms, tension leg platforms (TLPs), and spar platforms, have been considered as supporting structures for FOWTs. Among these options, approximately 80% of projects plan to use semi-submersible platforms (Musial et al., 2023). In general, these platforms are primarily supported by large columns, and dampers are commonly attached to the bottom of the FOWT to improve motion performance. The

cylindrical columns typically generate significant diffraction effects when exposed to incident waves, which rapidly amplify local free-surface elevation around these cylindrical structures. Platform designers must consider two principal localized free surface effects based on this phenomenon: air gap and wave run-up (Morris-Thomas and Thiagarajan, 2004).

According to the DNV-RP-C103 (DNV GL, 2015), the air gap indicates the distance between the highest wave crest and the bottom of the deck box. The design of offshore platforms must satisfy the criteria for a sufficient air gap so that the maximum height of the wave run-up can always be maintained below the platform deck. A 1.5-meter margin is commonly suggested as the critical value for the air gap (API, 2001). An insufficient air gap may induce wave impact or ingress on the deck and upper structures. On the other hand, an excessive air gap may increase fabrication costs and decrease the stability of the offshore platform (Morris-Thomas and Thiagarajan, 2004). The wave run-up is induced by the rapid amplification of the local free surface elevation due to the interaction between the incident waves and the columns of offshore platforms. When an incident wave impinges on the column, it undergoes a significant transformation,

Received 27 September 2023, revised 26 October 2023, accepted 28 October 2023

Corresponding author Bo Woo Nam: +82-2-880-7324, bwnam@snu.ac.kr

© 2023, The Korean Society of Ocean Engineers

This is an open access article distributed under the terms of the creative commons attribution non-commercial license (<http://creativecommons.org/licenses/by-nc/4.0>) which permits unrestricted non-commercial use, distribution, and reproduction in any medium, provided the original work is properly cited.

where the momentum of incident waves in the vertical direction (upward) increases instantaneously. Finally, this extra momentum flux transforms into a rapid wave amplification at the interaction point between the wave and body surfaces.

The wave run-up problem of offshore structures is an important issue that platform designers focus on because the precise predictions of this phenomenon are crucial for the air gap requirement. In particular, many studies have investigated the wave run-up problems around a truncated cylinder using experimental and numerical methods. Regarding numerical simulations, potential flow analysis has been widely used to predict wave run-up and wave impact. Havelock (1940), who used an analytical solution based on linear wave theory, conducted the earliest studies on the wave-body diffraction problem around a truncated cylinder in deep water. Omer and Hall (1949) and MacCamy and Fuchs (1954) extended Havelock's work to shallow and arbitrary water depths, respectively. Morris-Thomas and Thiagarajan (2004) conducted a model test and potential flow calculations to discuss the wave run-up on a fixed truncated cylinder with zeroth-, first-, second-, and third-order harmonic analysis in monochromatic progressive waves. They reported that distinct nonlinear effects should be predicted by high-order diffraction theory in long waves. On the other hand, compared to potential analysis, computational fluid dynamics (CFD) simulations could provide more accurate predictions of wave run-up by considering both nonlinear and viscous effects. Numerous scholars have conducted CFD simulations on the wave diffraction problem of a truncated circular cylinder. Kim et al. (2011) proposed a hybrid numerical wave tank (NWT) model by matching the potential far-field wave solutions and near-field CFD solutions based on the ALE finite-element method (FEM). The simulation results of wave run-up showed good agreement with the model test data. Koo et al. (2014) applied the commercial CFD code STAR-CCM+ to investigate the wave run-up height and depression depth around a circular cylinder under various Froude numbers (Fn). Mohseni et al. (2018) conducted a CFD simulation using OpenFOAM to investigate the physics of wave scattering and wave run-up around a truncated cylinder, considering various wave steepness. They reported that the formation of lateral edge waves becomes more significant with high-steepness waves.

In offshore engineering, various dampers are commonly attached to the base of the supporting column to improve the motion performance of FOWTs. Semi-submersible FOWT platforms, including WindFloat (Roddier et al., 2010), OC4-DeepCWind (Robertson et al., 2014), Tri-floater (Lefebvre and Collu., 2012), and Dutch Tri-floater (Huijs et al., 2014), all share a common design feature. They are composed of three circular truncated cylinders which are attached with the dampers. In addition to the improvement of the motion response, the presence of dampers also amplifies the wave run-up, which is undesirable.

The present study examined the effects of various types of dampers on the nonlinear wave run-up around a fixed truncated cylinder by conducting a series of CFD simulations. Section 2 describes the numerical method to construct a numerical wave tank (NWT) with a

truncated circular cylinder in regular waves. Section 3 assesses the accuracy of the present numerical scheme, and a spatial convergence study was performed based on the Grid Convergence Index (GCI) method. The validity of the present NWT was confirmed by comparing the wave run-up around a bare truncated cylinder with existing experimental results (Nam et al., 2008). Section 4 discusses the effect of three types of dampers on the wave run-ups around a truncated cylinder. The changes in the first- and second-order harmonic components and mean values of the wave run-up were analyzed, respectively.

2. Numerical Method

2.1 Numerical Method

Wave run-up around a truncated cylinder with various dampers was numerically analyzed. The numerical simulations were conducted with the CFD software STAR-CCM+ (Ver.15.04.008). The governing equations consist of a continuity equation (Eq. (1)) and a three-dimensional momentum equation, assuming air and water are incompressible viscous Newtonian fluids. The unsteady Reynolds-averaged equation of Navier-Stokes equation (URANS) is expressed as Eq. (2):

$$\frac{\partial(\rho u_i)}{\partial x_i} = 0 \quad (1)$$

$$\frac{\partial u_i}{\partial t} + \frac{\partial(u_i u_j)}{\partial x_j} = -\frac{1}{\rho} \frac{\partial P}{\partial x_i} + \frac{\partial}{\partial x_j} \left[\frac{\mu}{\rho} \left(\frac{\partial u_i}{\partial x_j} + \frac{\partial u_j}{\partial x_i} \right) \right] + g - \frac{\partial(\overline{u'_i u'_j})}{\partial x_j} \quad (2)$$

where u_i and x_i denote the fluid velocity and coordinate component in the i^{th} direction, respectively. P is the fluid pressure, and ρ is the fluid density. g is the gravitational acceleration. u'_i denotes the fluctuating velocity component in the i^{th} direction and μ is the turbulent viscosity. The $k-\epsilon$ turbulence model was used, and the volume-of-fluid (VOF) method was applied to capture the interface of multiphase flow. Regarding the CFD simulation, the finite volume method (FVM) was used to solve the RANS equations and VOF transport equation. A second-order implicit unsteady scheme was used for temporal discretization. The time step was chosen as 1/1000 of the incident wave period (T_n) to ensure the Courant number was below 0.1 (Perić and Abdel-Maksoud, 2018).

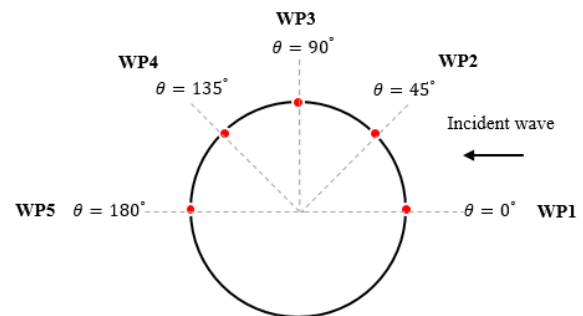


Fig. 1 Position of wave probes on the truncated cylinder

2.2 Grid System and Analysis Method

A truncated cylinder model with a scale ratio of 50.314 was selected for this study, matching the experimental model used by Nam et al. (2008) in their model test. During the test, five wave probes were attached to the surface of the truncated cylinder. These wave probes were positioned at 0° , 45° , 90° , 135° , and 180° with respect to the direction of the incident wave. Fig. 1 presents the top view of the wave probes.

Fig. 2 shows the computational domain and boundary conditions.

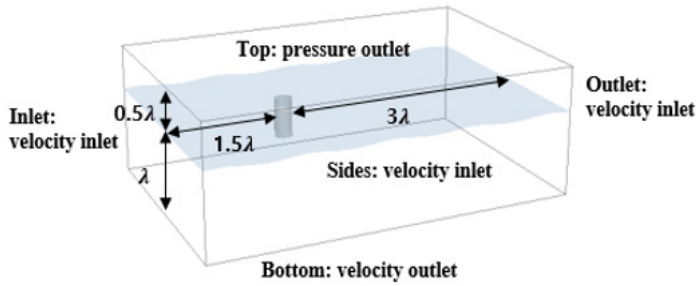


Fig. 2 Computational domain and boundary conditions

The length and width of the entire computational domain were 4.5 times the wavelength and 1.5 times the wavelength, respectively. The water depth was set to one wavelength to approximate the deep-water condition. The computational domain was divided into two parts: an inner zone to examine the physics of wave run-up and a forcing zone to ensure accurate wave generation upstream and prevent reflected waves at the boundaries. The length of the forcing zone is twice the wavelength in the downstream and half the wavelength in the upstream and the lateral boundaries, respectively. Fig. 3 presents the side view

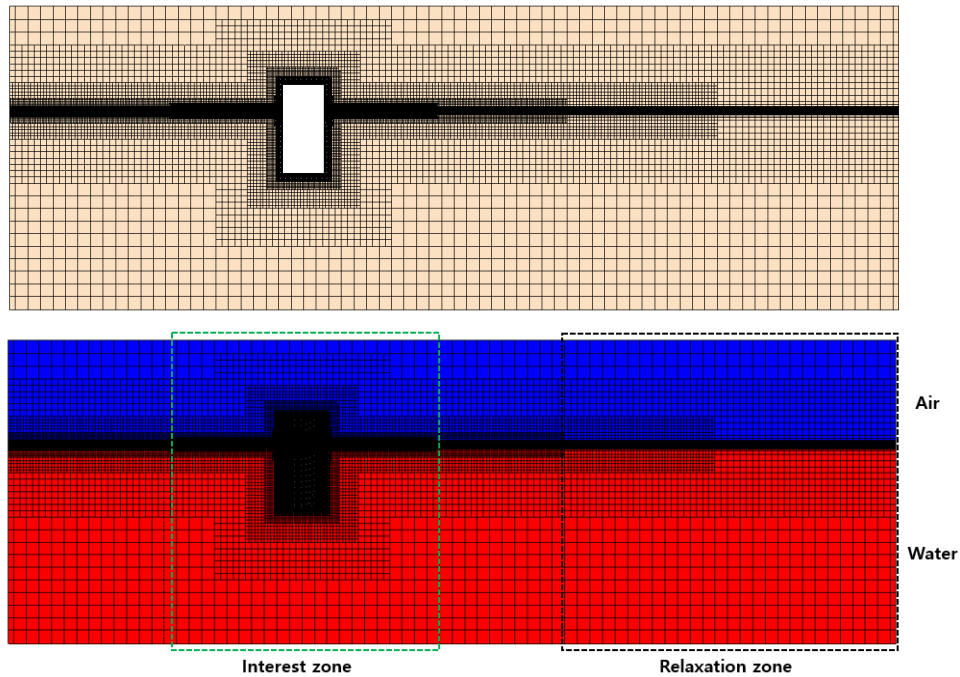
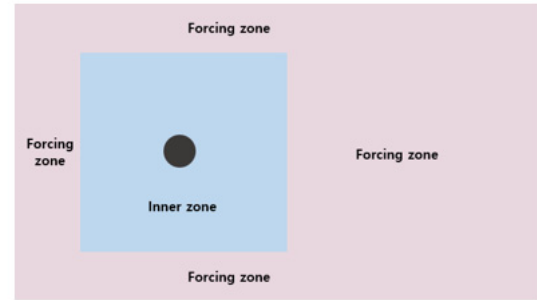


Fig. 3 Grid system

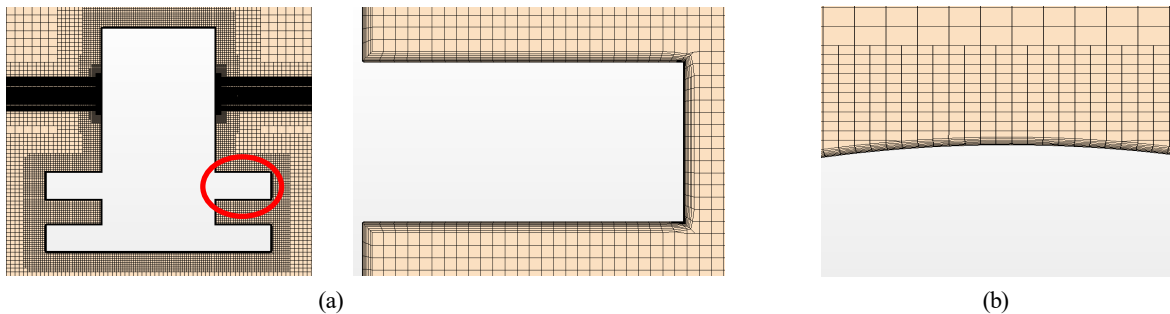


Fig. 4 Grid configuration adjacent to the damping plate: (a) side view and (b) top view

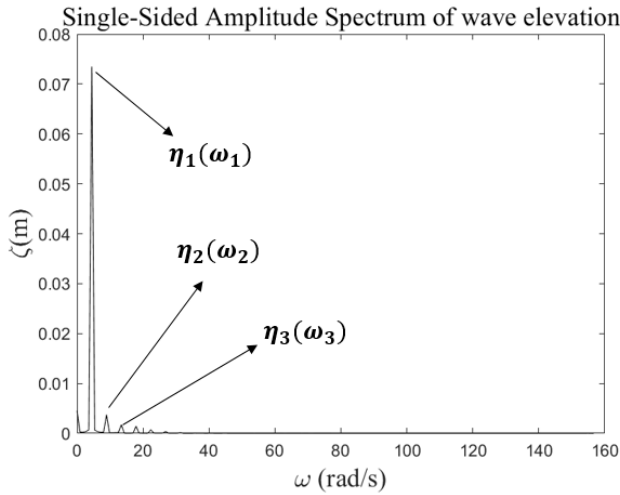


Fig. 5 DFT results for the wave run-up time series (ω : wave frequency, ζ : wave amplitude)

of the grid system. The relaxation zone incorporates grid damping and numerical forcing zones to prevent the reflected waves from downstream. The grid size in the computational zone was chosen as 150 grid points per wavelength and 20 grid points per wave height, respectively. Fig. 4 shows the detailed cell configuration near the damping plates.

The Discrete Fourier transform (DFT) method was applied to extract the first- and second-order harmonic components of wave run-up. Fig. 5 gives an example of the harmonic components of the wave elevation. The first- (η_1), second- (η_2), and third- (η_3) order harmonic components of the wave run-up are effectively extracted using DFT.

3. Numerical Validation

3.1 Verification of Incident Waves

Nam et al. (2008) conducted experiments under 24 regular wave conditions, including six different wave periods ($T = 7$ s, 8 s, 9 s, 10 s, 11 s, and 12 s) with four different wave steepness values ($\frac{H}{\lambda} = \frac{1}{50}, \frac{1}{30}, \frac{1}{16}, \text{ and } \frac{1}{10}$). In this study, only six regular waves ($T = 7$ s, 8 s, 9 s, 10 s, 11 s, and 12 s) with a constant wave steepness of $H/\lambda = 1/30$ were used for the numerical simulation and validation. As noted, a scaled cylinder model was used. Table 1 lists the dimensions

Table 1 Dimensions of truncated cylinder and wave conditions

Item	Prototype	Model
Scale	50.314	1.0
Cylinder	Diameter	16.0 m
	Draft	24.0 m
Wave condition	Wave period	7 s (76.43 m)
	(Wavelength)	12 s (284.32 m)
		0.986 s (1.519 m)
		1.692 s (5.651 m)

Table 2 Comparison of wave elevation between theory and simulation

Wave condition		Present CFD	Stokes 5th order theory	Difference
$T = 7$ s ($H/\lambda = 1/30$)	Crest (m)	0.0267	0.0269	0.59%
	Trough (m)	-0.0232	-0.0241	3.57%
$T = 12$ s ($H/\lambda = 1/30$)	Crest (m)	0.0987	0.0992	0.5%
	Trough (m)	-0.0881	-0.0892	1.23%

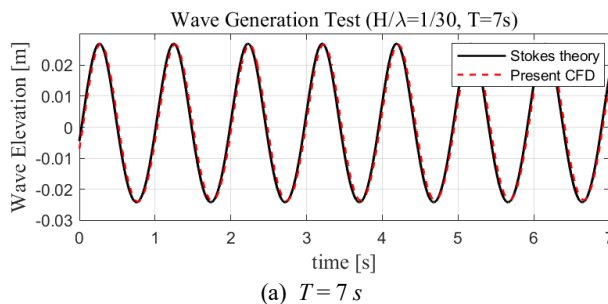
of the scaled truncated cylinder and the corresponding wave conditions.

Simulation tests of regular waves were conducted to verify the accuracy of wave generation in the present numerical wave tank. The calculated wave elevation time series was compared directly with the analytic solutions based on the fifth-order Stokes theory (Fenton, 1985). Fig. 6 compares the wave elevations between the simulation and theory. Table 2 lists the discrepancies between the wave elevations of theory and simulation. These results suggest that the present numerical wave tank can accurately generate the desired regular waves and effectively control wave dissipation.

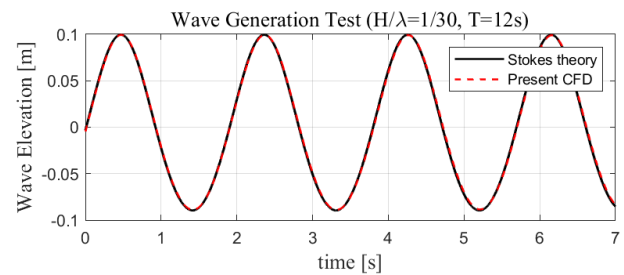
3.2 Convergence Study

As for spatial convergence in CFD simulations, the GCI method was used to estimate the discretization errors. In the present study, convergence analysis was performed with a focus on the crest values of the wave run-up around the truncated cylinder under the conditions of $T = 7$ s and $H/\lambda = 1/30$. Three different meshes (Meshes A, B, and C) were considered, with a refinement factor (r) chosen as $\sqrt{2}$. Table 3 provides detailed information for three mesh resolutions.

The changes in the numerical solution between Meshes A and B are denoted as $\epsilon_{BA} = (\eta_B - \eta_A)$, and the changes between Meshes B and C



(a) $T = 7$ s



(b) $T = 12$ s

Fig. 6 Comparison of the time history of wave generation ($H/\lambda = 1/30$)

Table 3 Spatial discretization for grid convergence study

Parameter	$H/\Delta z$	$L/\Delta x$	Total cell count
Mesh A	28	212	6.63 M
Mesh B	20	150	2.97 M
Mesh C	14	106	1.30 M

are denoted as $\epsilon_{CB} = (\eta_C - \eta_B)$, respectively. Based on the GCI method, the convergence ratio (R), order of accuracy (P), and GCI index were calculated using the following equations:

$$R = \epsilon_{BA} / \epsilon_{CB} \quad (3)$$

$$P = \frac{\ln\left(\frac{1}{R}\right)}{\ln(r_{BA})} + \frac{1}{\ln(r_{BA})} [\ln(r_{CB}^p - 1) - \ln(r_{BA}^p - 1)] \quad (4)$$

$$GCI_{BA} = \frac{FS\epsilon_{BA}}{r_{BA}-1}, \quad GCI_{CB} = \frac{FS\epsilon_{CB}}{r_{CB}-1} \quad (5)$$

where r is the refinement factor, and p denotes the theoretical order of the convergence, which is 2. FS is the safety factor of the method; Roche et al. (1994) recommended a constant value of FS as 1.25 when using more than two mesh resolutions.

The GCI index indicates an error band, representing how far the solution deviates from the asymptotic value. Therefore, a small GCI index indicates that the computation is within the asymptotic range. NASA (AIAA, 1998) proposed a principle to ensure that the grids are within the asymptotic range of convergence by checking that $\frac{GCI_{CB}}{r^P GCI_{BA}}$ close to 1. Table 4 provides details of all convergence parameters. The GCI indices for the first-order harmonic components of wave run-up at various wave probes were very small. Hence, Mesh B is sufficient for the numerical solution of wave run-up. Consequently, Mesh B was chosen as the appropriate mesh resolution for all the wave run-up simulations in this work.

3.3 Validation of Wave Run-Up on a Bare Truncated Cylinder

Before conducting the CFD simulations for a cylinder with dampers,

it is necessary to ensure the accuracy of the present numerical method. The validation of wave run-up and harmonic analysis around a bare truncated cylinder (without a damper) was performed by comparing the results of the present CFD simulations with the experimental data (Nam et al., 2008). The simulations for wave run-up were conducted for 10 wave periods, and the harmonic components were extracted using DFT over a time window of the last five periods. The first- and second-order harmonic components, as well as mean values of wave run-up, were directly compared to facilitate a precise comparison.

The first-order harmonic component represents the amplitude (η_1) of wave run-up corresponding to the fundamental wave frequency (ω). In the present study, the first-order harmonic component of wave run-up around the cylinder was normalized to the first-order harmonic amplitude of the incident wave (A_1). Fig. 7 compares normalized first-order harmonic components of wave run-up on the surface of the cylinder with respect to various scattering parameters (ka).

The second-order harmonic component indicates the amplitude (η_2) of wave run-up corresponding to the double wave frequency (2ω). Regarding the second-order harmonic components, the nonlinear interaction was more significant, particularly for short waves at the rear and shoulder points, and for long waves at the front and rear points of the truncated cylinder (Mohseni et al., 2018). The mean set up/down denotes the average time history for the free surface elevation. Both the mean set-up/down and the second-order harmonic components of the wave run-up were normalized to A_1^2/a . Here, “ a ” represents the radius of the cylinder. Fig. 8 presents the validation results of the second-order harmonic components.

The present CFD results for the first- and second-harmonic components agreed well with the experimental results. When the incident wave encounters the truncated cylinder, the wave propagation may be more or less disturbed because of the presence of the cylinder, causing some of the waves to be strongly reflected in front of the cylinder. This explains the relatively large wave run-up at WP1 (Fig. 7(a)). Moreover, the first-order harmonic components of wave run-up increased as the scattering parameter increased at wave probe 1, as reported by Morris-Thomas and Thiagarajan (2004). In the case of long waves, the first-order harmonic components at all the wave probes were close to one since the characteristic length of the truncated

Table 4 Convergence statics for the normalized first-order harmonic components of wave run-up

Items	WP1	WP2	WP3	WP4	WP5
Mesh A (m)	1.6695	1.4975	1.0145	0.7895	0.9772
Mesh B (m)	1.6661	1.4918	1.0149	0.7928	0.9751
Mesh C (m)	1.6629	1.4888	1.0152	0.7869	0.9736
ϵ_{BA}	0.0034	0.0057	0.0004	0.0033	0.0021
ϵ_{CB}	0.0032	0.0030	0.0003	0.0059	0.0015
GCI_{BA}	0.601%	1.008%	0.071%	0.583%	0.371%
GCI_{CB}	0.566%	0.530%	0.053%	1.043%	0.265%
$\frac{GCI_{CB}}{r^P GCI_{BA}}$	1.001	0.965	0.995	1.001	1.000

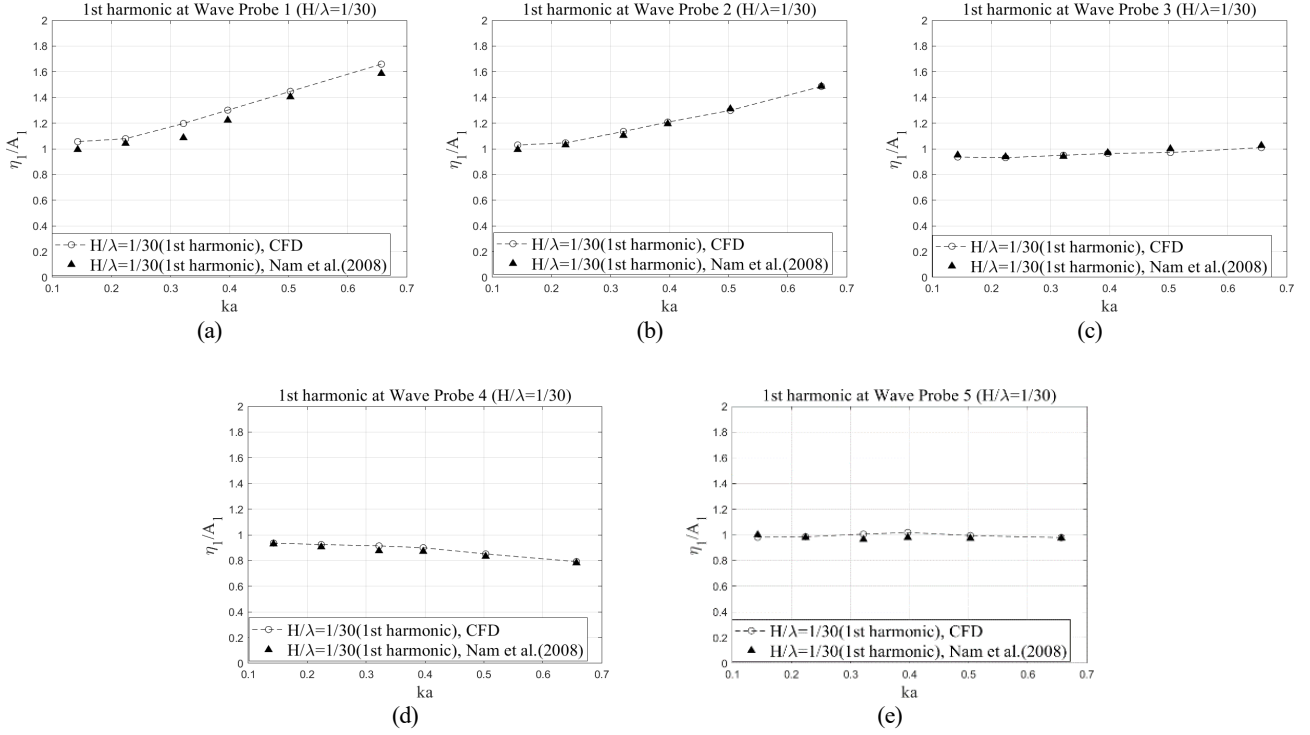


Fig. 7 Comparison of the first-order harmonic components of wave run-up between EFD & CFD results

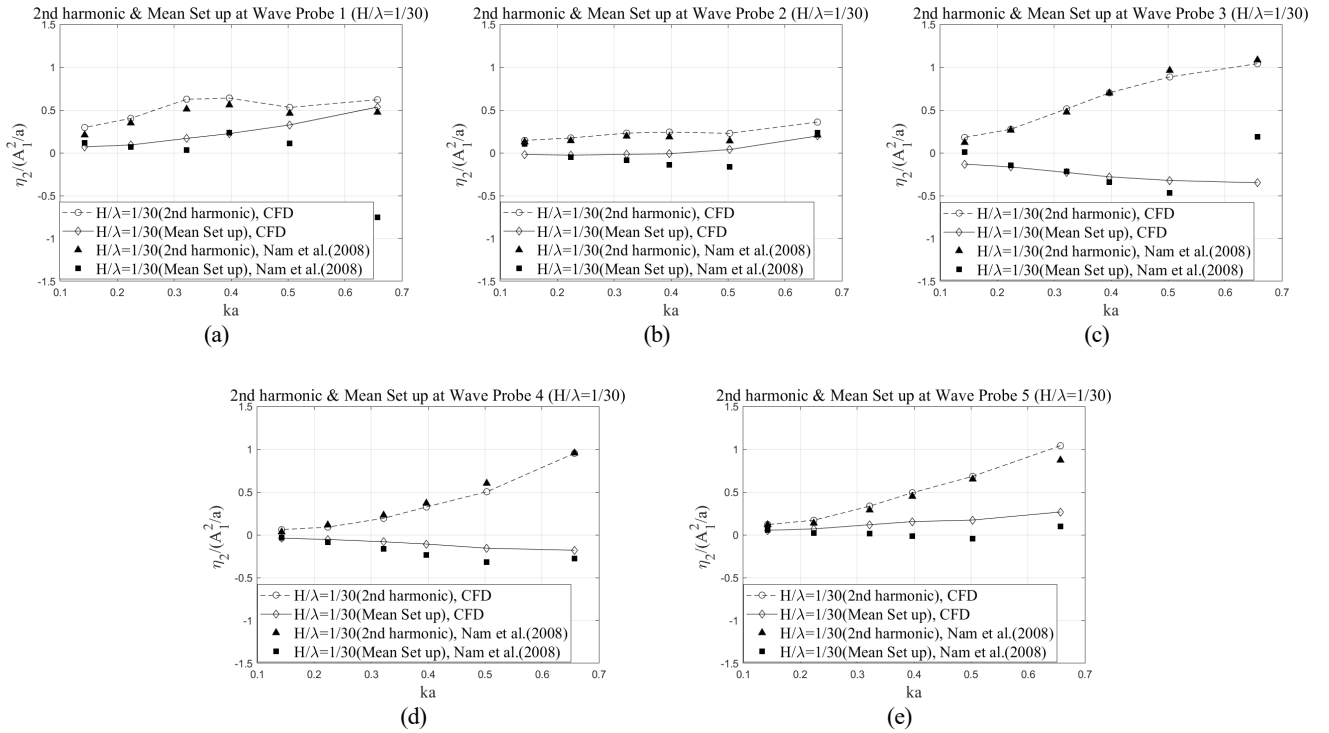


Fig. 8 Comparison of the second-order harmonic components and mean set-up components of wave run-up between EFD and CFD results

cylinder is relatively small compared to the incident wavelength. Furthermore, the mean set up/down of the free surface between the experiment and the present CFD results also matched well, except for several cases of short waves at the front and rear positions of the cylinder (Figs. 8(a) and 8(c)).

4. Results and Discussion

This study examined the effects of various dampers on the wave run-up around a truncated cylinder. Fig. 9 presents schematic diagrams of the cylinder with different dampers. Here, D denotes the

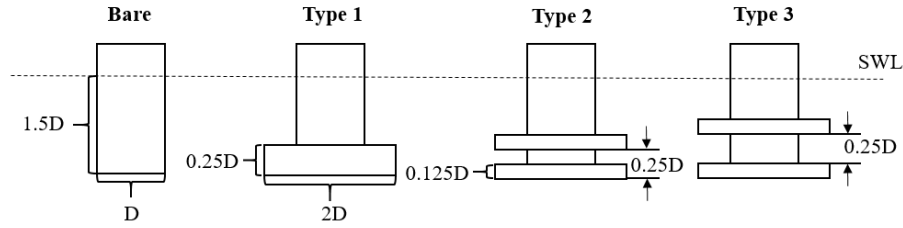


Fig. 9 Schematic diagram of the cylinders with various dampers

diameter of the truncated cylinder. The cylinder draft and the total damper thickness were assumed to be the same regardless of the damper type. As shown in Fig. 9, type 1 denotes the truncated cylinder with a single damper. From types 2 to 3 cylinders, dual dampers were attached to the truncated cylinders with various separating distances ($0.125 D$ and $0.25 D$). The lower damper was always fixed at the bottom for all cylinders.

4.1 Time History of Wave Elevation

Fig. 10 ($T = 7 s$, $H/\lambda = 1/30$) and Fig. 11 ($T = 12 s$, $H/\lambda = 1/30$) compare the wave run-up time series for four cylinders. Only the time histories of the last five wave periods are plotted in these

figures. When the short incident waves ($T = 7 s$) arrive, the wave run-up around the cylinders increase because of the presence of the damper (Fig. 10). In the case of the cylinders with dual dampers, the closer the upper damper is to the free surface, the stronger the scattering and amplification effects around the cylinder, leading to a higher run-up. Consequently, the wave elevations around the cylinder increased as the upper damper was raised upward. Regardless of the damper type, the amplification of wave elevation (WP1 and WP2) at the front face of the cylinder was greater than that of the side or rear of the cylinder (WP3, WP4, and WP5), which is also consistent with the trend observed in the bare cylinder. Therefore, the effect of the damper could be considered an

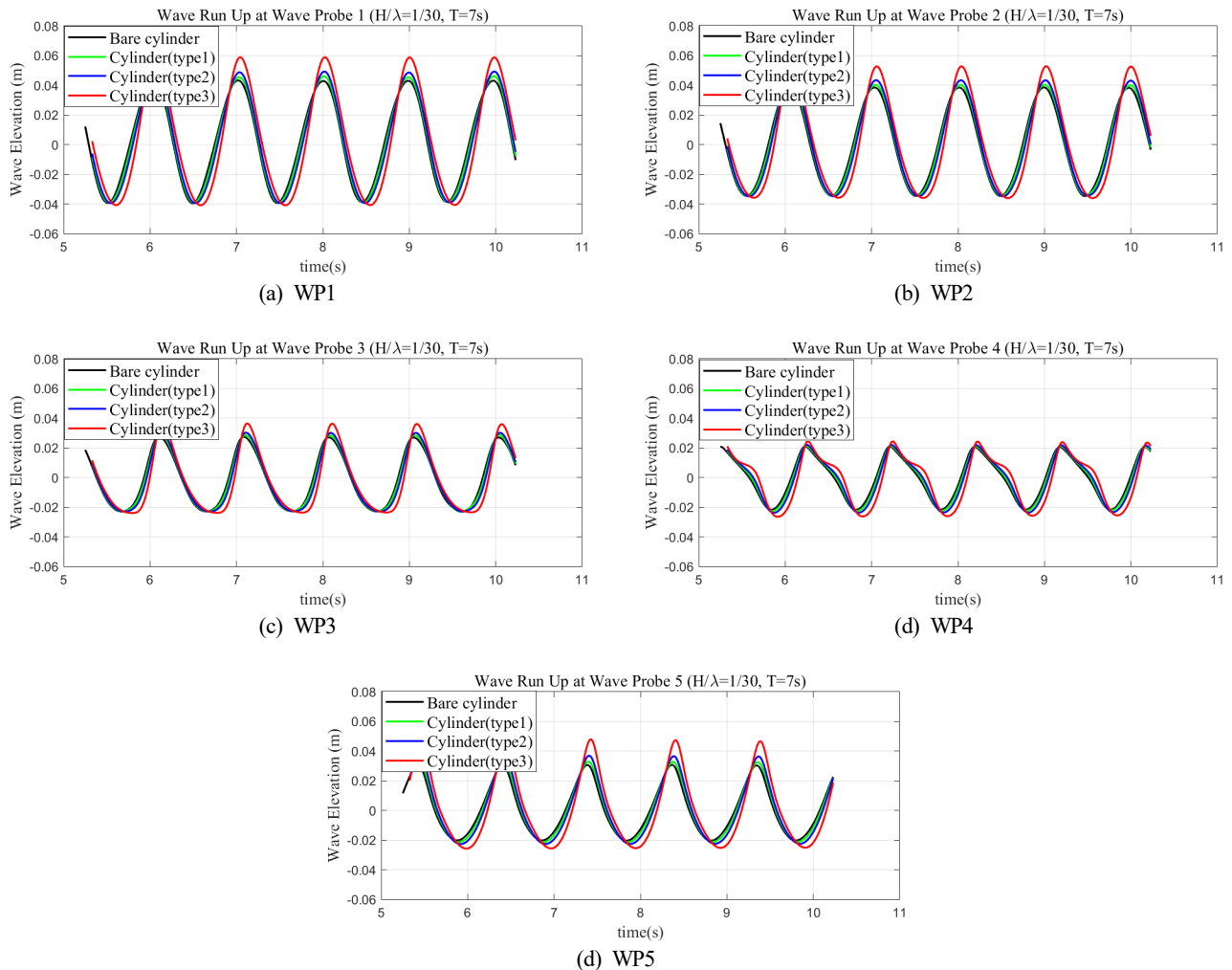


Fig. 10 Comparison of the time history of wave run-up around the cylinder with various dampers ($T = 7 s$, $H/\lambda = 1/30$)

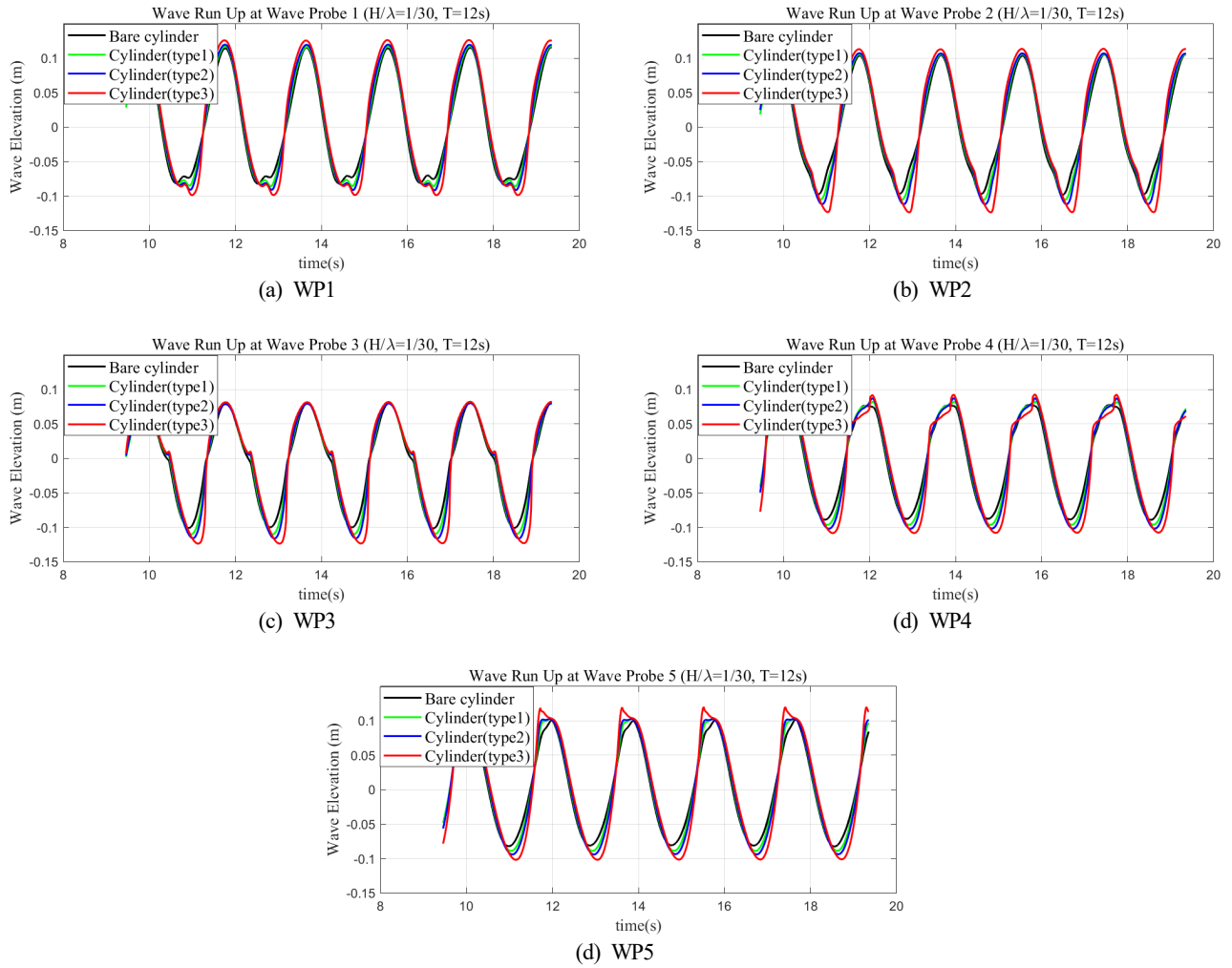


Fig. 11 Comparison of the time history of wave run-up around a cylinder with various dampers ($T = 12$ s, $H/\lambda = 1/30$)

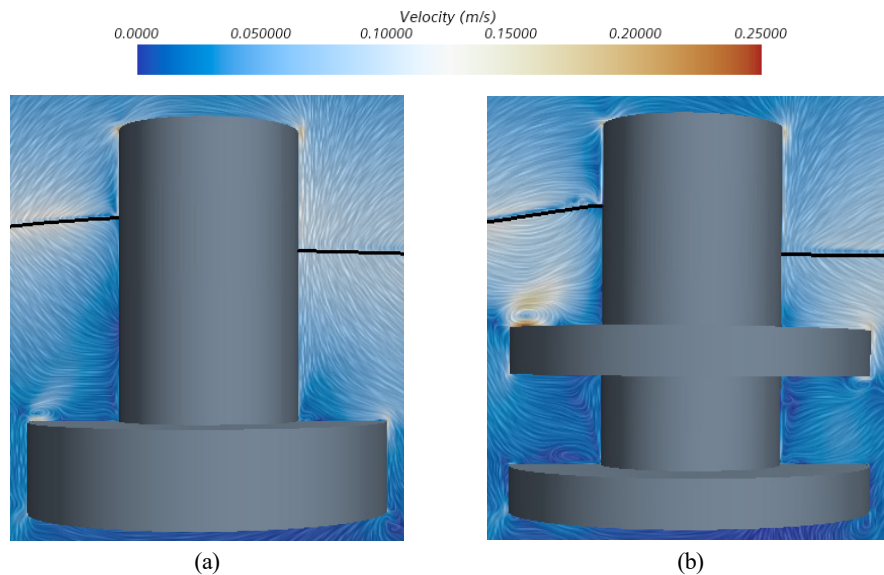


Fig. 12 Comparison of the velocity vector of the flow around the truncated cylinder ($t/T = 2.14$, $T = 7$ s, $H/\lambda = 1/30$): (a) type 1 and (b) type 3

enhancement of the original wave run-up characteristics for the bare cylinder. In particular, at the position of WP1, the kinetic energy of the incident wave was converted to a strong run-up because the front

cylinder surface and the upper damper work together to prevent the horizontal propagation of the incident wave and change the flow vertically upward. In addition, as the upper damper rises, it can

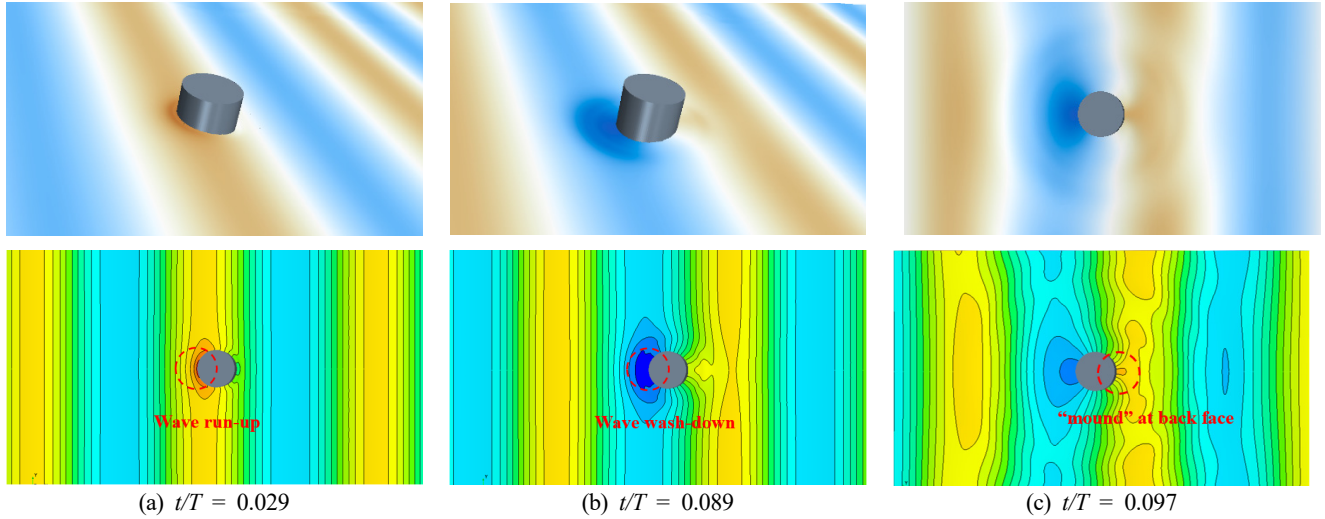


Fig. 13 Spatial contours of the wave elevation around the bare truncated cylinder ($T=7$ s, $H/\lambda = 1/30$)

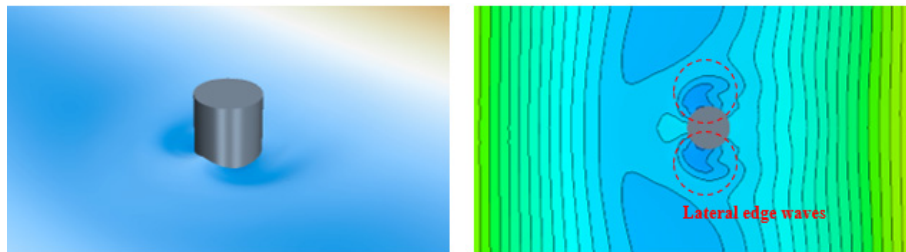


Fig. 14 Wave elevation around a bare truncated cylinder ($t/T=0.11$, $T=12$ s, $H/\lambda = 1/30$)

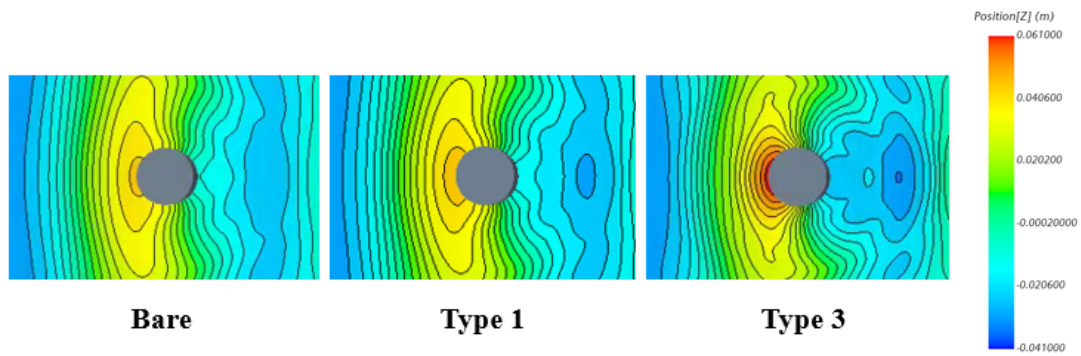


Fig. 15 Wave pattern of the free surface elevation around a cylinder with various dampers ($t/T=1.029$, $T=7$ s, $H/\lambda = 1/30$)

generate a strong vortex flow on the edge of the damper (Fig. 12), significantly altering the wave surface around the truncated cylinder. On the other hand, the effects of dampers on wave elevations around the cylinders were reduced when the wave period was 12 s (Fig. 11). This is because the diffraction effect becomes insignificant under the condition where the wavelength is much longer than the cylinder diameter. Interestingly, the higher position of the upper damper also causes higher wave crests and deeper wave troughs around the truncated cylinder (Figs. 10 and 11). The corresponding physical wave pattern could also be confirmed in Fig. 13.

Fig. 13 shows the top contour views of the free surface elevation around the truncated cylinder under short incident waves. Here, the

wave propagates from left to right. Significant run-up or wash-down occurs when the crest (Fig. 13(a)) or trough (Fig. 13(b)) of a propagating wave meets the front face of a truncated cylinder. Such a phenomenon was observed by Swan et al. (2005). When the incident waves surrounded the entire cylinder, two lateral edge waves were generated (separating at the front stagnation point) and moved towards the downstream direction. These two edge waves met at the back face of the cylinder, and a small “mound” of water occurred (Fig. 13(c)). Such a “mound” is also well known as back run-up (Swan et al., 2005, Wang et al., 2021). In addition, in the case of the long wave conditions, the diffraction waves were less significant than the short wave conditions (Fig. 14). Interestingly, as the wave trough passed the front

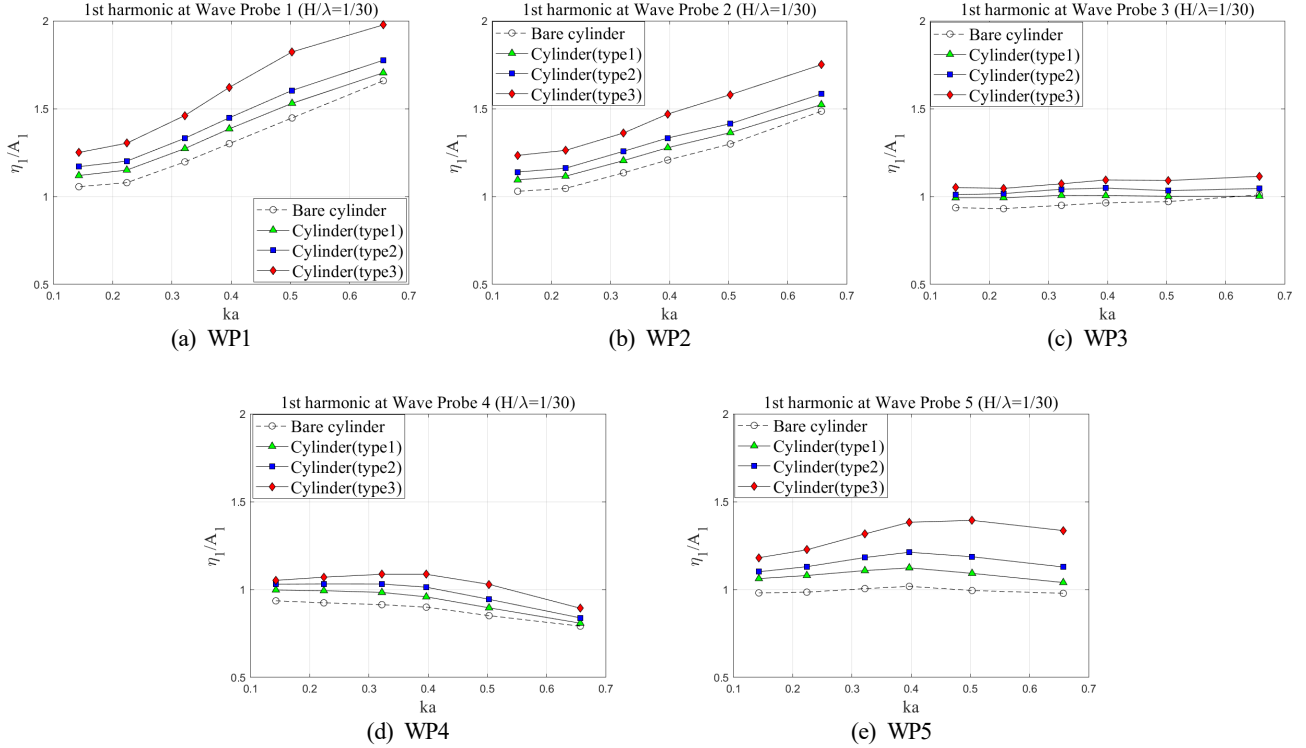


Fig. 16 Comparison for the first-order harmonic components of wave run-up around a cylinder with various scattering parameters

face of the cylinder, lateral edge waves occurred and began to propagate in the opposite direction along the cylinder surface towards the upstream face of the truncated cylinder.

4.2 First-Order Components of Wave Run-Up

The first-order harmonic component of wave run-up indicates the amplitude of wave elevation (η_1) corresponding to the fundamental wave frequency (ω). Fig. 16 presents the first-order harmonic components of wave run-up around various cylinders with respect to various scattering parameters (ka). The present results obviously showed that a gradual increase in the first-order harmonic components occurred around the cylinder as the position of the upper damper moved closer to the free surface. Such an increment became even more significant under short-wave conditions ($ka = 0.657$).

Furthermore, at each scattering parameter (ka), the amplification of

first-order harmonic components became more significant as the upper damper moved upward. The dramatic increase in the crest of total wave run-up could be explained by the first-order harmonic component being the dominant component. Moreover, the first-order harmonic components of wave run-up on the weather side (WP1 & WP2) of the cylinder increased as the scattering parameter increased, following the original characteristics for the bare cylinder. Fig. 17 presents the distributions of first-order harmonic components at different wave probes. In the case of short wave conditions (Fig. 17(a)), there was a consistent decreasing tendency of the first-order harmonic components of wave run-up from the front point (WP1) to the back shoulder point (WP4) and then an increase again at the back point (WP5). In contrast, under long wave conditions, the variations of the first-order harmonic components of wave run-up at various probes became less significant (Fig. 17(b)).

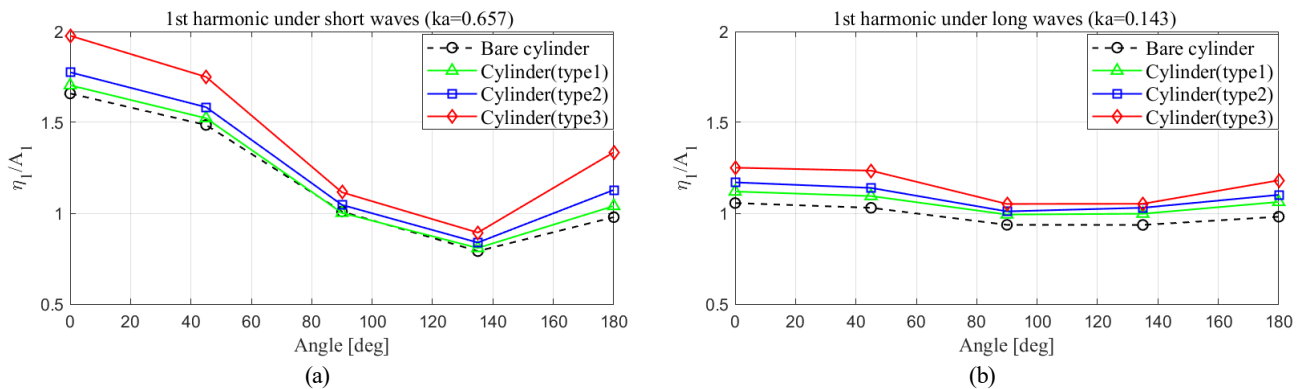


Fig. 17 Comparison of the first-order harmonic components of wave run-up around cylinder w.r.t. various positions

4.3 Second-Order Components of Wave Run-Up

Figs. 18 and 19 show the second-order harmonic components and mean set-up/set-down of wave run-up around the cylinder with different dampers. Here, the second-order harmonic component of wave run-up around the cylinder indicates the amplitude of the wave

component (η_2) at the double wave frequency (2ω), corresponding to the second-order sum-frequency component of the free-surface elevation. Furthermore, the mean set-up/set-down of the free surface elevation could be considered the second-order difference frequency component.

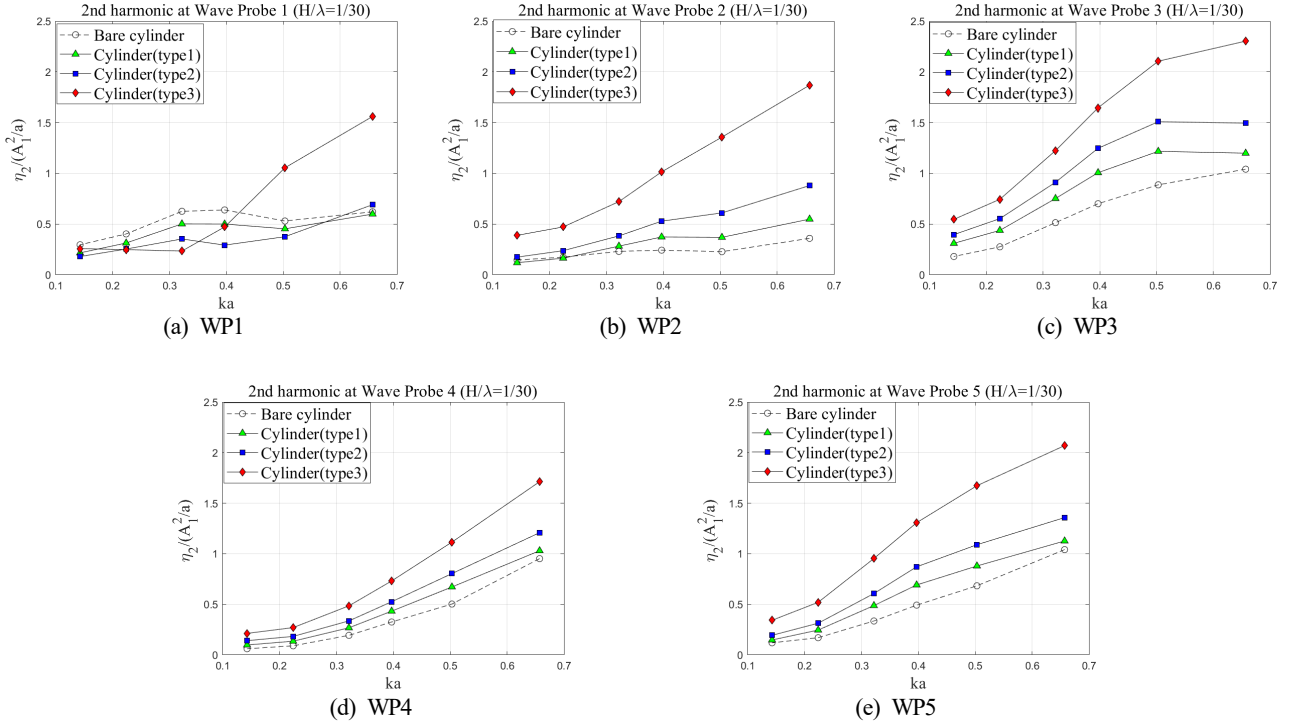


Fig. 18 Comparison of the second-order harmonic components of wave run-up around a cylinder

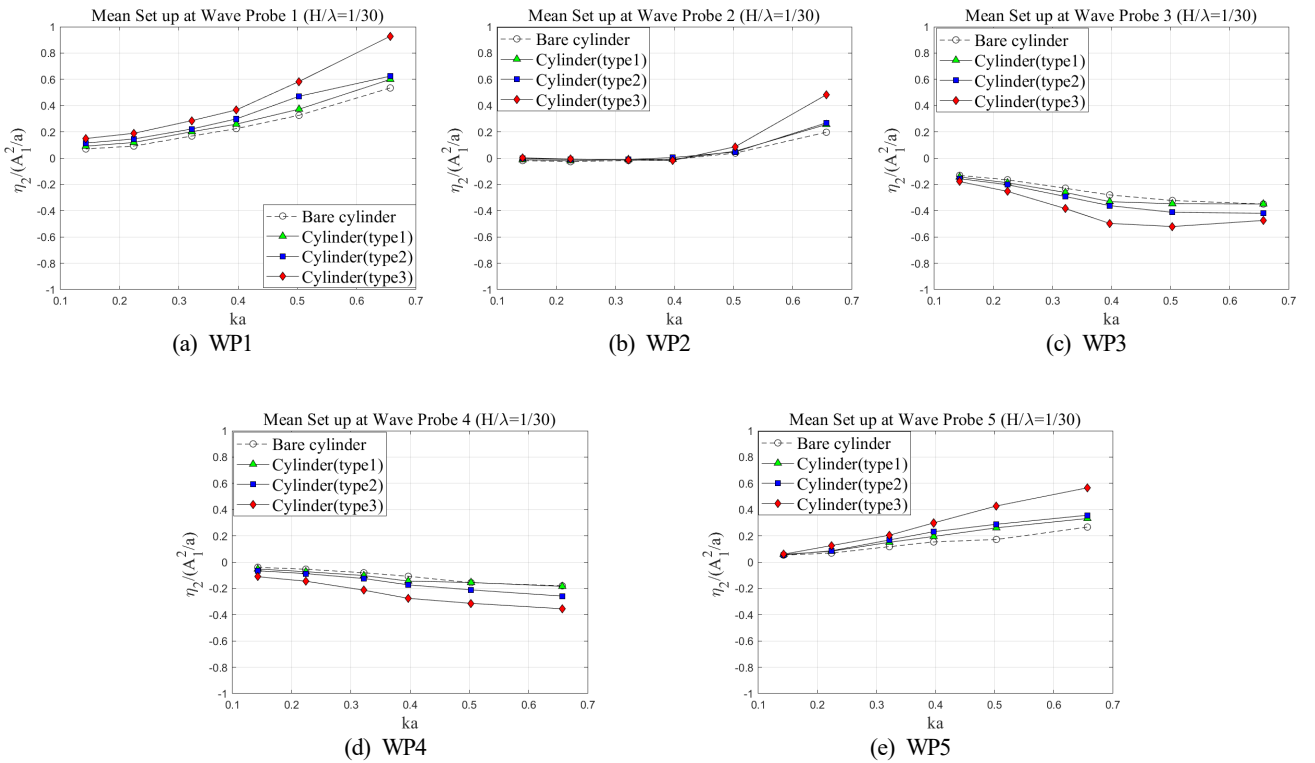


Fig. 19 Comparison of the mean set-up components of wave run-up around a cylinder

The overall second-order harmonic components of wave run-up around the cylinder increased as the scattering parameter increased, similar to the first-order harmonic components. On the other hand, the effects of the damper on the second-order harmonic components at the stagnation point (WP1) were not monotonous (Fig. 18(a)). Regarding the types 1 and 2 dampers, the behavior of the second-order harmonic components similarly follows that of a bare cylinder, whereas a rapid increase was found in the case of type 3, where the upper damper closely approaches the free surface. In addition, the increases in type 2 and type 3 dampers were more significant compared to those between the type 1 and type 2 dampers, as depicted in Fig. 18. Hence, the second-order harmonic components of wave run-up are also strongly affected by the position of the upper damper. Interestingly, the second-order harmonic components became significant on the lee side and rear locations (WP3~WP5) of the cylinder.

The mean set-up/set-down component of the wave run-up indicates the average value of the time series of the free surface elevation. Fig.19 shows the variations in the mean set-up components of wave run-up around a cylinder with various dampers. Different tendencies were observed in the mean set-up components compared to the first- and second-order harmonic components of wave run-up. Here, the damping plate amplified the change in the mean free surface elevations around the truncated cylinder. For example, at WP1 (Fig.19(a)), the set-up of the mean wave elevation was observed, particularly under short wave conditions (i.e., high scattering parameter), and the attachment of the damper caused an increase in set-up values. On the other hand, the set-down of the mean wave elevation was observed at WP3 and WP4(Figs. 19(c) and 19(d)). The decrease in the mean wave elevation became more significant because of the damper attachments. Such a phenomenon could also be observed in the time history of the wave elevations (Figs. 10(d) and 11(d)). The wave wash-down was more noticeable than the run-up at the back shoulder point (WP4) of the cylinder. In general, in the case of short-wave conditions, variations of mean set up/down became more significant because of the presence of a damper. Nevertheless, the magnitude of the mean set up/down is smaller than the second-order harmonic components of wave run-up commonly, as also discussed by Mohseni et al. (2018).

5. Conclusion

This study examined the effect of the heave damping plates on wave run-up characteristics around a truncated circular cylinder. The numerical validation was performed by comparing the wave run-up components around a bare truncated cylinder between the present numerical results and the model test data from Nam et al. (2008). A truncated cylinder with three different types of dampers was introduced for the CFD simulations. The closer the upper damper is to the free surface, the stronger the scattering and amplification effects, leading to higher wave crests and deeper wave troughs around the truncated cylinder. Regarding the nonlinearities of the wave run-ups, the amplification of the first- and second-order harmonic components

became more significant as the upper damper moves upward. In particular, regarding the mean set-up, the damping plate amplifies the original change in the mean free surface elevations around the truncated cylinder instead of showing a monotonous increment. Based on the present work, future research will focus on the optimal arrangement of the damping plates and the wave forces acting on the cylinder under different wave conditions.

Conflict of Interest

Bo Woo Nam serves as a journal publication committee member of the Journal of Ocean Engineering and Technology, but he had no role in the decision to publish this article. No potential conflict of interest relevant to this article was reported.

Funding

This work was supported by the “Development of Design Technology for TLP-type Floating Offshore Wind Turbine System and Scaled Model Test Technique” of the New & Renewable Energy of the Korea Institute of Energy Technology Evaluation and Planning (KETEP) grant funded by the Ministry of Trade, Industry and Energy (MOTIE) (No. 20223030020130). This research was also supported by the Korea Agency for Infrastructure Technology Advancement (KAIA) grant funded by the Ministry of Land, Infrastructure and Transport (Grant RS-2023-00250727) through the Korea Floating Infrastructure Research Center at Seoul National University.

References

- American Institute of Aeronautics and Astronautics (AIAA). (1998). *AIAA guide for the verification and validation of computational fluid dynamics simulations*. AIAA.
- American Petroleum Institute. (API). (2001). *Recommended practice for planning, designing, and constructing floating production systems*. American Petroleum Institute.
- DNV GL. (2015). *Recommended practices (RP) “Column-Stabilised Units”* (DNVGL-RP-C103).
- Fenton, J. D. (1985). A fifth-order Stokes theory for steady waves. *Journal of waterway, port, coastal, and ocean engineering*, 111(2), 216–234. [https://doi.org/10.1061/\(ASCE\)0733-950X\(1985\)111:2\(216\)](https://doi.org/10.1061/(ASCE)0733-950X(1985)111:2(216))
- Havelock, T. H. (1940). The pressure of water waves upon a fixed obstacle. *Proceedings of the Royal Society of London. Series A. Mathematical and Physical Sciences*, 175(963), 409–421. <https://doi.org/10.1098/rspa.1940.0066>
- Huijs, F., de Bruijn, R., & Savenije, F. (2014). Concept design verification of a semi-submersible floating wind turbine using coupled simulations. *Energy Procedia*, 53, 2–12. <https://doi.org/10.1016/j.egypro.2014.07.210>
- Kim, J., Jaiman, R., Cosgrove, S., & O’Sullivan, J. (2011). Numerical

- wave tank analysis of wave run-up on a truncated vertical cylinder. *Proceedings of International Conference on Offshore Mechanics and Arctic Engineering*, 805–814. <https://doi.org/10.1115/OMAE2011-50283>
- Koo, B. G., Park, D. W., & Paik, K. J. (2014). A study on wave run-up height and depression depth around air-water interface-piercing circular cylinder. *Journal of the Korean Society of Marine Environment & Safety*, 20(3), 312–317. <https://doi.org/10.7837/kosomes.2014.20.3.312>
- Lefebvre, S., & Collu, M. (2012). Preliminary design of a floating support structure for a 5 MW offshore wind turbine. *Ocean Engineering*, 40, 15–26. <https://doi.org/10.1016/j.oceaneng.2011.12.009>
- MacCamy, R. C., & Fuchs, R. A. (1954). *Wave forces on piles: a diffraction theory* (No. 69). US Beach Erosion Board.
- Mohseni, M., Esperanca, P. T., & Sphaier, S. H. (2018). Numerical study of wave run-up on a fixed and vertical surface-piercing cylinder subjected to regular, non-breaking waves using OpenFOAM. *Applied Ocean Research*, 79, 228–252. <https://doi.org/10.1016/j.apor.2018.08.003>
- Morris-Thomas, M. T., & Thiagarajan, K. P. (2004). The run-up on a cylinder in progressive surface gravity waves: harmonic components. *Applied Ocean Research*, 26(3–4), 98–113. <https://doi.org/10.1016/j.apor.2004.11.002>
- Musial, W., Spitsen, P., Duffy, P., Beiter, P., Shields, M., Hernando, D. M., Hammond, R., Marquis, M., King, J., & Sriharan, S. (2023). *Offshore wind market report: 2023 edition*. United States. <https://doi.org/10.2172/1997466>
- Nam, B. W., Sung, H. G., Kim, Y. S., & Hong, S. Y. (2008). Experiments second-order computations for run-up around a truncated cylinder in waves. *Journal of Ships & Ocean Engineering*, 46, 43–52.
- Omer Jr, G. C., & Hall, H. H. (1949). The scattering of a tsunami by a cylindrical island. *Bulletin of the Seismological Society of America*, 39(4), 257–260. <https://doi.org/10.1785/BSSA0390040257>
- Perić, R., & Abdel-Maksoud, M. (2018). Analytical prediction of reflection coefficients for wave absorbing layers in flow simulations of regular free-surface waves. *Ocean Engineering*, 147, 132–147. <https://doi.org/10.1016/j.oceaneng.2017.10.009>
- Roache, P. J. (1994). Perspective: A method for uniform reporting of grid refinement studies. *Journal of Fluids Engineering*, 116(3), 405–413. <https://doi.org/10.1115/1.2910291>
- Robertson, A., Jonkman, J., Masciola, M., Song, H., Goupee, A., Coulling, A., & Luan, C. (2014). *Definition of the semi-submersible floating system for phase II of OC4* (No. NREL/TP-5000-60601). National Renewable Energy Lab. (NREL), Golden, CO.
- Roddier, D., Cermelli, C., Aubault, A., & Weinstein, A. (2010). WindFloat: A floating foundation for offshore wind turbines. *Journal of renewable and sustainable energy*, 2(3), 033104. <https://doi.org/10.1063/1.3435339>
- Swan, C., Masterton, S., Sheikh, R., & Cavalletti, A. (2005, January). Wave forcing and wave scattering from a vertical surface-piercing cylinder. *Proceedings of the International Conference on Offshore Mechanics and Arctic Engineering* (Vol. 41960, pp. 571–580). <https://doi.org/10.1115/OMAE2005-67158>
- Wang, Q., Fang, Y., & Liu, H. (2021). An experimental study of run-up and loads on a vertical truncated cylinder in a solitary wave. *Ocean Engineering*, 219, 108346. <https://doi.org/10.1016/j.oceaneng.2020.108346>

Author ORCIDs

Author name	ORCID
Song, Zhenhao	0009-0001-8268-5618
Nam, Bo Woo	0000-0003-1125-7453

Dynamic Behavior Assessment of OC4 Semi-submersible FOWT Platform Through Morison Equation

Chungkuk Jin¹, Ikjae Lee², JeongYong Park² and MooHyun Kim³

¹Assistant Professor, Department of Ocean Engineering and Marine Sciences, Florida Institute of Technology, FL, USA

²Graduate Student, Department of Ocean Engineering, Texas A&M University, TX, USA

³Professor, Department of Ocean Engineering, Texas A&M University, TX, USA

KEYWORDS: FOWT, OC4 Semi-submersible, Diffraction, Morison, Effective inertia coefficient, Random wave

ABSTRACT: This paper proposes an effective inertia coefficient (EIC) in the Morison equation for better wave-force calculations. The OC4 semi-submersible floating offshore wind turbine (FOWT) platform was considered to test the feasibility. Large diffraction at large Keulegan-Carpenter (KC) numbers and the interaction between columns can result in errors in estimating the wave force using the Morison equation with a theoretical inertia coefficient, which can be corrected by the EIC as a function of the wave period and direction. The horizontal and vertical wave forces were calculated using the Morison equation and potential theory at each column, wave period, and wave direction. The EICs of each column were then obtained, resulting in a minimal difference between the Morison inertia force and the wave excitation force by the potential theory. The EICs, wave forces, phase angles, and dynamic motions were compared to confirm the feasibility of an EIC concept under regular and random waves.

1. Introduction

Cylindrical floating and underwater structures are used widely, including spar-type offshore platforms, monopile offshore wind turbines, spar and semi-submersible floating offshore wind turbines (FOWTs), marine risers and pipelines, and submerged floating tunnels. Several frequency- and time-domain numerical methods have been proposed to understand the hydrodynamic behaviors. In particular, in time domain analysis, computational fluid dynamics (CFD), potential-flow-based numerical wave tank, and Cummins equation have been used to assess the wave forces and dynamic behaviors of cylindrical structures in the ocean (Abbasnia and Soares, 2018; Dafnakis et al., 2020; Paulsen, et al., 2014). On the other hand, these numerical methods are time-inefficient, particularly when the fluid domain is large, structure size is large, multiple bodies interact (multi-body problem), and hydroelasticity is considered. These methods may be inefficient if many simulations are considered in the initial design optimization phase.

An alternative method is to use the Morison equation (Morison et al., 1950), which is used widely for cylindrical objects because of its simplicity and low computational expense (Boccotti et al., 2013; Chen

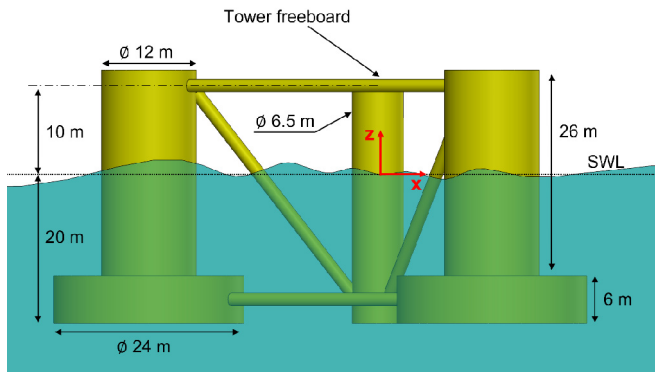
et al., 2015; Jin et al., 2021; Lin et al., 2018). Nevertheless, the equation has fundamental assumptions in that a wavelength is much larger than the structural characteristic length (i.e., a slender body approximation), and the radiation-damping force is not that significant. The Morison equation has inertia, added mass, and drag coefficients. The inertia coefficient denotes the contribution from Froude-Krylov (FK) and diffraction forces, and the representative value of the inertia coefficient for cylinders is two for a slender body (Faltinsen, 1993). The inertia coefficient should be modified if the cylinder is exposed to short waves due to significant diffraction. Many studies have examined the validity of the Morison equation for vertical and horizontal cylinders. For vertical cylinders, Chakrabarti and Tam (1975) investigated the wave forces from MacCamy Fuchs's analytical solution (potential theory) and the Morison equation for a bottom-mounted vertical cylinder. They introduced the effective inertia coefficient (EIC) by comparing the wave forces from the Morison equation with the analytical solution. The EIC tended to decrease with the Keulegan-Carpenter (KC) number because of the significant diffraction force. Chung (2018) reported that the inertia coefficient could be a function of the wave frequency when the structure is close to the free surface. This means selecting the EIC is critical, and large

Received 20 September 2023, revised 6 November 2023, accepted 21 November 2023

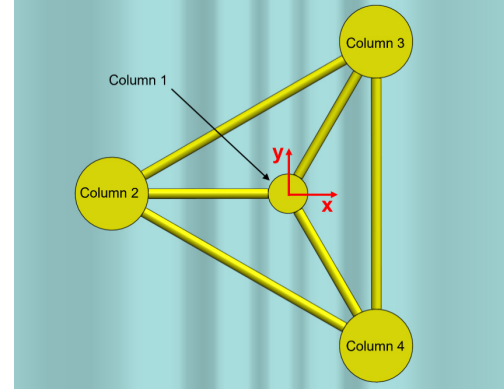
Corresponding author Chungkuk Jin: +1-321-674-8934, cjin@fit.edu

© 2023, The Korean Society of Ocean Engineers

This is an open access article distributed under the terms of the creative commons attribution non-commercial license (<http://creativecommons.org/licenses/by-nc/4.0>) which permits unrestricted non-commercial use, distribution, and reproduction in any medium, provided the original work is properly cited.



(a) Side view



(b) Top view

Fig. 1 Configuration of OC4 semi-submersible FOWT platform (only four columns are considered in this study).

errors are expected when inputting a representative/theoretical inertia coefficient. Chang et al. (2019) compared results from the numerical wave tank and Morison equation up to second-order wave kinematics for the vertical cylinder and discussed that the Morison equation underestimates or overestimates wave forces as wave steepness is high. In contrast, the overall comparison for low-wave steepness is excellent. For horizontal cylinders, Li et al. (1997) compared the in-line responses of fully submerged cylinders between experiments and the Morison equation, highlighting that the inertia coefficients do not change substantially with regard to the KC number. On the other hand, Chen et al. (2015) compared the Morison equation with a CFD simulation. They reported that a partly submerged horizontal cylinder could induce a large underprediction of the wave force by up to 50% relative errors. Jin (2022) and Jin et al. (2023) showed some differences between inertia forces and wave excitation forces from potential theory observed when the horizontal cylinder is close to the free surface, resulting in a difference in elastic behaviors, especially in short waves. These studies support the importance of correctly selecting the inertia coefficient in the Morison equation for short waves (or high KC numbers).

This study proposes an EIC in the Morison equation in regular and random waves to compare high-fidelity numerical methods and the Morison equation. The OC4 semi-submersible floating offshore wind turbine (FOWT) platform was selected for a feasibility demonstration. The Morison equation can be used to evaluate the hydrodynamic behavior and its effectiveness to some degree (González et al., 2021; Takata et al., 2021). In addition, Kvittem et al. (2012) calculated the EIC by comparing the added mass from potential theory with the added mass term in the Morison equation, showing improvement in the motion response amplitude operator (RAO) of semi-submersible FOWT. Compared to previous research (Kvittem et al., 2012), this study improved the EIC approach in that each column has a separate EIC at various wave periods and directions. This study first assessed the horizontal and vertical wave forces using the Morison equation and potential theory at each column, wave period, and wave direction. An estimation of the EIC under regular and random waves was followed, which minimized the difference between the two methods. The EICs,

wave forces, phase angles, and dynamic motions were compared systematically to show the feasibility of an EIC concept under regular and random wave excitations.

2. Configuration of OC4 Semi-Submersible FOWT Platform

Fig. 1 presents the side and top views of the OC4 semi-submersible FOWT platform. Although this FOWT consists of blades, nacelle, tower, floater, and mooring lines, this study only focused on the platform hydrodynamics. The platform has one center column (Column 1), three side columns (Columns 2–4), and slender pontoons and braces. The side columns consist of upper and base columns with different diameters. This study only considered four large columns (Columns 1–4); the others were neglected because pontoons and braces are slender and are typically modeled by the Morison equation. The direct comparison between the potential theory and the Morison equation for Columns 1–4 was possible. The detailed design parameters are not described in this paper and can be found elsewhere (Robertson et al., 2014).

3. Method

3.1 Morison Equation

The Morison equation (Morison et al., 1950) for a moving body consists of linear inertia, linear added mass, and quadratic drag terms, which can be written as follows:

$$\mathbf{F}_M = \rho C_I \nabla \mathbf{a} - \rho C_A \nabla \ddot{\mathbf{X}} + \rho C_D A |\mathbf{v} - \dot{\mathbf{X}}| (\mathbf{v} - \dot{\mathbf{X}}) \quad (1)$$

where ρ is the water density; C_I , C_A , and C_D are the inertia, added mass, and drag coefficients, respectively; \mathbf{a} and \mathbf{v} are the acceleration and velocity of fluid particles at a geometric center; $\ddot{\mathbf{X}}$ and $\dot{\mathbf{X}}$ are the acceleration and velocity of the platform; and ∇ and A are the displaced volume and drag area. C_I , C_A , and C_D in the Morison equation are typically obtained experimentally and through analytical solutions and numerical simulations. This study adopted the Airy wave

theory to obtain wave kinematics.

This study focused on the inertia force \mathbf{F}_I , which is the first term in Eq. (1). Based on the configuration given in Fig. 1, the way to evaluate \mathbf{F}_I in the horizontal and vertical direction was different. In the case of the horizontal force, the column was first discretized into 20 elements along the vertical direction (1 m height for each element). The inertia force was calculated at each element with the element volume. The total force of each column was obtained by integrating the element forces. The volume exposed to water only needs to be considered in the case of the vertical force. A correction needs to be made if the top area is not exposed to water like OC4 semi-submersible because the Morison equation considers the body fully submerged in water. For Column 1 (the main column at the center), the inertia force was first estimated at its geometric center (i.e., $z = -10$ m) using the first term in Eq. (1). This portion was then corrected by deducting the FK force on the top surface because the top surface at the mean water level (i.e., $z = 0$ m) is not exposed to water. For Columns 2–4, the base columns are only exposed to water in the vertical direction. Therefore, the inertia force was obtained only from the base columns at its geometric center (i.e., $z = -17$ m). The FK force at the location at which the upper and base columns meet (i.e., $z = -14$ m) was partly eliminated with the area of the top column. The following equation can be used for horizontal and vertical inertia forces on the column (\mathbf{F}_{IH} and \mathbf{F}_{IV}):

$$\mathbf{F}_{IH} = \sum_{e=1}^E \rho C_I \nabla \mathbf{a}_e \quad (2)$$

$$\mathbf{F}_{IV} = \rho C_I \nabla \mathbf{a} + P_I A_T \quad (3)$$

where e is the element number in the vertical direction; P_I is the incident wave pressure; and A_T denotes the surface on the top section that is not exposed to water.

3.2 Potential Theory in Frequency Domain

Two fundamental equations of potential theory are the Laplace and Bernoulli equations. First, the first-order boundary value problem is solved by Green's integral equation. In this problem, the governing equation is the Laplace equation, assuming inviscid, incompressible, and irrotational flows. The governing equation is solved with the boundary conditions on the free surface, bottom, body, and far-field, which results in the velocity potentials of incident, diffraction, and radiation waves as follows:

$$\Phi = \Phi_I + \Phi_D + \Phi_R \quad (4)$$

where Φ_I , Φ_D , and Φ_R are the first-order incident, diffracted, and radiated wave potentials. The first-order hydrodynamic pressure on the wetted body surface is given by the Bernoulli equation as follows:

$$P = -\rho \frac{\partial(\Phi_I + \Phi_D + \Phi_R)}{\partial t} \quad (5)$$

The force is obtained by integrating the pressure over the wetted surface. The wave excitation force is obtained by the incident and

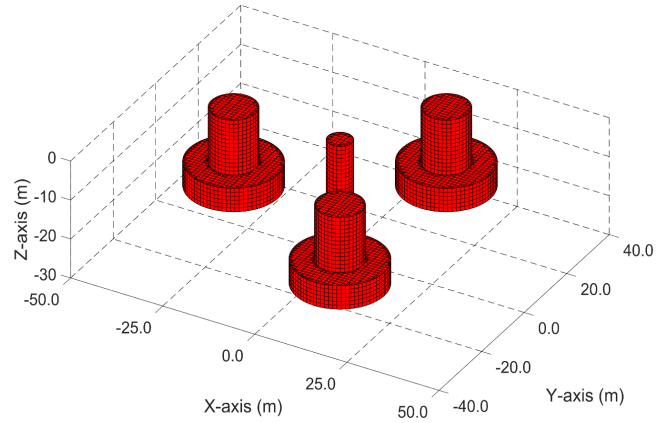


Fig. 2 Panel model of OC4 semi-submersible FOWT platform.

diffracted wave pressures as:

$$\mathbf{F}_{EX} = \iint_{S_b} (P_I + P_D) \mathbf{n} dS \quad (6)$$

where P_I and P_D are the incident and diffracted wave pressures, and S_b denotes the wetted surface. The 3D diffraction/radiation panel method was used to obtain the wave excitation forces and hydrodynamic coefficients (Lee, 1995). Fig. 2 presents the panel model used in this study. This study considered 7,181 panels below the mean water level.

3.3 Effective Inertia Coefficient in Morison Equation

In the Morison equation given in Eq. (1), the inertia coefficient, C_I , is defined as $1+C_A$ where one and C_A are related to the contribution from the FK and diffraction forces. In a cylindrical structure, C_A is typically set to one, meaning that the contribution from that FK force is the same as that from the diffraction force (Faltinsen, 1993). On the other hand, as described by Chakrabarti and Tam (1975), the total force is significantly affected by large diffraction in short waves, which requires some correction in the inertia coefficient to be well correlated with the wave excitation force. As a result, the EIC was introduced in this study. The horizontal and vertical EICs for each column in regular waves are defined by Eqs. (7)–(8), respectively:

$$C_{I,eff}(\omega, \beta) = \frac{\mathbf{F}_{EX}(\omega, \beta)}{\sum_{e=1}^E \rho \nabla \mathbf{a}_e(\omega, \beta)} \quad (7)$$

$$C_{I,eff}(\omega, \beta) = \frac{\mathbf{F}_{EX}(\omega, \beta) - P_I(\omega, \beta) A_T}{\rho \nabla \mathbf{a}(\omega, \beta)} \quad (8)$$

where ω and β are angular frequency and wave direction, respectively. In the case of random waves, depicting one EIC value is challenging, so a simple statistical approach was adopted. The time history of the wave excitation forces was first obtained by superposing the sinusoidal forces at different regular wave frequencies. The Pierson–Moskowitz (PM) spectrum was considered for fully developed seas. The root mean square error (RMSE) between the time histories of the wave excitation force and the Morison inertia force was calculated at

different inertia coefficients. The inertia coefficient that gives the lowest RMSE was selected as EIC under random waves as follows:

$$C_{l,eff}(T_p, \beta) = \min \left[\sqrt{\frac{\sum_{t=1}^T (\mathbf{F}_{EX}(T_p, \beta)_t - \mathbf{F}_I(T_p, \beta)_t)^2}{T}} \right] \quad (9)$$

where t and T denote the time step and final time step, T_p is the peak period, and \mathbf{F}_I is the Morison inertia force. The Morison equation may not be correlated well when diffracted waves significantly change the phase of the total force in very short waves because the Morison equation uses the phase of fluid acceleration only.

3.4 Time-Domain Equation of Motion for Platform

The time-domain equations of motion for the FOWT platform were established by the Cummins equation and Morison formula given in Eqs. (10)–(11) as follows:

$$[\mathbf{M} + \mathbf{A}(\infty)]\ddot{\mathbf{X}} + \mathbf{C}\dot{\mathbf{X}} + \mathbf{K}\mathbf{X} = \mathbf{F}_{EX} + \mathbf{F}_R \quad (10)$$

$$\mathbf{M}\ddot{\mathbf{X}} + \mathbf{C}\dot{\mathbf{X}} + \mathbf{K}\mathbf{X} = \mathbf{F}_M \quad (11)$$

where \mathbf{M} is the mass matrix; $\mathbf{A}(\infty)$ is the added mass matrix at infinite frequency; \mathbf{C} is the external damping matrix; \mathbf{K} is the hydrostatic and gravitational restoring matrix; \mathbf{F}_R is the convolution-integral based radiation damping force; and \mathbf{F}_M is the Morison force as defined as Eq. (1). $\mathbf{A}(\infty)$ and \mathbf{F}_R can be obtained using the following equations:

$$\mathbf{A}(\infty) = \mathbf{A}(\omega) + \int_0^\infty \mathbf{R}(t) \frac{\sin(\omega t)}{\omega} dt \quad (12)$$

$$\mathbf{F}_R = -\int_0^\infty \mathbf{R}(\tau) \dot{\mathbf{X}}(t - \tau) d\tau \quad (13)$$

$$\mathbf{R}(t) = \frac{2}{\pi} \int_0^\infty \mathbf{B}(\omega) \cos(\omega t) d\omega \quad (14)$$

where $\mathbf{A}(\omega)$ and $\mathbf{B}(\omega)$ are the added mass and radiation damping matrices in the frequency domain and $\mathbf{R}(t)$ is the retardation function. A comparison of Eq. (10) with Eq. (11) showed that the heavy computation in the Cummins equation is due to \mathbf{F}_R . In the Morison equation, the radiation damping is excluded, and the last term of \mathbf{F}_M ,

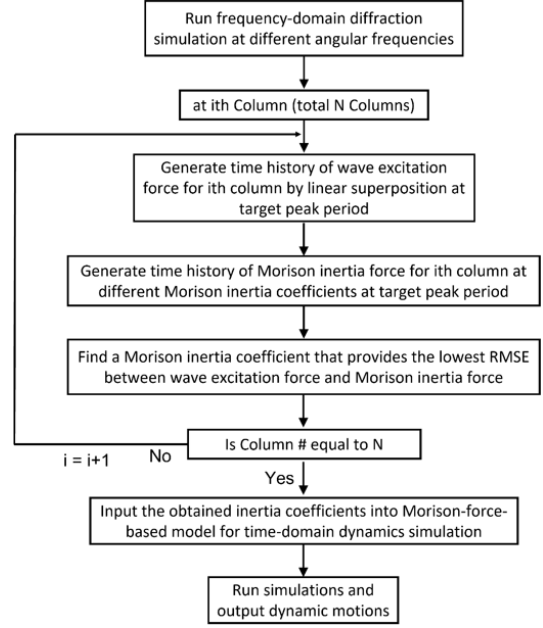


Fig. 3 Flowchart of the overall procedures to obtain EIC for the irregular wave cases and run time-domain simulations from the Morison equation-based model.

which is the viscous drag force, is not considered. Fig. 3 shows the overall procedures to evaluate EICs for the irregular wave cases and run time-domain simulations from the Morison-equation-based model.

4. Results and Discussions

The Results and Discussion section compares the wave forces on the OC4 semi-submersible FOWT platform and platform motions obtained by the Morison inertia force and the wave excitation force by the potential theory.

4.1 Wave Force Under Regular Waves

Figs. 4–5 show the total horizontal and vertical excitation forces and Morison inertia forces with a fixed inertia coefficient of two and corresponding phase angles. The total forces were calculated at different regular wave frequencies and directions. The inertia coefficient was fixed to two, a representative value for cylindrical

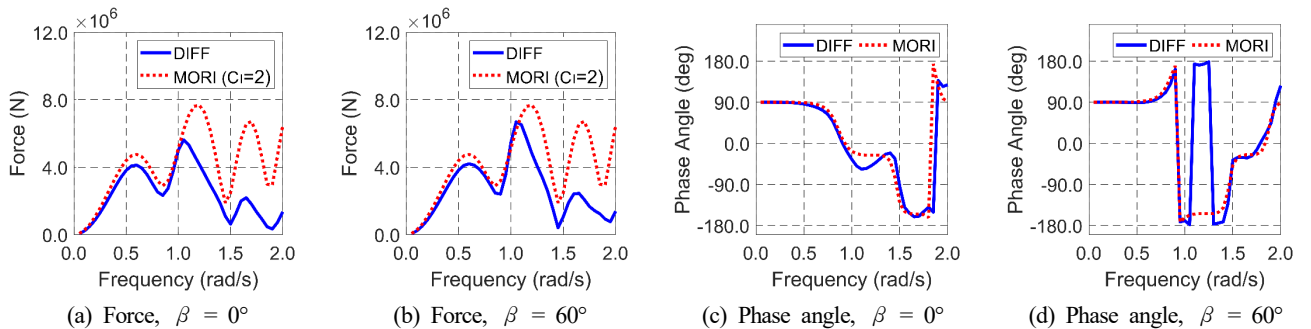


Fig. 4 Comparison of the horizontal inertia force ($C_l = 2$) and wave excitation forces and corresponding phase angles at different regular wave frequencies and wave headings.

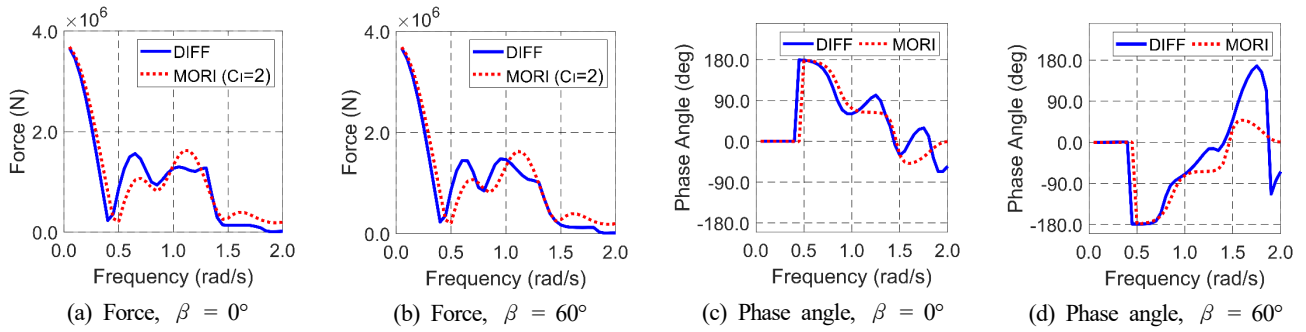


Fig. 5 Comparison of the vertical inertia force ($C_I = 2$) and wave excitation forces and corresponding phase angles at different regular wave frequencies and wave headings.

objects. DIFF and MORI in the legends denote components related to the 3D potential theory and Morison equation. As shown in Fig. 4, the magnitudes of the horizontal forces coincide at the wave frequencies of lower than 1.0 rad/s, while the inertia force tends to be exaggerated at higher frequencies because of large diffraction and interaction between columns (i.e., wake effects). Although there is a large difference in the forces in the high-frequency region, the phase angles of the inertia forces are well matched with those of the excitation force. As shown in Fig. 5, the magnitudes and phases of the vertical forces are well matched up to 1.5 rad/s, even if some phase differences are observed in higher frequencies. These results show that if the magnitude of the inertia force is corrected by introducing the concept of the EIC, the Morison inertia force can be a good option for wave force calculation without losing significant accuracy while minimizing the computational cost.

Fig. 6 shows the EICs at different regular wave frequencies and wave directions. In this process, the force of each column obtained by two methods was compared, and the EIC was obtained for each column using Eqs. (7)–(8). C1–C4 in the legends denote Columns 1–4. As shown in Fig. 6 (a)–(b), the horizontal EICs of all columns tend to decrease as the wave frequency increases. As shown in Fig. 6 (c)–(d), the vertical EICs also tend to decrease as the wave frequency increases, except for the central column (Column 1). This is because the inertia force of Column 1 is based on the wave kinematics estimated at the center of the column ($z = -10$ m), which cannot represent vertical inertia force accurately. Nevertheless, the given method can still result in comparable results by introducing the concept of EIC.

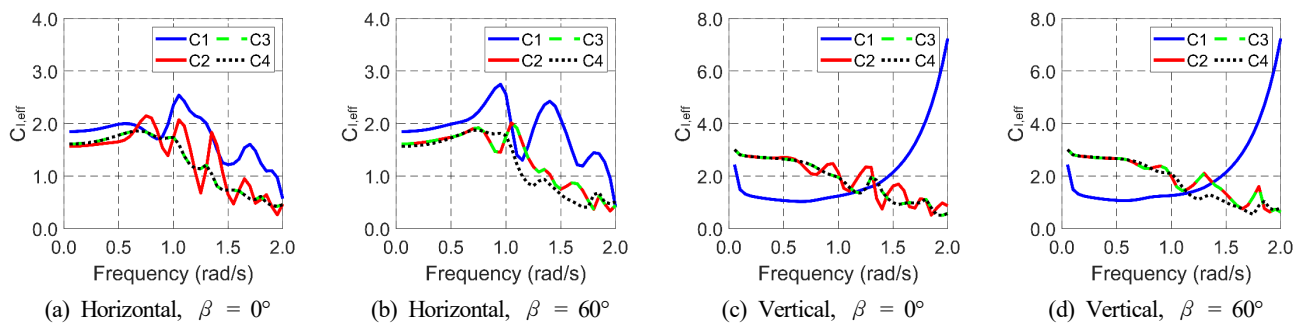


Fig. 6 Effective horizontal (a)–(b) and vertical (c)–(d) inertia coefficients ($C_{I,eff}$) of Columns 1–4 (C1–C4) at different regular wave frequencies and wave directions.

4.2 Wave Force Under Random Waves

Similar comparisons were made under random waves. The time histories of random waves were produced by superposing regular wave components from the PM spectrum, and the time histories of the wave forces were obtained. Figs. 7–8 show the time history comparison of horizontal and vertical wave forces under random waves at different peak periods and wave directions. The wave excitation force, inertia force with a fixed inertia coefficient of 2, and the inertia force with the EIC obtained by Eq. (9) were compared. In addition, a three-hour simulation for each wave condition was considered to acquire EIC, and the time histories of the first 300 s are only presented for a better time-history comparison. As shown in Fig. 7, for the horizontal force, a representative inertia coefficient of 2 was sufficient when the peak period was large (i.e., 15 s) and the wave direction was 0°. On the other hand, a significant overestimation in force was observed in the inertia force with a representative inertia coefficient at a low peak period (i.e., 6 s) and wave direction of 60°. This overestimation was corrected using EIC. With EIC, the time history of the inertia force showed good agreement with that of the wave excitation force. As shown in Fig. 8, similar correction effects were also valid for the vertical wave forces because the EIC significantly reduces the error between the two methods. In addition, estimating the EIC using RMSE between the wave excitation force and the Morison inertia force was acceptable.

Fig. 9 shows the EICs under random waves at different peak periods and wave directions. The trends and magnitudes are similar to those in Fig. 6 under regular waves. The EICs under random waves show more smothered results. This makes sense because random waves consider

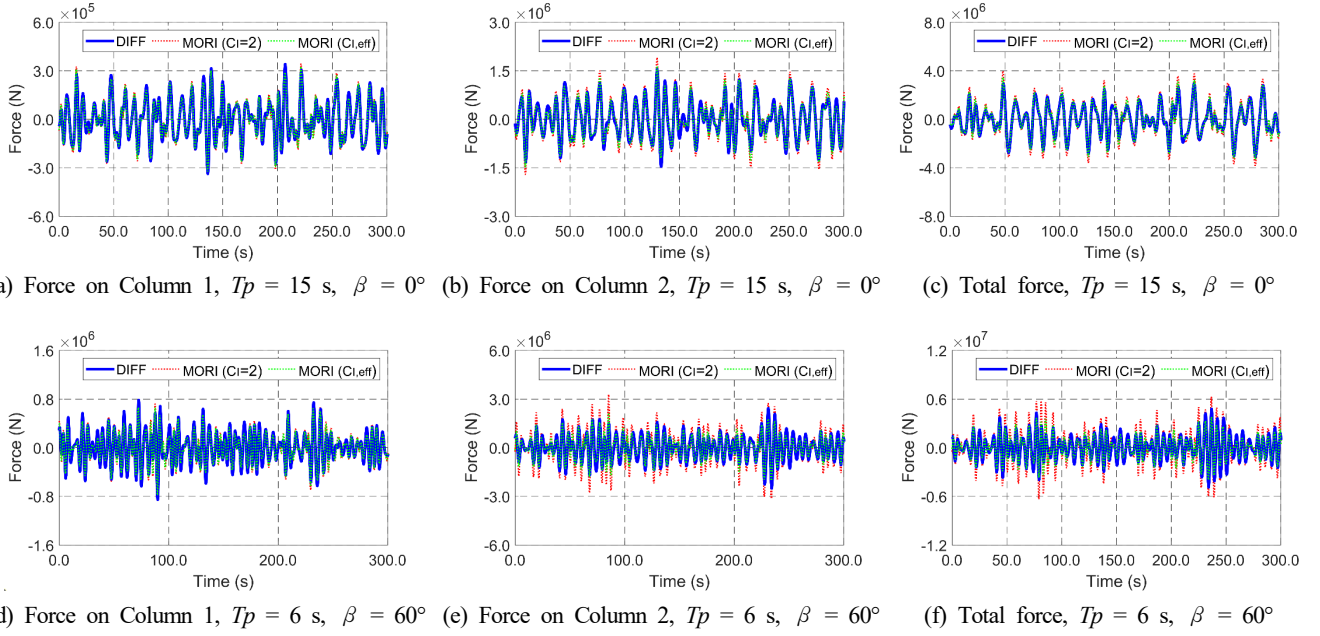


Fig. 7 Time histories of the horizontal inertia forces from the Morison equation and wave excitation forces from potential theory at different peak periods and wave directions.

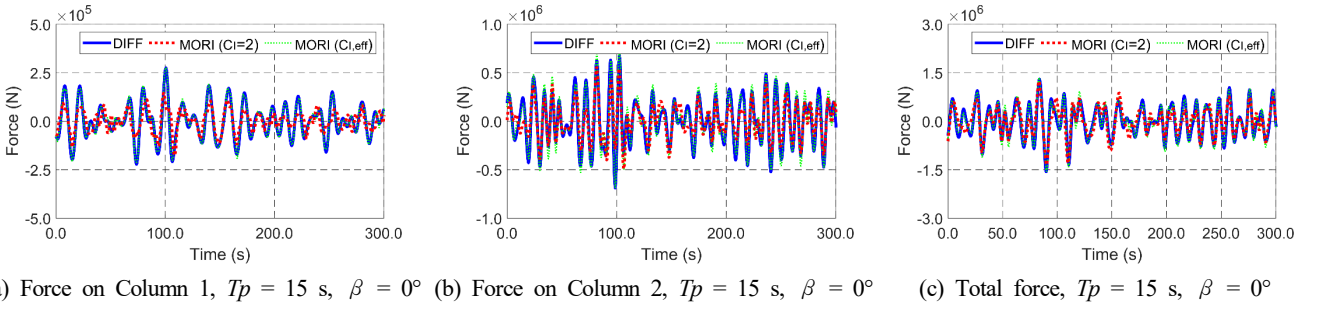


Fig. 8 Time histories of the vertical inertia forces from the Morison equation and wave excitation forces from potential theory.

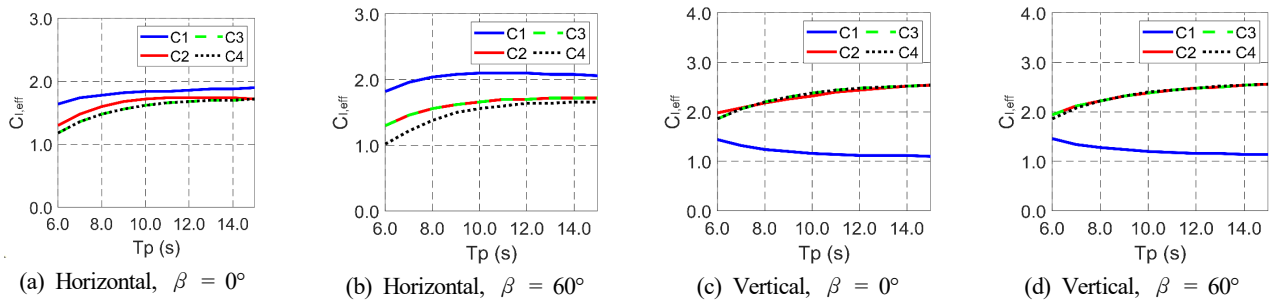


Fig. 9 Effective horizontal (a-b) and vertical (c-d) inertia coefficients ($C_{i,eff}$) of Columns 1-4 (C1-C4) under random waves at different peak periods and wave directions.



Fig. 10 Error of the horizontal (a) and vertical (b) inertia forces at different peak periods and wave directions (the values are interpolated).

many frequency components.

Fig. 10 summarizes the errors of inertia force. The error was calculated by comparing the percentage difference between the standard deviation of the wave excitation force and that of the inertia force with EIC. Some errors up to 24.94% at a peak period of 6 s and wave direction of 45° were obtained for horizontal wave force. On the other hand, the errors in the horizontal force were reduced significantly as the peak period increased. For example, the errors at a wave heading of 60° decreased to 6.15% and 0.26% at peak periods of 8 s and 15 s. Regarding the vertical force, the error is within 10% regardless of the peak period and wave direction.

4.3 Dynamic Response of Platform Under Random Waves

Sections 4.1–4.2 show the feasibility of the EIC concept. The method can be used for fixed cylindrical structures because the horizontal and vertical forces are correctly estimated by correcting the inertial forces in the Morison equation. In Section 4.3, the EIC concept was further checked for floating structures by comparing the motions between the two methods. A commercial time-domain dynamics simulation program, OrcaFlex, was used to obtain the dynamic motions of the OC4 semi-submersible FOWT platform. The models based on diffraction theory and the Morison approach were established separately, as expressed in Eqs. (10)–(11). Each column was discretized into 1-m elements in the Morison approach, and the Morison inertia coefficient was inputted separately. Note that each column has the same inertia coefficient. The pressure correction in vertical force, $P_L A_T$ in Eq. (3), was inputted as an external force after precalculation. For a moving body, an added mass coefficient needs to be inputted, which was obtained by subtracting one from the obtained inertia coefficient (i.e., effective added mass coefficient). In the comparisons, only heave, roll, and pitch degree-of-freedom (DOF)

motions were considered, while the other DOF motions were constrained because the mooring lines were not modeled. In this demonstration, 10% damping was considered in the heave, roll, and pitch DOFs, which excludes the influence of added mass because the effective added mass coefficient varies according to given environmental conditions. A time-domain simulation was conducted with a simulation time of one hour with a fixed time interval of 0.1 s. Random waves were generated by superposing 200 regular waves from the Jonswap wave spectrum with an enhancement parameter of two. In addition, the computational time of the Morison-equation-based model was approximately 25% faster than the Cummins-equation-based approach. On the other hand, it can vary depending on the division of the Morison element. In the present case, 1-m elements were used for Morison force calculations, which is considered acceptable. The Morison equation can be much more time-efficient if the proper element size is selected.

Figs. 11–12 show the time histories and spectra of heave and pitch motions based on models with the Morison equation and potential theory at different peak periods. In this demonstration, the wave heading was fixed to 0° . When the peak period was 15 s, a large discrepancy was observed between heave motions based on the Morison equation with a fixed inertia coefficient of two and diffraction theory, which is corrected by the EIC concept. The pitch motion of the current model is based primarily on the surge force, which results in a good comparison regardless of the inertia coefficient correction. At a peak period of 6 s, however, moderate differences were observed in both heave and pitch motions. Various coupling effects were observed in the model with Morison force because the Morison equation considers instantaneous positions instead of a fixed location for kinematics calculations as in potential theory. Although there is no wave energy at the lower frequency region, the pitch spectra at a peak

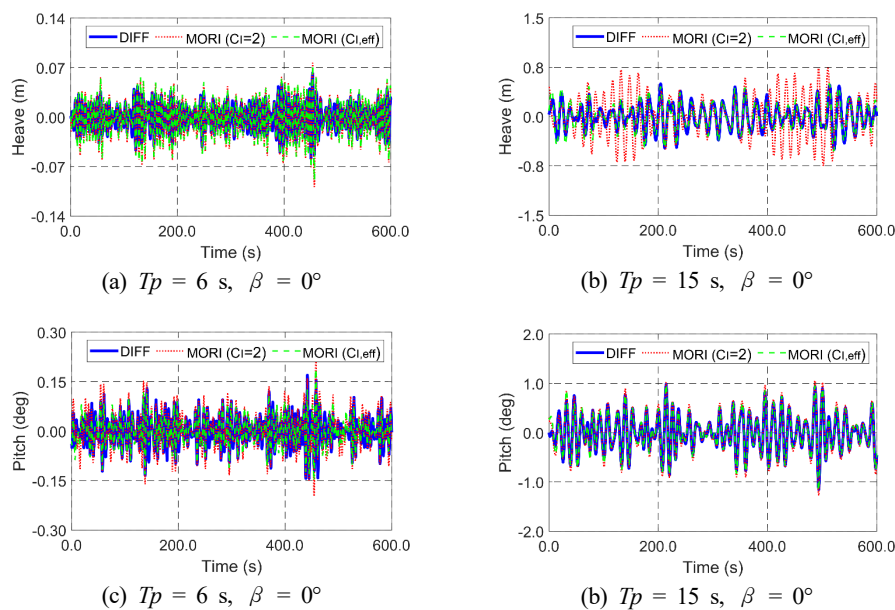


Fig. 11 Time histories of the heave (a)–(b) and pitch motions (c)–(d) based on models with Morison equation and potential theory at different peak periods.

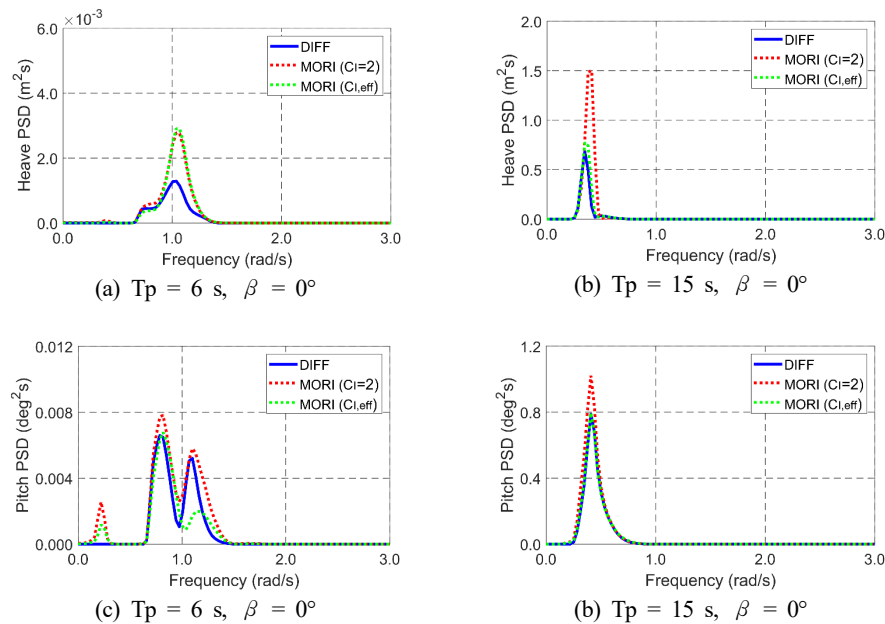


Fig. 12 Spectra of the heave (a)–(b) and pitch motions (c)–(d) based on models with the Morison equation and potential theory at different peak periods.

period of 6 s showed a low-frequency peak at the pitch natural frequency only from Morison models. A thorough study still needs to validate the EIC concept under different wave conditions and floating structures. The Morison equation can also be extended to include second-order wave inertia forces, as reported by Kim and Chen (1994).

5. Conclusions

This paper introduced the concept of EIC in the Morison equation to make a better estimation of the wave forces and platform motions through the Morison equation. The OC4 semi-submersible FOWT platform was considered. The EIC was estimated by comparing the wave excitation force by potential theory and inertia force using the Morison equation. Various regular and random waves at different periods and directions were considered. First, horizontal and vertical (surge and heave) wave forces were assessed at various regular wave frequencies. Large errors in the horizontal force were observed with a fixed inertia coefficient of two. The errors tended to increase when the wave direction and wave frequency increased, and the EIC decreased the discrepancy between the two methods. Although similar trends were observed under random waves to regular waves, a smoother EIC was obtained because it considers many wave frequency components. The adoption of EIC reduces the difference between the two forces significantly. The OC4 platform motions were then compared under wave forces using two methods. The motion comparison results show acceptable agreement at the longer wave case. These results show that the concept of EIC can play some role in mass simulations in the early design stage to provide a range of design parameters quickly so that the design optimization can be done in a time-efficient manner. A rigorous study still needs to be carried out under various wave

conditions and other floating structures to assess the feasibility of the EIC concept.

Conflict of Interest

Chungkuk Jin and MooHyun Kim serve as editorial board members of the Journal of Ocean Engineering and Technology, but they had no role in the decision to publish this article. No potential conflict of interest relevant to this article was reported.

References

- Abbasnia, A., & Soares, C. G. (2018). Fully nonlinear simulation of wave interaction with a cylindrical wave energy converter in a numerical wave tank. *Ocean engineering*, 152, 210–222. <https://doi.org/10.1016/j.oceaneng.2018.01.009>
- Boccotti, P., Arena, F., Fiamma, V., & Romolo, A. (2013). Two small-scale field experiments on the effectiveness of Morison's equation. *Ocean engineering*, 57, 141–149. <https://doi.org/10.1016/j.oceaneng.2012.08.011>
- Chakrabarti, S. K., & Tam, W. A. (1975). Interaction of waves with large vertical cylinder. *Journal of Ship Research*, 19(01), 23–33. <https://doi.org/10.5957/jsr.1975.19.1.23>
- Chang, S., Huang, W., Sun, H., & Li, L. (2019). Numerical investigation of secondary load cycle and ringing response of a vertical cylinder. *Applied Ocean Research*, 91, 101872. <https://doi.org/10.1016/j.apor.2019.101872>
- Chen, B., Lu, L., Greated, C. A., & Kang, H. (2015). Investigation of wave forces on partially submerged horizontal cylinders by numerical simulation. *Ocean engineering*, 107, 23–31.

- <https://doi.org/10.1016/j.oceaneng.2015.07.026>
- Chung, J. S. (2018). Morison equation in practice and hydrodynamic validity. *International Journal of Offshore and Polar Engineering*, 28(01), 11–18. <https://doi.org/10.17736/ijope.2018.jc740>
- Dafnakis, P., Bhalla, A. P. S., Sirigu, S. A., Bonfanti, M., Bracco, G., & Mattiazzo, G. (2020). Comparison of wave-structure interaction dynamics of a submerged cylindrical point absorber with three degrees of freedom using potential flow and computational fluid dynamics models. *Physics of Fluids*, 32(9). <https://doi.org/10.1063/5.0022401>
- Faltinsen, O. (1993). *Sea loads on ships and offshore structures* (Vol. 1). Cambridge university press.
- González, G. G., Urbán, A. M., Horcas, S. G., Roqueta, L. V. I., & Blanco, S. H. (2021). Evaluation of a lowfidelity hydrodynamic modelling approach for a floating wind turbine mounted on an enhanced spar. *Journal of Physics: Conference Series*, 2018(1), [012019]. <https://doi.org/10.1088/1742-6596/2018/1/012019>
- Jin, C. (2022). Comparison of Potential Theory and Morison Equation for Deformable Horizontal Cylinders. *Sustainable Marine Structures*, 4(2), 1–10. <https://doi.org/10.36956/sms.v4i2.492>
- Jin, C., Bakti, F. P., & Kim, M. (2021). Time-domain coupled dynamic simulation for SFT-mooring-train interaction in waves and earthquakes. *Marine Structures*, 75, 102883. <https://doi.org/10.1016/j.marstruc.2020.102883>
- Jin, C., Kim, G.-J., Kim, S.-J., Kim, M., & Kwak, H.-G. (2023). Discrete-module-beam-based hydro-elasticity simulations for moored submerged floating tunnel under regular and random wave excitations. *Engineering Structures*, 275, 115198. <https://doi.org/10.1016/j.engstruct.2022.115198>
- Kim, M., & Chen, W. (1994). Slender-body approximation for slowly-varying wave loads in multi-directional waves. *Applied Ocean Research*, 16(3), 141–163. [https://doi.org/10.1016/0141-1187\(94\)90025-6](https://doi.org/10.1016/0141-1187(94)90025-6)
- Kvittem, M. I., Bachynski, E. E., & Moan, T. (2012). Effects of hydrodynamic modelling in fully coupled simulations of a semi-submersible wind turbine. *Energy Procedia*, 24, 351–362. <https://doi.org/10.1016/j.egypro.2012.06.118>
- Lee, C.-H. (1995). *WAMIT theory manual* (Report No. 95-2). Massachusetts Institute of Technology, Department of Ocean Engineering.
- Li, Y. S., Zhan, S., & Lau, S. (1997). In-line response of a horizontal cylinder in regular and random waves. *Journal of Fluids and Structures*, 11(1), 73–87. <https://doi.org/10.1006/jfls.1996.0067>
- Lin, H., Xiang, Y., Yang, Y., & Chen, Z. (2018). Dynamic response analysis for submerged floating tunnel due to fluid-vehicle-tunnel interaction. *Ocean Engineering*, 166, 290–301. <https://doi.org/10.1016/j.oceaneng.2018.08.023>
- Morison, J., Johnson, J. W., & Schaaf, S. A. (1950). The force exerted by surface waves on piles. *Journal of Petroleum Technology*, 2(05), 149–154. <https://doi.org/10.2118/950149-G>
- Paulsen, B. T., Bredmose, H., Bingham, H. B., & Jacobsen, N. G. (2014). Forcing of a bottom-mounted circular cylinder by steep regular water waves at finite depth. *Journal of Fluid Mechanics*, 755, 1–34. <https://doi.org/10.1017/jfm.2014.386>
- Robertson, A., Jonkman, J., Masciola, M., Song, H., Goupee, A., Coulling, A., & Luan, C. (2014). *Definition of the semi-submersible floating system for phase II of OC4*. United States. <https://doi.org/10.2172/1155123>
- Takata, T., Takaoka, M., Gonçalves, R. T., Houtani, H., Yoshimura, Y., Hara, K., Oh, S., Dotta, R., Malta, E. B., Iijima, K., & H. Suzuki (2021). Dynamic Behavior of a Flexible Multi-Column FOWT in Regular Waves. *Journal of Marine Science and Engineering*, 9(2), 124. <https://doi.org/10.3390/jmse9020124>

Author ORCIDs

Author name	ORCID
Jin, Chungkuk	0000-0002-5446-0534
Lee, Ikjae	0000-0002-7701-2996
Park, JeongYong	0000-0002-7771-8083
Kim, MooHyun	0000-0001-5793-3707

Point Cloud-Based Spatial Environment Development for Near Real-Time Erection Simulation in Shipyards

Yeon-Jun Kim¹, SeungYeol Wang¹, Jaewon Jang², Bon-Yeong Park³, Dong-Kun Lee³ and Daekyun Oh^{2,3}

¹Graduate Student, Department of Ocean System Engineering, Mokpo National Maritime University, Mokpo, Korea

²Researcher, Sustainable Ship Technology Center, Industry-Academy Cooperation Foundation of Mokpo National Maritime University, Mokpo, Korea

³Professor, Department of Naval Architecture and Ocean Engineering, Mokpo National Maritime University, Mokpo, Korea

KEYWORDS: Block Erection, Point Cloud, Near Real-Time, Virtual Reality, Laser Scanning

ABSTRACT: Interference and collisions often occur in the loading process at shipyards. Existing simulation methods focus primarily on resource processes and schedules, and there is a lack of real-time reflection in the complex and highly variable loading process. This study aims to develop a spatial environment incorporating real-time product data, such as hulls, and confirms its effectiveness by simulating various construction scenarios. As a method, a near real-time spatial environment based on broadband laser scanning was established, with the situation of loading heavy cargo assumed when converting an existing ship into an LNG dual-fuel propulsion ship. A case study simulation of near-real-time cargo loading processes was then conducted using Unity 3D to confirm the interference and collision risks within the spatial environment. The results indicated that interference occurred in structures previously not identified in the design data, and a collision occurred during the loading object erection phase. The simulation confirmed that the identification of interference and collision risks during the erection phase highlights the need for a relocation or removal process of potential hazards before erection takes place. An improved erection simulation that integrates near real-time data could effectively prevent interference and collision risks.

1. Introduction

In Korea, active industrial activities are being carried out, but the incidence of industrial accidents is very high. As of 2021, industrial accidents in the manufacturing industry comprised 25.84 % of the total industrial accidents, the largest proportion among all industries, excluding industrial fields categorized as others. In terms of the industrial accident rate per 1,000 persons, which refers to the number of victims of industrial accidents per 1,000 regular workers, the shipbuilding industry has been reported to have the highest accident rate (MOEL, 2022). According to the data released by the Korea Occupational Safety and Health Agency (KOSHA), accidents caused by original cause materials are one of the most frequent types of serious accidents in the shipbuilding industry, with crane accidents constituting a major category of accidents due to original cause materials (Mline Studio, 2023). Crane accidents are caused mainly by inferences and collisions that occur frequently due to the complexity of the work site, including the target block, equipment, and previously erected blocks when block erection operation or block turnover

operation is performed using a crane in the shipbuilding process (Cha et al., 2009). Human accidents or problematic situations can occur if an inspection of the block erection process is not performed correctly in advance, which may lead to the necessity of cutting the interference member while the crane is holding a block (Cheon et al., 2013). The shipbuilding industry and researchers have used various methods, such as limitations on multi-level subcontracting, installation of crane collision prevention sensors, strengthening equipment management and field management supervision, and simulations, to prevent such problems (Cha et al., 2012; Hwang, 2013; MOEL, 2018). Among these approaches, simulations can verify processes and methods before applying them. Simulation-based manufacturing technologies have been emerging because they can play a major role in resolving various difficulties (e.g., process/method evaluation and production method/planning) before actual production and shipbuilding (Hwang, 2014; Lee et al., 2011).

Previous simulation research can be divided into scheduling simulations and safety evaluation simulations. Scheduling simulation studies mainly performed mutual verification simulations of processes

Received 26 September 2023, revised 9 November 2023, accepted 27 November 2023

Corresponding author Daekyun Oh: +82-61-240-7318, dkoh@mmu.ac.kr

© 2023, The Korean Society of Ocean Engineers

This is an open access article distributed under the terms of the creative commons attribution non-commercial license (<http://creativecommons.org/licenses/by-nc/4.0>) which permits unrestricted non-commercial use, distribution, and reproduction in any medium, provided the original work is properly cited.

and scheduling and facility simulations using GIS (Geographic information system) data (Heo et al., 2012; Hwang et al., 2010; Lee and Hwang, 2011). Research on safety evaluation simulations has been conducted mainly on product visualization and evaluation, simulations of crane lifting and the erection of blocks, simulations of the control of blocks and logistics control, and virtual reality (VR) simulations (Ham et al., 2020; Heo et al., 2012). These simulation studies focused mainly on scheduling and VR training. They did not sufficiently reflect the real-time data of the complex and significantly variable spatial environment of the erection process. The lack of reflection of real-time data makes it challenging to identify the risk factors for the erection process when there are differences between design data and the existing structure for various reasons, such as malfunctions of the design data, malfunctions of fieldwork, changes in work scheduling, and the complexity of the work site. Suppose an erection operation is performed without identifying the risk factors involved in the erection process in advance. In that case, equipment malfunctions and accidents can occur due to differences between the design data and the existing structure, which may lead to project delays or large-scale industrial accidents. On the other hand, in relation to the characteristics of shipbuilding, it is difficult to reflect real-time data because of practical difficulties, such as the huge size of a ship as a product and the complexity of the work site, where many processes are performed simultaneously at multiple positions. Therefore, reflecting near real-time data that maximally replicates real-time data is a feasible approach.

Therefore, this study aimed to obtain near real-time data of a ship under construction set as the simulation product by broadband laser scanning and construct the spatial environment that reflects the field of shipbuilding near real-time using the data of the crane and the dock, which are resources of the shipyards. This study verified the effectiveness of the simulation method developed through a simulation case study of the erection process based on the improved near real-time erection spatial environment.

2. Methods

This study constructed the spatial environment by reflecting product and resource data and conducted an erection process simulation using Unity 3D (Unity, n.d.), a commercial simulation platform.

The spatial environment is the simulation environment that reflects the resource data based on near real-time product and design data. This study was based on Kim et al. (2007) and Pfrommer et al. (2013) regarding the simulation elements. The erection process was set as the process. A jib crane and a dock were set as the resources required for the erection process, and the hull of a ship under construction was set as the product. Considering that the spatial environment of products, such as ships, is highly variable, near real-time data was reflected in the product data using a broadband laser scanner. In addition, resource data were constructed based on design data because resources, such as a crane or a dock, have low variability. This newly devised method

allows a simulation developer to perform a simulation by replacing only the product data in the existing spatial environment when the erection process simulation is required.

2.1 Product Data of a Ship under Construction

As mentioned in the previous section, there may be discrepancies between the design and product data of a ship under construction. A measurement method for acquiring near real-time data on the ship is required to solve this problem. Regarding the criteria for selecting a measurement method, it is necessary to consider the need for fast measurements, the huge size of the product, and the characteristics of outdoor processes related to the shipbuilding characteristics. Commonly used measurement techniques include human, photogrammetry, optical, and laser measurements. Among these methods, a suitable method for measuring a ship was selected. Measurements by humans were considered unfeasible because they required a large number of people and took a long time (Kwon, 2009). The photogrammetry method has low accuracy with errors in cm ~ m units because there is no medium for direct measurements (Che, 2017). Hence, it was considered unsuitable for this study. Laser measurement can be used outdoors for fast and high-precision distance measurements compared to other methods because of the directivity and high reflectivity of laser beams. Therefore, it is used to acquire the shape data of large-scale facilities, such as buildings, bridges, ports, and ships (Bae et al., 2007; Park and Lee, 2022; Kwon, 2009). Accordingly, the laser measurement method was considered suitable for measuring a ship under construction (Bae et al., 2007; Park and Lee, 2022; Kwon, 2009).

In short, the laser measurement method was adopted to reflect near real-time product data. This method was used to acquire a 3D-built model from the point cloud of a ship under construction.

2.2 Resource of the Erection Process

The resource refers to the facilities related to the execution of a process. In this study, the facilities for the execution of the erection process were the erection position and the crane. The erection locations are divided mainly into a dry dock, a floating dock, and an inner wall. Among the three locations, the dry dock was selected to erect an LNG (liquefied natural gas) tank. In addition, a job crane was selected for the erection process. In this study, the dry dock and the jib crane data of job cranes with a hoisting load of 200 t were applied for the dock and crane.

2.3 Erection Process

The scenario postulated in this study is the process of erecting an LNG tank (Fig. 1(b)) in a dock (Fig. 1(a)) on the stern part of the ship named the Segeroho (Fig. 1(d)) using a crane shown in Fig. 1(c). Regarding the erection position of the LNG tank, considering the size of the tank, Fr. 4, C.L of the stern part of the shelter deck of the Segeroho was selected as the erection position (Fig. 2). The stern part of the boat deck of the Segeroho needed to be removed to erect the LNG tank. Therefore, the LNG tank erection process was carried out,

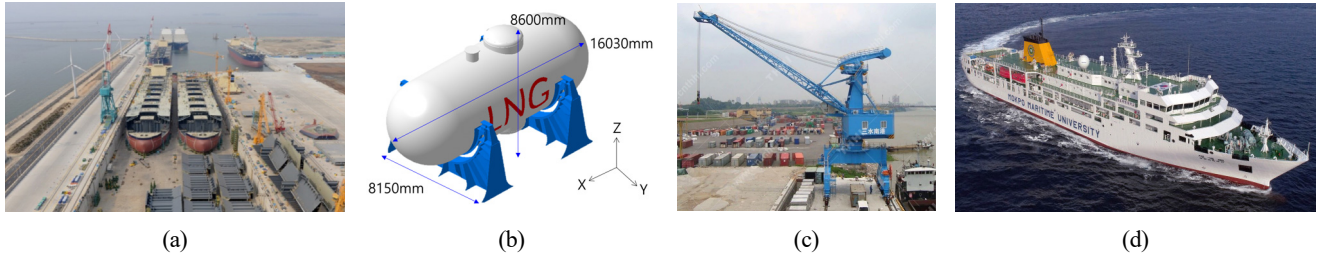


Fig. 1 Product and resource: (a) The Segeroho training ship (Product) (Sin, 2022); (b) Loading object LNG tank (Product); (c) Shipyard crane (Resource) (THHI. n.d.); (d) Shipyard dock (Resource) (Lee, 2017)

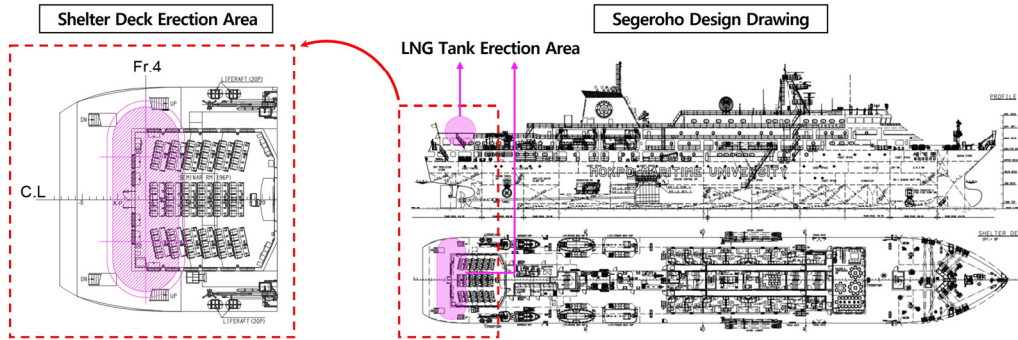


Fig. 2 LNG tank erection area in the Segeroho design data (MMU, n.d.)

where the stern part of the boat deck was removed before the LNG tank erection process.

3. Near Real-Time Erection Spatial Environment

Frequently, there are some dissimilarities between the design data and the existing structure of the ship waiting for the erection process for various reasons, such as a malfunction of fieldwork, changes in work scheduling, and the complexity of the work site. If the design data has low reliability, this results in frequent situations where erection is not carried out according to the erection plan because of structures not identified in the design data. Therefore, it is essential to obtain accurate design data.

This section describes the construction process of the near real-time spatial environment and a comparison of the design data and near real-time data. Regarding the near real-time data of the Segeroho, the simulation product in this study, a 3D-built model from a point cloud was obtained using broadband laser scanning. 3D modeling for the design data and resource model of the Segeroho was then performed based on the design drawing. The near real-time data and design data of the Segeroho, the product of this simulation, were then compared by comparing the models of near real-time data and design data through data matching. The data of the midship part ~ A.E. were reflected because the erection position of the LNG tank is the stern, half of the data. Fig. 3 outlines the construction process of the spatial environment.

3.1 Selection of the Laser Scanner and 3D Built-Model from Point Cloud

Laser scanning is a technology for measuring the shape of an object

in the form of 3D coordinates or point cloud data by shooting laser beams onto the surface of an object and capturing the laser beams reflected to the scanner (Lee, 2021). Selecting a laser scanner using the optimal measurement method and considering factors, such as the measurement distance, the object size, scanning speed, and measurement accuracy, is essential for acquiring 3D data efficiently (Lee et al., 2007). This study used a Leica RTC 360 laser scanner (Fig. 3) as the measurement method. RTC 360 uses waveform digitizer (WFD) technology that allows fast, high-precision, and long-distance measurements (Kim, 2013). RTC 360 is a high-performance laser scanner with an accuracy of 1.9 mm at a distance of 10 m, a maximum measurement distance of 130 m, and a scan rate of up to 2 million points per second.

The process of acquiring near-time data using the selected laser scanner is as follows. Regarding the scope of measurement, the erection position was used as the reference position. The boat deck (Fr. 4 – Fr. 28), the navigation bridge deck (Fr. 28 – Fr. 76), the compass deck (FR. 76 – Midship), the shelter deck (Fr. 2 – Fr. 22), and the starboard surface (Looking port, Midship ~ A.E) were determined as the scope of measurement. According to the determined scope of measurement, scanning was performed at 20 points, including eight points on the stern of the shelter deck of the Segeroho, six points on the open deck, and six points on the starboard surface in the direction of the ship from the quay wall (Fig. 4(a)).

The acquired point cloud data contained 368,982,640 points, and it was necessary to perform postprocessing to remove the unnecessary points and perform data matching. First, the initial registration was performed using the automatic registration function of Leica Cyclone Register 360 (Leica Geosystems, n.d.) software. The unnecessary data

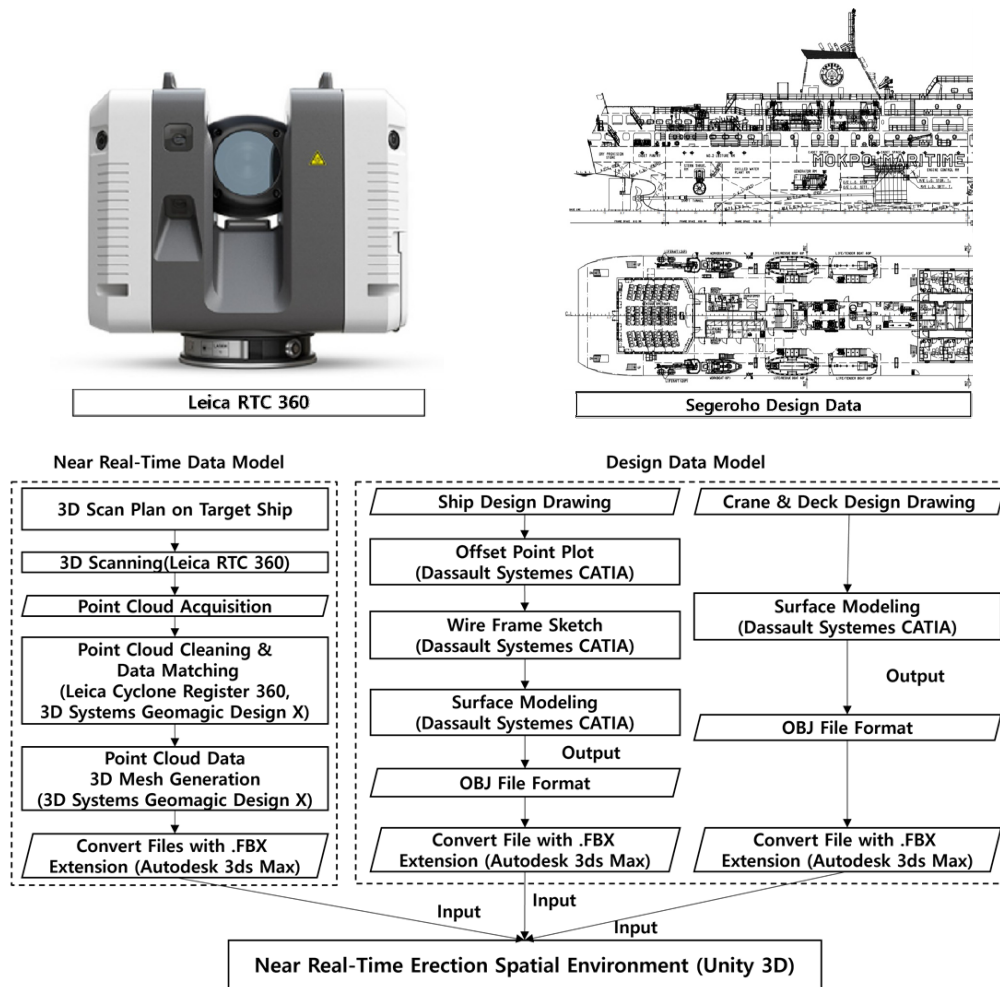


Fig. 3 Spatial environment configuration for near real-time erection simulation (Leica Geosystems, n.d.; MMU, n.d.)

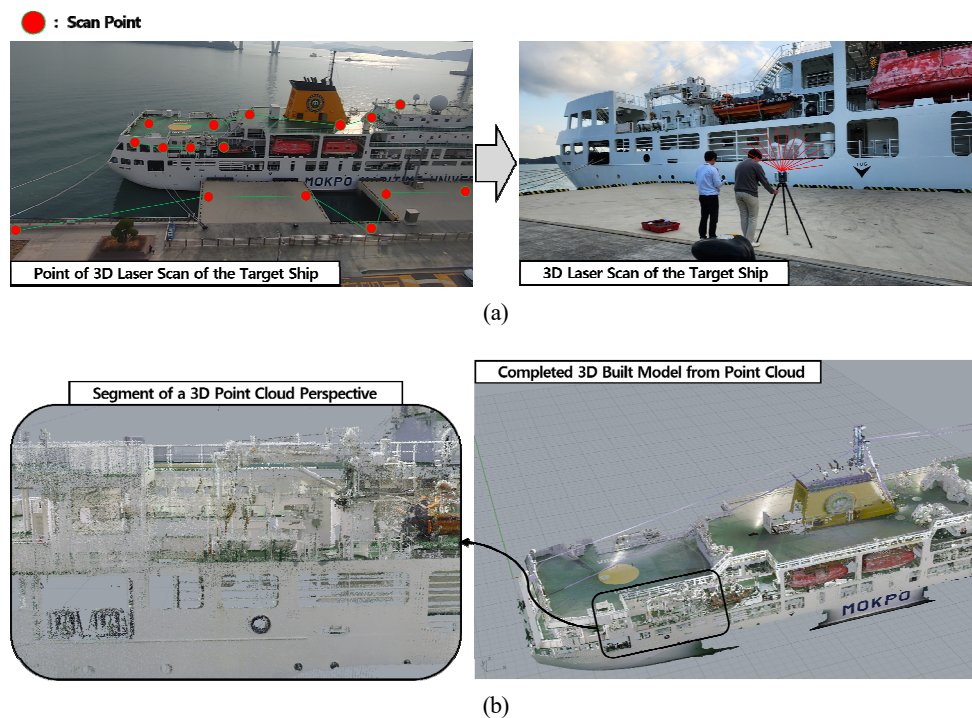


Fig. 4 Acquiring a point cloud model: (a) Scan plan and process of a 3D laser scan of the target ship; (b) Completed point cloud model through data matching and point cloud registration

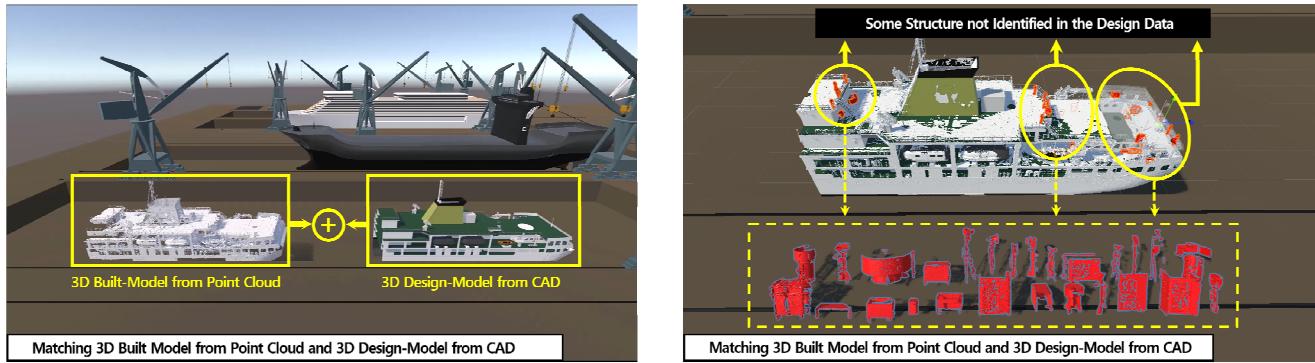


Fig. 5 3D design-model from CAD and 3D built-model from point cloud matching comparison

were removed, and the second registration process was performed using Geomagic Design X (3D Systems, n.d.) software. As a result, a 3D-built model from a point cloud composed of 17,643,199 points was finally acquired (Fig. 4(b)).

The time needed to generate the Built-Model from Point Cloud is as follows. Scanning took one minute and 26 seconds per point, and postprocessing the total acquired data, including data matching and removing unnecessary data, took approximately three hours. Among the processes of generating the built model from the point cloud, raw data import required the most time, and the postprocessing time varied according to the specifications and performance of the computers used. Generating 3D design and modeling data required considerable time (Lee, 2018). As for the time needed for the 3D CAD (Computer-aided design) modeling of equipment, the 3D modeling of the main engine takes three days, and the 3D modeling of a single part takes approximately one hour (Kang et al., 2011). In this study, the 3D design model from the CAD of the Segeroho took approximately one week to generate. Therefore, if the scanning method presented in this study is used to acquire the latest ship data, it can reduce the time needed to generate 3D models compared to existing modeling methods.

3.2 3D Design-Model from CAD

A 3D design model from CAD was generated to compare the structural differences between the 3D-built model from the point cloud and the design data. This 3D design model was generated by 3D Modeling on the design data of the Segeroho using CATIA (Dassault Systems, n.d.), a type of CAD software.

3.3 Comparison of 3D Design-Model from CAD and 3D Built-Model from Point Cloud

The software used to construct the spatial environment was Unity 3D (Unity, n.d.), which is commonly used to develop simulations. Unity 3D enables users to develop simulations intuitively and simply because it supports various major platforms and technologies (Ki et al., 2020). In addition, Unity 3D permits simulation developers to achieve their desired results using diverse methods because it allows the asset developers to integrate various technologies (Lee, 2022).

The 3D-built model from the point cloud in Unity 3D was used by first rendering the data into a mesh using Geomagic Design X. After

the data was exported into the FBX format, it was imported into Unity. The FBX extension is suitable for jointing objects, specifying collision areas, and constructing scripts because the elements of the hierarchical structure designed separately in CAD are separated into individual parts, and the classes used in CAD are applied. In addition, the scale of CAD software is applied consistently, and the pivot set for each part is also applied consistently.

The 3D design model from CAD and the 3D-built model from the point cloud were compared by data matching on the Unity platform. As a result, 26 structures not identified in the 3D design model from CAD were identified from the 3D-built model from the point cloud. In Fig. 5, the red shapes represent the structures not identified in the 3D design model from CAD. These structures not identified in the design data are risk factors predictive of inference and collisions in the erection process. Section 4 presents the simulation process conducted by reflecting near real-time data to examine the impact of the risk factors on the erection process.

4. Improved Erection Process Simulation

This section describes the process of conducting the erection process simulation that was improved compared to existing simulations. This simulation was carried out by applying the spatial environment to the erection process plan established based on the jib crane loading manual and the design data of the Segeroho. Generally, an erection process plan is established according to design data based on the crane loading manual. Suppose the erection is performed according to the erection plan based on the design data. In that case, interference or a collision can occur due to structures not identified in the 3D design model from CAD but identified from the 3D-built model from the point cloud. Therefore, Section 4.1 presents an overview of the system of the inference and collision risk identification function generated by simulation to verify the erection process in advance for the reasons mentioned above (Fig. 6).

4.1 Overview of the Improved Erection Process Simulation System

The physical effects were reflected in the spatial environment using C# Script and components, such as Collider, Rigidbody, and Joint, constructed through the NVIDIA PhysX engine (NVIDIA, n.d.) on the

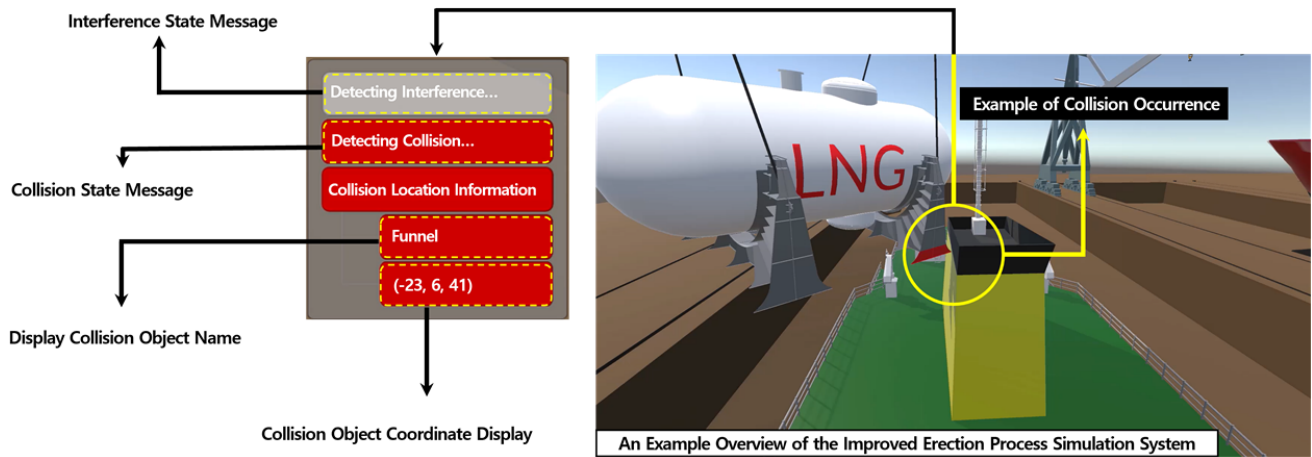


Fig. 6 Overview of the improved erection process simulation system implemented in Unity 3D

Unity 3D platform. An example of the functions generated through the spatial environment is identifying the risks for interference and collisions when a loading object is erected. First, interference refers to the existence of a structure that interferes with the movement of objects with a radius of motion, such as a crane. The radius of motion for each dynamic object on the ship was represented in the spatial environment to make it possible to check the presence of interference structures or the occurrence of interference. In addition, the spatial environment was constructed in such a way that the radius of motion of each dynamic object will be displayed in red to confirm the occurrence of interference visually when there is a structure within the radius of motion. Furthermore, the presence or absence of interference is displayed in the message window through the User Interface (UI), as shown in (Fig. 7(a)).

The collision check function was designed to detect the collision of objects using the Collider component. In addition, through C# Script, it was designed to allow the visual identification of the occurrence of collisions between objects. In Fig. 7(b), the position of collision occurrence is indicated in red, and the collision status, the name of the

collision object, and the location coordinates of the collision occurrence position are displayed in the message window through the UI.

4.2 Improved Erection Process Simulation – Occurrence of Interference

In the near real-time erection process, there was interference with the working radius of the deck crane mounted on the stern part of the shelter deck before the LNG tank erection process began, as shown in Fig. 8(a). When interference occurred, the silhouette of the LNG tank appeared on the expected LNG tank erection position, and the working radius of the deck crane was activated. Hence, it was possible to identify the interference visually. Suppose the erection process is done without taking measures to resolve the inference problem. In that case, there is a limitation on the rotation angle of the deck crane mounted on the stern when LNG tank erection is performed. Consequently, if the deck crane overrotates within the limited range, it collides with the LNG tank. Fig. 8(b) shows the result of removing the interference structure to prevent interference with the operation of the deck crane before erecting the LNG tank.

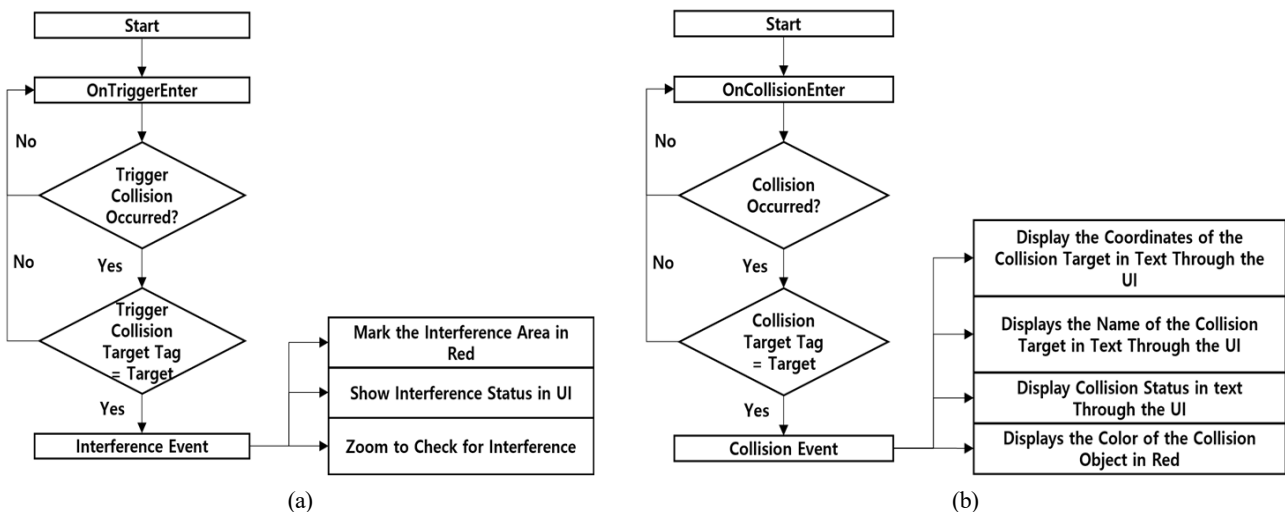


Fig. 7 Implementation of functions through script and PhysX engine: (a) Interference check function process; (b) Collision check function process

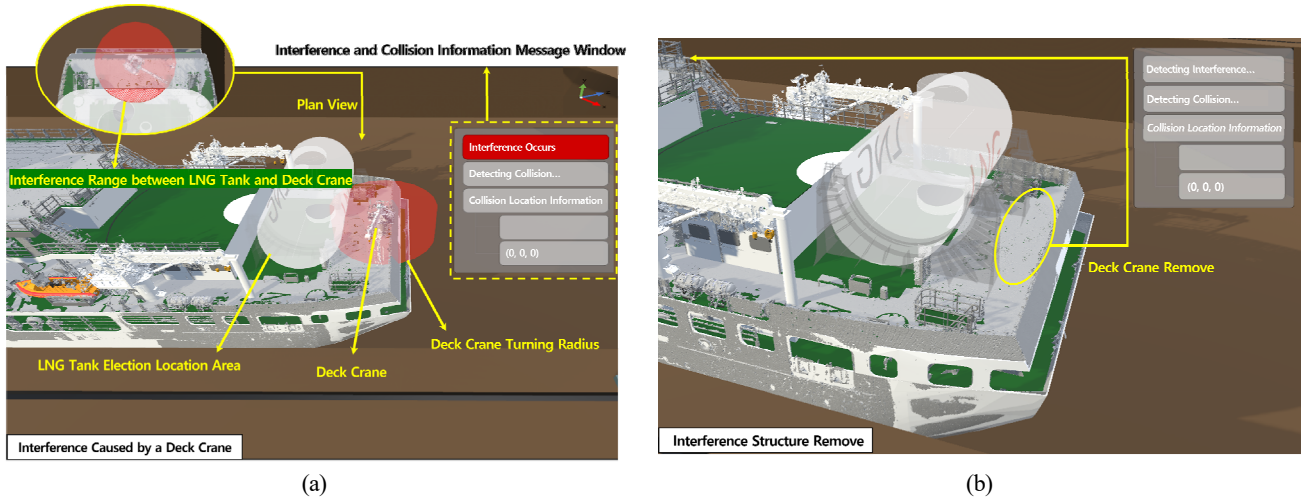


Fig. 8 Interference occurs: (a) Interference before loading starts; (b) Interference structure is removed

4.3 Improved Erection Process Simulation – Occurrence of Collision

The LNG tank erection process is performed as follows. First, the job crane rotates in the direction of where the LNG tank is located, and the tank is loaded after it is hooked to the crane. Next, the crane rotates toward the erection position, moving to the erection position with the LNG tank hooked to the crane. The crane is matched with the erection position in the horizontal distance. As the jib angle increases, the LNG tank is located on the vertical line of the erection position. Finally, the LNG tank is lowered and placed on the erection position, as shown in Fig. 9.

As a result of the simulation of the LNG tank erection process, through the 3D-built model from the point cloud, a collision occurred

because two outdoor units among the structures were not identified in the 3D design model from CAD while the LNG tank was lowered on the erection position. These results showed that the LNG tank erection process necessitates the removal or relocation of structures, potentially causing collisions before the erection process. Fig. 9 shows the erection simulation process.

5. Conclusions

In this study, the spatial environment of the complex and highly variable erection process was constructed based on point cloud data by reflecting near real-time product data. In addition, a case study through improved erection process simulation was conducted based on the near

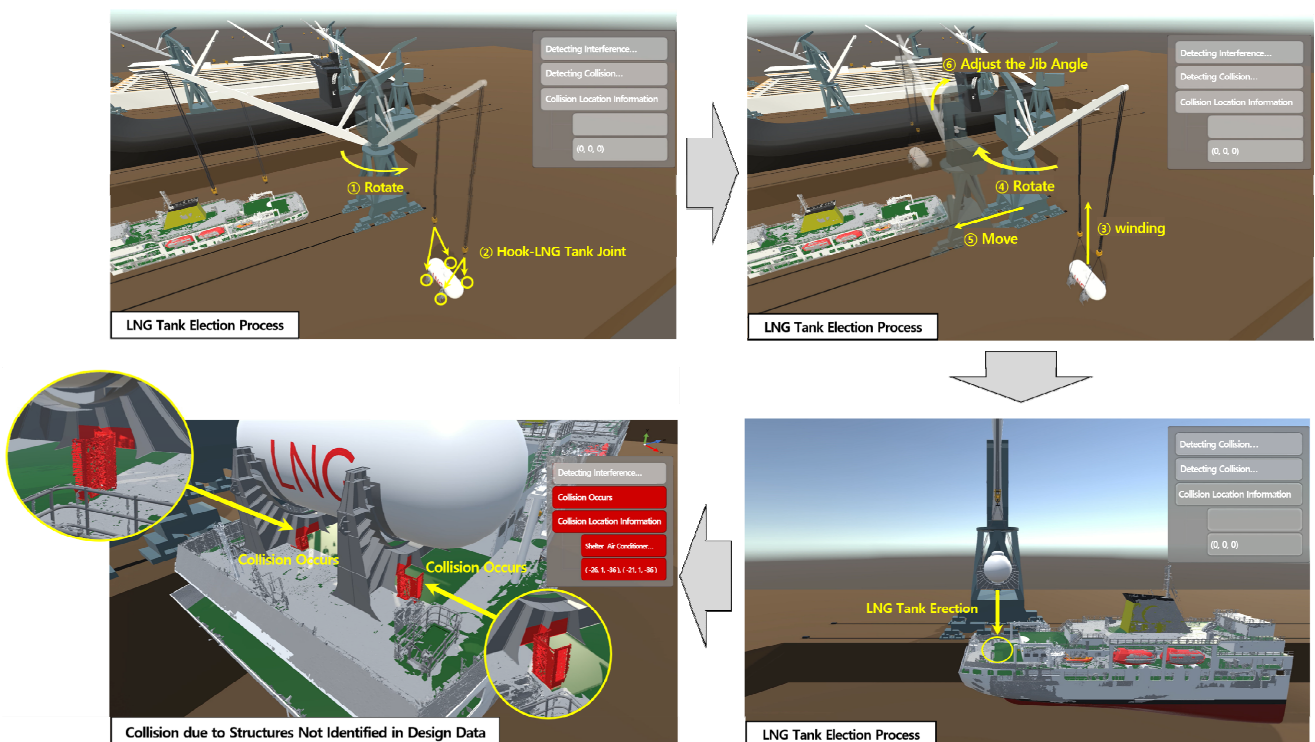


Fig. 9 Collision due to structures not identified in the design data during LNG tank erection

real-time erection spatial environment. A comparison of the 3D built model from the point cloud with the 3D design model from CAD revealed 26 structures not identified previously in the 3D design model from CAD that were identified from the 3D built model from the point cloud. A simulation-based case study of the near real-time erection process was conducted based on Unity 3D to assess the impact of the structures not identified in the design data on the erection process. Through the verification of improved erection process simulation, interference occurred with the operation of the deck crane when an LNG tank was installed. A collision occurred when the LNG tank erection process was performed because of two outdoor units not previously identified in the 3D design model from CAD. This simulation case analysis verified the necessity of the relocation process for structures potentially causing interference or a collision. On the other hand, modifications to the jib crane loading manual, such as avoiding hazardous objects, were unnecessary.

In the block erection process, checking and identifying the risks for such interference and collisions is imperative. If any interference occurs during the erection process, it frequently leads to a situation where it is necessary to solve the problem with a loading object hooked onto a crane. Otherwise, the loading object must be moved again back to the original position. In addition, interference and collisions occurring in the block erection process may also lead to human accidents. Consequently, additional operations, including renewal operations, extend the time for the dock and affect the overall production schedule. In this way, accidents may cause quality deterioration and adversely affect the trust relationship with the ship owners due to problems, such as project delays.

The simulation in this study requires professional simulation engineers and expensive hardware and software. Nevertheless, as shipbuilding projects are generally carried out as a series of large-scale projects, the developed simulation is expected to contribute to acquiring up-to-date shipbuilding data and prevent process delays and serious industrial accidents.

Conflict of Interest

The authors declare no potential conflict of interest.

Funding

This paper was supported by Korea Institute for Advancement of Technology (KIAT) grant funded by the Korea Government (MOTIE) (P0017006, The Competency Development Program for Industry Specialist)

References


- 3D Systems. (n.d.). *Geomagic Design X*. <https://ko.3dsystems.com/software/geomagic-design-x>
- Bae, Y. C., Kim, C. S., Kim, Y. G., Cho, E. J., & Park, J. B. (2007). The development of industrial laser range finder. *The Journal of the Korea Institute of Electronic Communication Sciences*, 2(4), 228–235.
- Cha, J. H., Hu, Y. J., Kim, Y. J., Song, C. Y., & Lee, D. Y. (2012). Installation control simulation of fixed-type offshore wind turbine substructure. *Proceedings of 2012 Conference of the Korean Society for Marine Environment & Energy*, 418–425.
- Cha, J. H., Roh, M. I., & Lee, K. Y. (2009). Block erection simulation in shipbuilding using the open dynamics module and graphics module. *Korean Journal of Computational Design and Engineering*, 14(2), 69–76.
- Che, G. S. (2017). A study on the comparison and utilization of 3D point cloud data for building objects using laser scanning and photogrammetry [Master's Thesis, Sungkyunkwan University].
- Cheon, S., Lee, J. H., Park, K. P., & Suh, H. W. (2013). Requirement analysis on lightweight CAD models in ship PLM environment and its application examples. *Korean Journal of Computational Design and Engineering*, 18(4), 299–307. <https://doi.org/10.7315/CADCAM.2013.299>
- Dassault Systems. (n.d.). *Discover CATIA*. <https://www.3ds.com/products-services/catia/>
- Ham, S. H., No, M. I., & Lee, J. H. (2020). Integrated simulation method for the development of multi-purpose ship and ocean simulators. *Korean Journal of Computational Design and Engineering*, 25(2), 161–182. <https://doi.org/10.7315/CDE.2020.161>
- Heo, C. S., Kim, S. M., & Kwon, O. (2012). Simulation system practical application case. *Bulletin of the Society of Naval Architects of Korea*, 49(2), 66–81.
- Hwang, H. J. (2013). Shipbuilding and offshore production simulation technology. *Communications of the Korean Institute of Information Scientists and Engineers*, 31(1), 33–39.
- Hwang, H. J. (2014). Production simulation integrated solution for productivity improvement in the shipbuilding and maritime industry. *Journal of the Korean Society of Mechanical Engineers*, 54(12), 45–48.
- Hwang, I. H., Noh, J. K., Lee, K. K., & Shin, J. G. (2010). Short-term scheduling optimization for subassembly line in ship production using simulated annealing. *Journal of the Korea society for simulation*, 19(1), 73–82.
- Kang, Y. Y., Lee, G. H., Chun, S. W., Moon, D. H., & Hand, S. H. (2011). Analysis of ship design catalog construction status to simplify equipment 3D CAD. *Korean Society of Shipbuilding Academic Conference Materials*, 112–114
- Ki, J. S., Hwang, K. C., & Choi, J. H. (2020). A study on the development of high sensitivity collision simulation with digital twin. *Journal of the Society of Disaster Information*, 16(4), 813–823. <https://doi.org/10.15683/kosdi.2020.12.31.813>
- Kim, D. J. (2013). 빅데이터의 80%는 위치와 관련 있는 공간빅데이터이다? [80% of big data is geospatial big data related to Location?]. *News letter of Spatial Information Research Institute*,

17. 1. https://www.lx.or.kr/cmm/fms/FileDown.do?atchFileId=FILE_00000000010252snmNw&fileSn=0
- Kim, G. Y., Lee, I. S., Song, M. H., & Noh, S. D. (2007). PPR information managements for manufacturing of automotive press dies. *Korean Journal of Computational Design and Engineering*, 12(6), 452-460.
- Kim, M. S., Song, W., Choi, Y. J., & Hong, M. (2018). Real-Time collision response between cloth and sphere object in Unity. *Journal of Internet Computing and Services*, 19(6), 53-62. <https://doi.org/10.7472/jksii.2018.19.6.53>
- Kwon, S. W. (2009). Object recognition and modeling technology using laser scanning and BIM for construction industry. *Review of Architecture and Building Science*, 53(4), 31-38.
- Lee, J. C., Noh, T. H., & Kim, J. S. (2007). Coastal topography extraction using terrestrial laser scanning technique. *Proceedings of Korean Society for Geospatial Information Science*, 380-384.
- Lee, J. S. (2018). 3D Modeling Product Design Process Based on Photo Scanning Technology. *Journal of the Korea Institute of Information & Communication Engineering*, 22(11), 1505-1510. <https://doi.org/10.6109/jkiice.2018.22.11.1505>
- Lee, K. Y., Gu, N. G., & Roh, M. I. (2011). Crane lifting and loading simulation of blocks. *Bulletin of the Society of Naval Architects of Korea*, 48(4), 14-18.
- Lee, P. R., & Hwang, I. H. (2011). Shipbuilding and offshore process mutual verification simulation and production management platform. *Bulletin of the Society of Naval Architects of Korea*, 48(4), 10-13.
- Lee, S. H. (2017, July 24). 24억달러 선박펀드, 군산조선소에 '핀셋 지원' 논란 [Gunsan shipyard's \$2.4 billion ship fund 'Tweezers' support controversy]. *E News Today*. <http://www.ewestoday.co.kr/news/articleView.html?idxno=1090038>
- Lee, S. I. (2021). 레이저스캐닝 기술개요 및 건축 리모델링 현장 시범 적용 사례 [Laser scanning technology overview and architectural remodeling site case study]. *Construction Technology Review Ssangyoung*, 78, 93-98.
- Lee, U. S. (2022). 150-ton Crawler Crane Work Plan Simulator using Unity. *Proceedings of 2022 Autumn Conference on Drive and Control*, The Korea Fluid Power Systems Society, 74-78.
- Leica Geosystems. (n.d.) *Leica cyclone REGISTER 360 PLUS - 3D laser scanning point cloud registration software*. <https://leica-geosystems.com/en-in/products/laser-scanners/software/leica-cyclone/leica-cyclone-register-360>
- Ministry of Employment and Labor (MOEL). (2018). *Public participation investigation committee investigation report on severe industrial accidents in the shipbuilding industry*. https://www.moel.go.kr/policy/policydata/view.do?bbs_seq=20180900181
- Ministry of Employment and Labor (MOEL). (2022). *Industrial Accident Status Analysis in 2021*. https://www.moel.go.kr/policy/policydata/view.do?bbs_seq=20221201394
- Mline Studio. (2023). *Serious disaster in the shipbuilding industry, 'Crane Accident'*. https://m-line.tv/vr-content/safeline_005/
- Mokpo National Maritime University (MMU). (n.d.) *Training ship*. <https://www.mmu.ac.kr/main/contents/tsIntro>
- NVIDIA. (n.d.). *NVIDIA PhysX system software*. <https://www.nvidia.com/ko-kr/drivers/physx/physx-9-19-0218-driver/>
- Park, J. G., & Lee, G. H. (2022). Individual tree detection and modeling using terrestrial and drone-mounted laser scanners. *Journal of the Korea Academia-Industrial cooperation Society*, 23(11), 36-41. <https://doi.org/10.5762/KAIS.2022.23.11.36>
- Pfrommer, J., Schleipen, M., & Beyerer, J. (2013). PPRS: production skills and yheir relation to product, process, and resource. In *2013 IEEE 18th Conference on Emerging Technologies & Factory Automation (ETFA)* (pp. 1-4). IEEE. <https://doi.org/10.1109/ETFA.2013.6648114>
- Sin, S. H. (2022, January 27). *Mokpo Maritime University training ship SEGEROHO 'Non-contact visiting day' program operated*. Veritas-a. <http://www.veritas-a.com/news/articleView.html?idxno=405222>
- THHI. (n.d.). *45T30M Port jib crane*. <http://ko.tonghui-crane.com/port-crane/rack-luffing-crane/45t30m-port-jib-crane.html>
- Unity. (n.d.). *Unity introduction*. <https://unity.com/kr/our-company>

Author ORCIDs

Author name	ORCID
Kim, Yeon-Jun	0009-0004-8013-9973
Wang, SeungYeol	0009-0003-6337-9185
Jang, Jaewon	0000-0003-3971-2550
Park, Bon-Yeong	0000-0003-2452-0310
Lee, Dong-Kun	0000-0002-8705-062X
Oh, Daekyun	0000-0001-5239-1590

Numerical Method for Calculating Fourier Coefficients and Properties of Water Waves with Shear Current and Vorticity in Finite Depth

JangRyong Shin ¹

¹Engineer, Offshore structure design department, Hanwha Ocean Co., LTD, Geoje, Korea

KEYWORDS: Fourier approximation, Fenton's method, Newton's method, Shooting method, Incompressible Euler equations

ABSTRACT: Many numerical methods have been developed since 1961, but unresolved issues remain. This study developed a numerical method to address these issues and determine the coefficients and properties of rotational waves with a shear current in a finite water depth. The number of unknown constants was reduced significantly by introducing a wavelength-independent coordinate system. The reference depth was calculated independently using the shooting method. Therefore, there was no need for partial derivatives with respect to the wavelength and the reference depth, which simplified the numerical formulation. This method had less than half of the unknown constants of the other method because Newton's method only determines the coefficients. The breaking limit was calculated for verification, and the result agreed with the Miche formula. The water particle velocities were calculated, and the results were consistent with the experimental data. Dispersion relations were calculated, and the results are consistent with other numerical findings. The convergence of this method was examined. Although the required series order was reduced significantly, the total error was smaller, with a faster convergence speed.

1. Introduction

Since Chappellear (1961) developed an early numerical method, many other numerical methods have been derived (Dean, 1965; Rienecker and Fenton, 1981; Chaplin, 1979; Cokelet, 1977; Fenton, 1988). Rienecker and Fenton (1981) solved the coefficients and some wave properties directly using Newton's method. This method was further simplified by Fenton (1988). The major modification was that all the required partial differentials were calculated numerically (Tao et al., 2007). Although neither of the above numerical methods could be applied to waves in deep water (Fenton, 1990), Shin (2023) calculated deep water breaking waves with an error of less than 2.04×10^{-3} percent, demonstrating that Fourier approximation is effective even for deep water waves. The objective of this study was to extend Shin's method (Shin, 2023) to include rotational water waves with a shear current in a finite depth (Shin, 2022). The basic concept of Shin's method (Shin, 2023) for establishing a set of equations was similar to Fenton's method (Rienecker and Fenton, 1981; Fenton, 1988), and some issues with Fenton's method have been addressed. The first issue is inherent in Newton's method, which necessitates an initial solution in close proximity to the final solution. In common with other versions of the Fourier approximation method (Chappellear, 1961; Dean, 1965; Chaplin, 1979), it is sometimes necessary to solve a

sequence of lower waves, extrapolating forward in height steps until the desired height is reached (Fenton, 1988). These methods can occasionally converge to the wrong solution with very long waves (Fenton, 1988). This paper shows that regression analysis can easily avoid this issue (Shin, 2019).

The second issue arises from the coordinate system. Because Fenton's method adopts the moving coordinate system proposed by Dean (1965), the abscissa is the position from the crest in the range, $-L \leq x \leq L$. Therefore, the relative position with respect to the wavelength, L , is unknown because the wavelength is unknown. As a result, the number of unknown variables to be determined in Fenton's method is more than double the number in this study. Furthermore, a nonlinear equation for calculating the wavelength was coupled to the set of equations for calculating the coefficients. This coupling complicates the problem because Newton's method requires partial derivatives with respect to the wavelength. The issue can be avoided easily using the dimensionless coordinate system in Fig. 1 because it is independent of the wavelength. The abscissa is the phase in the range $-\pi \leq \beta \leq \pi$, and is known. After determining the steepness, S , the wave-number is calculated as $k = S/H$ because wave height, H is known. The steepness is calculated using the wave height condition, which is integrated automatically into the set of equations because it is linear. Therefore, it is not necessary to calculate the partial derivatives with regard to the wavelength in this study.

Received 13 October 2023, revised 1 December 2023, accepted 8 December 2023

Corresponding author JangRyong Shin: +82-55-735-5117, jrshin9797@hanwha.com

© 2023, The Korean Society of Ocean Engineers

This is an open-access article distributed under the terms of the creative commons attribution non-commercial license (<http://creativecommons.org/licenses/by-nc/4.0>) which permits unrestricted non-commercial use, distribution, and reproduction in any medium, provided the original work is properly cited.

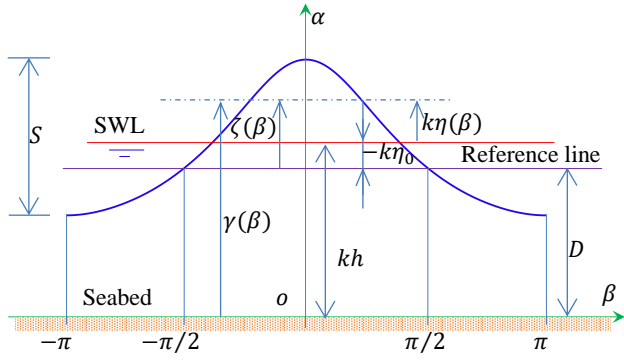


Fig. 1 Typical wave profile in the coordinate system

The third issue arises from the water depth condition used to calculate the reference depth, D , which is unknown. Fenton's method requires partial derivatives with respect to the reference depth because the water depth condition is coupled to the set of nonlinear equations used to calculate the coefficients. Most errors in Fenton's method occur when the water depth condition is calculated numerically. The required series order must be increased to reduce the error, and Simpson's rule was used for the numerical integration. This issue was avoided by calculating the reference depth independently using the shooting method in the study. In numerical analysis, the shooting method is used to solve a boundary value problem by transforming it into an initial value problem. A set of " n " equations with " n " unknowns can be converted to a set of " $n-1$ " equations with " $n-1$ " unknowns because one variable can be calculated independently, assuming it is a known value in advance. The assumed value was determined using the shooting method. Although it has the disadvantage of requiring the calculation of one procedure as two procedures, the numerical formulation simplifies the process and significantly reduces the total number of steps needed to converge to a complete solution. The reference depth is not coupled to the set of equations for calculating the Fourier coefficients because the water depth condition is calculated independently.

The fourth issue is a method for calculating the partial derivatives required in Newton's method. While all the necessary partial derivatives were obtained numerically in Fenton (1988), they were calculated analytically by tensor analysis in the present study. Therefore, there are no errors in the partial derivatives in this study.

Although the above-mentioned studies are irrotational flows, this study is rotational flow based on Shin (2022). The numerical method used to calculate the Fourier coefficients and the related wave properties was not presented by Shin (2022) but is presented in the present study. Shin (2018) presented the numerical method for irrotational waves. The method was extended to rotational waves in this study. Shin (2022) reported the complete solutions to the Euler equations and calculated the waves by Le Mehaute et al. (1968). The fluid velocities calculated by irrotational wave theories (Fenton, 1990; Tao et al., 2007) and by rotational wave theory (Shin, 2022) were compared with the experimental data reported by Le Mehaute et al. (1968) on the same graphs. Unlike the irrotational waves, the results of the rotational wave theory agreed well with the experimental data. The calculated wave-breaking limit was in good accordance with the Miche formula. While Rienecker and Fenton (1981), Fenton (1988), Tao et al. (2007), Cokelet (1977), and Vadden-Broeck and Schwartz (1979) calculated the dispersion relations for some waves in a relative depth of 0.7, this study calculated these relations for many waves with

different heights at various depths. The results were then extrapolated to all waves using regression analysis (Shin, 2019). The dispersion relations for a relative depth of 0.7 were compared and showed good accordance with the other results. The convergence of this study was tested according to the series orders. Even for relatively small orders, the error was significantly lower than Fenton's method and Tao et al. (2007).

2. The Complete Solution to the Euler Equations

This chapter summarizes the solution reported by Shin (2022). The two coordinate systems were adopted. The first was a conventional coordinate system (t, x, y) , as reported by Dean et al. (1984), in which the origin is located at a fixed point on the still water line (SWL). The x -axis is in the direction of wave propagation; the y -axis points vertically upward, and t is the time. The fluid domain is bounded by a flat bed, $y = -h$ (water depth), and by a free surface $y = \eta(t, x)$. The second is a dimensionless coordinate system, (β, α) , as shown in Fig. 1, which is a stationary frame. The origin is located under the crest of the bed. Therefore, the wave profile is fixed with a periodic, even function in the system. The abscissa is phase $\beta = kx - \omega t$ in $-\pi \leq \beta \leq \pi$, where $k = 2\pi/L$ is the wave number and $\omega = 2\pi/T$ is the angular frequency. Here, T is the wave period; L is the wavelength, and the ordinate is the dimensionless elevation from the bed, $\alpha = k(y + h)$ in $0 \leq \alpha \leq \gamma$, where $\gamma = k(\eta + h)$ is the dimensionless free surface elevation from the bed. The term $\zeta = \gamma - D$ is a dimensionless free surface elevation measured from the reference line (the horizontal line passing through two points on the free surface at two phases $\beta = \pm\pi/2$). The reference depth $D = k(\eta_o + h)$ is the dimensionless distance from the bed to the reference line where $\eta_o = \eta(\pm\pi/2)$. Because the coordinate system is independent of the wavelength, it has several advantages, as presented by Shin (2023). The dimensionless quantity of a flow field f is denoted by \bar{f} except for those defined separately, such as S and θ . Using the notation, the stream function is defined by $\psi = \bar{\psi} \omega / k^2$. The horizontal and vertical velocities are defined by $u = C\bar{u}$ and $v = C\bar{v}$, respectively, where $C = \omega/k$ is the celerity. The vorticity is defined by $\Omega = \omega\bar{\Omega}$. The pressure is defined by $p = \rho C^2 \bar{p}$, where ρ is the water density. The dimensionless wave height (steepness) is defined by $S = kH$. The linear steepness $\theta = \omega^2 H / g$ (where g is the gravity) is a constant for a particular wave. When $h \rightarrow \infty$ and $H \rightarrow 0$, $S \rightarrow \theta$, which gives the dispersion relation ($\omega^2 = gk$) of deep water linear waves. The stream function to satisfy the incompressible Euler equations is as follows:

$$\bar{\psi} = \alpha - \frac{c_0 \sinh\langle 0 \rangle \alpha}{\langle 0 \rangle} + \sum_{n=1}^N c_n \frac{\sinh\langle n \rangle \alpha}{\cosh\langle n \rangle D} \cos n\beta \quad (1)$$

where $\langle n \rangle \stackrel{\text{def}}{=} \sqrt{n^2 + \varepsilon}$; N is the series order; and c_n are the Fourier coefficients. The first and second terms describe a current. On the other hand, the two terms can be deleted for an irrotational wave ($\varepsilon = 0$). The vorticity is presented as follows:

$$\bar{\Omega} = \varepsilon \left\{ \frac{c_0 \sinh\langle 0 \rangle \alpha}{\langle 0 \rangle} - \sum_{n=1}^N c_n \frac{\sinh\langle n \rangle \alpha}{\cosh\langle n \rangle D} \cos n\beta \right\} \quad (2)$$

This solution also contains irrotational waves, where the constant, ε is referred to as the strength of vorticity because $\bar{\Omega} = 0$ when $\varepsilon = 0$. When ε is non-positive, the vorticity has the same direction as the motion of the particles. The iso-stream and iso-vorticity lines can be calculated using Newton's method in the Appendix. The free surface is an iso-vorticity line given by $\bar{\Omega}(\beta, \gamma) = C_1 \varepsilon$, where C_1 is a constant. Substituting $\bar{\Omega}(\beta, \gamma) = C_1 \varepsilon$ into Eq. (2), the wave profile is determined to satisfy the KFSBC (Kinematic free surface boundary condition) as follows:

$$\frac{c_0(\sinh\langle 0 \rangle \gamma - \sinh\langle 0 \rangle D)}{\langle 0 \rangle} = \sum_{n=1}^N c_n \left\{ \frac{\sinh\langle n \rangle \gamma}{\cosh\langle n \rangle D} \cos n\beta - \tanh\langle n \rangle D \cos \frac{n\pi}{2} \right\} \quad (3)$$

The constant C_1 is determined from the definition of the reference line in Fig. 1; that is, $\gamma(\pm\pi/2) = D$. The profile is an implicit function that can be calculated using Newton's method in the Appendix. When $\varepsilon \rightarrow 0$, Eq. (3) yields the profile defined by Shin (2018). Moreover, the sea bed is an iso-vorticity line given by $\bar{\Omega}(\beta, 0) = 0$. Differentiating Eq. (1) with respect to α and β , the horizontal velocity becomes the following.

$$\bar{u} = 1 - c_0 \cosh\langle 0 \rangle \alpha + \sum_{n=1}^N \langle n \rangle c_n \frac{\cosh\langle n \rangle \alpha}{\cosh\langle n \rangle D} \cos n\beta \quad (4)$$

The vertical velocity is as follows:

$$\bar{v} = \sum_{n=1}^N n c_n \frac{\sinh\langle n \rangle \alpha}{\cosh\langle n \rangle D} \sin n\beta \quad (5)$$

Substituting Eqs. (1)–(5) to the Euler momentum equations, Bernoulli's principle for rotational flow can be calculated as follows.

$$\frac{\bar{U}^2}{2} + \frac{S\alpha}{\theta} + \bar{p} = Q \quad (6)$$

where $\bar{U}^2 = \bar{V}^2 - \varepsilon(\alpha - \bar{\psi})^2$, and Q is a constant. A mechanical analog to irrotational and rotational flows was depicted by considering a carnival Ferris wheel in Fig. 2.11 in Dean et al. (1984). While the irrotational motion of chairs involves rotating around the center of the Ferris wheel, the rotational motion of the chairs involves both revolving around the center of the Ferris wheel and rotating around their center. Therefore, the total kinetic energy of the rotational motion is represented by the sum of the revolving kinetic energy around the center of the Ferris wheel and the rotating kinetic energy around their center. Analogous to the Ferris wheel, the total kinetic energy of rotational flow is represented by $\bar{U}^2 = \bar{V}^2 - \varepsilon(\alpha - \bar{\psi})^2$, where the first term corresponds to the revolving kinetic energy around the center of the Ferris wheel, and the second term corresponds to the rotating kinetic energy around its center. When $\varepsilon = 0$, $\bar{U}^2 = \bar{V}^2 = (1 - \bar{u})^2 + \bar{v}^2$, which is the kinetic energy for irrotational flow. In contrast to Baddour et al. (1998), ε is not positive because kinetic energy functions should be positive-definite functions. Therefore, let $\varepsilon \stackrel{\text{def}}{=} -\sigma^2$, where σ is a non-negative real number. Hence, $\langle 0 \rangle = \sigma i$. Substituting Eqs. (1), (4), and (5) into the relation, $\bar{U}^2 = \bar{V}^2 -$

$\varepsilon(\alpha - \bar{\psi})^2$, the dynamic pressure (kinetic energy) \bar{U}^2 is as follows:

$$\bar{U}^2 = c_0^2 - 2 \sum_{n=1}^N \Lambda_{0n} c_n + \sum_{n=1}^N c_n \left\{ \sum_{m=1}^N \Lambda_{nm} c_m \right\} \quad (7)$$

where

$$\Lambda_{0n}(\beta, \alpha) \stackrel{\text{def}}{=} \frac{c_0 \cos n\beta}{\cosh\langle n \rangle D} \{ \langle n \rangle \cosh\langle 0 \rangle \alpha \cosh\langle n \rangle \alpha - \langle 0 \rangle \sinh\langle 0 \rangle \alpha \sinh\langle n \rangle \alpha \} \quad (8)$$

and

$$\begin{aligned} \Lambda_{nm}(\beta, \alpha) \stackrel{\text{def}}{=} & Z_1 \cosh(\langle n \rangle + \langle m \rangle) \alpha \cos(n - m) \beta \\ & + Z_2 \cosh(\langle n \rangle - \langle m \rangle) \alpha \cos(n - m) \beta \\ & + Z_3 \cosh(\langle n \rangle + \langle m \rangle) \alpha \cos(n + m) \beta \\ & + Z_4 \cosh(\langle n \rangle - \langle m \rangle) \alpha \cos(n + m) \beta \end{aligned} \quad (9)$$

where $Z_1 = (\langle n \rangle \langle m \rangle + nm - \varepsilon)/4W$; $Z_2 = (\langle n \rangle \langle m \rangle - nm + \varepsilon)/4W$; $Z_3 = (\langle n \rangle \langle m \rangle - nm - \varepsilon)/4W$; $Z_4 = \frac{\langle n \rangle \langle m \rangle + nm + \varepsilon}{4W}$; and $W = \cosh\langle n \rangle D \cosh\langle m \rangle D$. If Λ_{0n} is the component of column vector $\{\Lambda_{0n}\}$ and c_n is the component of the column vector $\{c_n\}$, the second term on the right side in Eq. (7) becomes an inner product of the two vectors. Accordingly, Λ_{nm} can be considered a component of the square matrix $[\Lambda_{nm}]$ in N -dimensional space. Therefore, the third term on the right side of Eq. (7) is presented as $\{c_n\}^t [\Lambda_{nm}] \{c_m\}$, where $\{c_n\}^t$ is a row vector. This concept helps formulate numerical calculations in this study. Considering the average speed \bar{U}_b over a wave period on the sea bed, the constant c_0 is determined as follows:

$$c_0 = 1 - \bar{U}_b \quad (10)$$

For the average speed \bar{U}_s over a wave period on still water, the strength of vorticity is as follows:

$$\sigma = \frac{1}{kh} \cos^{-1} \left(\frac{1 - \bar{U}_s}{1 - \bar{U}_b} \right) \quad \text{for} \quad \left| \frac{1 - \bar{U}_s}{1 - \bar{U}_b} \right| \leq 1 \quad (11)$$

From Stokes' breaking criterion, $|\bar{U}_b| \leq 1$ and $|\bar{U}_s| \leq 1$. The Bernoulli's constant Q is determined from the definition of the reference line (i.e., $\gamma(\pi/2) = D$) and the DFSBC (Dynamic free surface boundary condition), i.e., $\bar{p}(\pi/2, D) = 0$ because the point $(\pi/2, D)$ is on the free surface. Therefore, the pressure field is

$$\bar{p} = -\frac{1}{2} \left\{ \bar{U}^2(\beta, \alpha) - \bar{U}^2\left(\frac{\pi}{2}, D\right) \right\} - \frac{S(\alpha - D)}{\theta} \quad (12)$$

By applying the DFSBC, i.e., $\bar{p}(\beta, \gamma) = 0$ on $\alpha = \gamma$ to Eq. (12), the other wave profile can be determined as follows:

$$\frac{S\zeta}{\theta} = -\frac{1}{2} \left\{ \bar{U}^2(\beta, \gamma) - \bar{U}^2\left(\frac{\pi}{2}, D\right) \right\} \quad (13)$$

The wave height condition is defined as

$$S = \zeta(0) - \zeta(\pi). \quad (14)$$

The water depth condition is defined as

$$kh = \frac{1}{2\pi} \int_{-\pi}^{\pi} \gamma d\beta \quad (15)$$

3. Newton's Method for Coefficients and Steepness

The solution contains $N+2$ unknown constants: N Fourier coefficients, c_n , steepness, S , and reference depth, D . Eqs. (3) and (13) present two wave profiles with implicit functions. The two wave profiles are even functions considering the coordinate system. The Fourier series of a periodic even function is presented as $f(x) = \sum_{n=0}^{\infty} c_n \cos nx$, in $-\pi \leq x \leq \pi$. The coefficients are generally determined from the orthogonality of trigonometric functions. The method is inapplicable when $f(x)$ is an implicit function, as expressed in Eqs. (3) and (13). The problem can be solved by converting the series to a set of algebraic equations, which are obtained by calculating the series at some phases instead of all phases. This is done by replacing the infinite series with a truncated series, i.e., $\sum_{n=0}^N c_n \cos nx_m = f(x_m)$ for $m = 1, \dots, N$. There are N algebraic equations for calculating the coefficients, c_n , because $\cos nx_m$ and $f(x_m)$ are known. Hence, there are a set of N equations, and Eqs. (3) and (13) are equal to each other at $N+1$ phases (Note that Eqs. (3) and (13) are already equal to each other at phase $\pm\pi/2$ because the integral constants were determined to satisfy the definition of the reference line) and two equations, i.e., Eqs. (14) and (15). Therefore, there are $N+2$ equations to determine the unknown constants.

Referring to Eqs (3)–(5), the denominators are expressed as transcendental functions of the reference depth. When determining the reference depth using Newton's method in conjunction with the coefficients, it is necessary to calculate the partial derivative with respect to the reference depth. Furthermore, Eq. (15) only permits a numerical approach. This difficulty can be overcome by calculating the reference depth independently using the shooting method, assuming that the reference depth is known. Based on the assumption, Eq. (15) is independent of the other equations and will be calculated in the next chapter. In addition to this assumption, N parameters, X_m , are introduced in this chapter to simplify the numerical formulation. Unlike Fenton's method, X_m are merely parameters for calculating the coefficients and the steepness in this chapter. After determining the coefficients, X_m are no longer used. Hence, the wave elevation is denoted with X_m instead of ζ_m in this chapter.

When the wave profile ζ and the reference depth D are prescribed, it is possible to convert Eq. (3) into a set of linear equations for the coefficients. Because the wave profile is an even function, the phases $\beta_m (m = 1, 2, \dots, N)$ are considered in the range $0 \leq \beta_m \leq \pi$ and $\beta_m \neq \pi/2$ because the two wave profiles are already equal at phase $\beta = \pi/2$. In addition, $\beta_1 = 0$ and $\beta_N = \pi$. Denoting $\zeta(\beta_m)$ as X_m , i.e., $X_m = \zeta(\beta_m)$, Eq. (3) is presented.

$$K_{mn}c_n = Y_m \quad (16)$$

The summation convention is considered in Eq. (16). The repeated subscript “ n ” is a dummy subscript, whereas K_{mn} is a second-order

tensor, and the terms c_n and X_m are vectors in N -dimensional space. From Eq. (3), the component of the tensor K_{mn} is presented as

$$K_{mn} = \frac{\sinh\langle n \rangle \bar{X}_m}{\cosh\langle n \rangle D} \cos n\beta_m - \tanh\langle n \rangle D \cos \frac{n\pi}{2} \quad (17)$$

where $\bar{X}_m = X_m + D$. Because $\langle 0 \rangle = \sigma i$, the component of the first-order tensor, Y_m is presented as

$$Y_m = \frac{c_0 \{ \sin \sigma \bar{X}_m - \sin \sigma D \}}{\sigma} \quad (18)$$

The summation convention is not applied when the component of a tensor is presented as in Eqs. (17) and (18). Using the inverse tensor G_{mn} of the tensor K_{mn} , the solution to Eq. (16) is determined easily as follows.

$$c_n = G_{nm}Y_m \quad (19)$$

Eq. (13) is also evaluated at the same phase. A set of N nonlinear equations for calculating the N parameters X_n is obtained by substituting Eq. (19) into Eq. (13) at the same phase because the wave height condition in Eq. (14) is expressed as $S = X_1 - X_N$ in this approach. For Newton's method, the error vector E_m is defined from Eq. (13) as follows:

$$E_p \stackrel{\text{def}}{=} -\frac{SX_p}{\theta} + A_{pn}c_n - \frac{1}{2}B_{pnm}c_n c_m \quad (20)$$

From Eqs. (8) and (9), the second-order tensor A_{pn} and the third-order tensor B_{pnm} are defined as

$$A_{pn} \stackrel{\text{def}}{=} \Lambda_{0n}(\beta_p, \bar{X}_p) - \Lambda_{0n}\left(\frac{\pi}{2}, D\right) \quad (21)$$

$$B_{pnm} \stackrel{\text{def}}{=} \Lambda_{nm}(\beta_p, \bar{X}_p) - \Lambda_{nm}\left(\frac{\pi}{2}, D\right) \quad (22)$$

Substituting Eq. (19) into Eq. (20), $E_p = 0$ gives a set of nonlinear equations for calculating the parameters, X_q . Therefore, unlike Fenton's method (Rienecker and Fenton, 1981; Fenton, 1988), the set of N nonlinear equations is solved using Newton's method in this study. Therefore, when using the same series order, the number of unknown constants is less than half of that in Fenton's method.

Denoting partial derivatives of a tensor by making use of commas and indices as $\frac{\partial(\quad)}{\partial X_q} = (\quad)_{,q}$ and expanding Eq. (20) as a Taylor series about X_q points in terms of ΔX_q and ignoring higher-order terms, the following set of linear equations is obtained:

$$E_{p,q} \Delta X_q = -E_p \quad (23)$$

Because $\Delta X_q^{(r)} = X_q^{(r+1)} - X_q^{(r)}$, the solution in the next step is

$$X_q^{(r+1)} = X_q^{(r)} + \Delta X_q^{(r)} \quad (24)$$

The superscript (r) means the step of Newton's method. It is clear that all the steps are r^{th} in all equations except Eq. (24). Thus, for the

simplification of equations, the superscript (r) was omitted in all the equations except Eq. (24). Differentiating Eq. (20) with respect to X_q , the partial derivative $E_{p,q}$ of the error vector is

$$E_{p,q} = -\frac{S_{,q}X_p}{\theta} - \frac{S\delta_{pq}}{\theta} + A_{pn,q}c_n + A_{pn}c_{n,q} - \frac{1}{2}B_{pnm,q}c_n c_m - B_{pnm}c_{n,q}c_m. \quad (25)$$

Note that $c_{n,q}c_m = c_n c_{m,q}$. Because $S = X_1 - X_N$,

$$S_{,q} = \begin{cases} 1 & \text{for } q = 1 \\ 0 & \text{for } q \neq 1 \text{ or } N \\ -1 & \text{for } q = N \end{cases}. \quad (26)$$

Differentiating Eq. (16) with respect to X_p results in

$$K_{mn,p}c_n + K_{mn}c_{n,p} = Y_{m,p}. \quad (27)$$

Multiplying Eq. (27) by the tensor G_{im} , the partial derivative of the coefficient is determined as follows.

$$c_{i,p} = G_{im}(Y_{m,p} - K_{mn,p}c_n). \quad (28)$$

where $G_{im}K_{mn} = \delta_{in}$ and $\delta_{in}c_{n,p} = c_{i,p}$ and δ_{in} is the second-order isotropic tensor. Differentiating Eq. (17) with respect to X_p , the components of the third-order tensor $K_{mn,p}$ are presented as

$$K_{mn,p} = \delta_{mp} \frac{\langle n \rangle \cosh \langle n \rangle \bar{X}_m}{\cosh \langle n \rangle D} \cos n\beta_m \quad (29)$$

Differentiating Eq. (18) with respect to X_p , the component of the second-order tensor $Y_{m,p}$ is presented as

$$Y_{m,p} = \delta_{mp} c_0 \cos \sigma \bar{X}_m. \quad (30)$$

Differentiating Eq. (21) with respect to X_q , the component of the third-order tensor $A_{pn,q}$ is expressed as follows:

$$A_{pn,q} = \frac{\delta_{pq} n^2 \sinh \langle n \rangle \bar{X}_p \cos \sigma \bar{X}_p \cos n\beta_p}{\cosh \langle n \rangle D} \quad (31)$$

Differentiating Eq. (22) with respect to X_q , the component of the forth-order tensor $B_{pnm,q}$ is

$$B_{pnm,q} = \delta_{pq} [Z_1^* \sinh(\langle n \rangle + \langle m \rangle) \bar{X}_p \cos(n-m)\beta_p + Z_2^* \sinh(\langle n \rangle - \langle m \rangle) \bar{X}_p \cos(n-m)\beta_p + Z_3^* \sinh(\langle n \rangle + \langle m \rangle) \bar{X}_p \cos(n+m)\beta_p + Z_4^* \sinh(\langle n \rangle - \langle m \rangle) \bar{X}_p \cos(n+m)\beta_p]. \quad (32)$$

where $Z_1^* = Z_1(\langle n \rangle + \langle m \rangle)$; $Z_2^* = Z_2(\langle n \rangle - \langle m \rangle)$; $Z_3^* = Z_3(\langle n \rangle + \langle m \rangle)$; and $Z_4^* = Z_4(\langle n \rangle - \langle m \rangle)$.

Based on the assumption that the reference depth is known, Eq. (16) is linear and decoupled from Eq. (20), unlike in Fenton's method (Rienecker and Fenton, 1981; Fenton, 1988). Dividing the inner

product of the error vector, E_m by N , the mean squared error (MSE) in the DFSBC is defined as

$$\text{MSE} = \sqrt{\frac{E_m E_m}{N}} \quad (33)$$

The MSE is used as a criterion for determining the convergence of the Newton method.

Shin (2019) was used as the first step, $X_m^{(0)}$ in Newton's method. The author reported that the real part of a geometric series, $f(\beta)$ with a common ratio, $\lambda e^{i\beta}$ (where "i" is the imaginary unit), closely resembles the shape of a water wave. A reliable approximation of the profile of a water wave can be achieved by shifting the function down by " $f(\pi/2)$ " to align with the reference line in Fig. 1, normalizing the result by its height and multiplying the result by the actual wave amplitude " $S/2$ " to meet the wave height condition, as reported by Shin (2019).

The profile satisfies the definition of the reference depth, i.e., $\zeta(\pm\pi/2) = 0$, the wave height condition in Eq. (14), and the water depth condition in Eq. (15). Replacing ζ with $X_m^{(0)}$, the profile at the phase β_m is presented as follows:

$$X_m^{(0)} = \frac{S^{(0)}}{2} \frac{1 - \lambda^2}{\lambda} \left(\frac{1 - \lambda \cos \beta_m}{1 + \lambda^2 - 2\lambda \cos \beta_m} - \frac{1}{1 + \lambda^2} \right) \quad (34)$$

where the steepness $S^{(0)}$ and the shape factor λ are presented in Shin (2019), and (0) means the first step in Newton's method. The function is much simpler than the other nonlinear waves because it contains only two parameters, i.e., wave steepness, S and the shape factor, λ . When the shape factor approaches 0, it becomes an Airy wave. When the shape factor approaches 0.5, it becomes a fifth-order Stokes wave. When the shape factor approaches 1, it becomes a Solitary wave. The shape factor is a positive real number less than 1. Because the function was derived independently from the Euler equations, the two parameters were determined to minimize the error in two boundary conditions on the free surface using a variational method. Because Eq. (34) is very close to the complete solution, Newton's method rapidly and converges for all waves.

4. Shooting Method for Reference Depth

In contrast to the assumption considered in Ch. 3, the reference depth is closely linked to the coefficients and is unknown. Therefore, while maintaining the validity of the method presented in Ch. 3, the shooting method is suitable for determining the reference depth. The reference depth is adjusted until the calculated water depth from the water depth condition matches the actual value using the shooting method. The secant method is used as a root-finding algorithm. In each step of the secant method, substituting the calculated coefficients and the prescribed reference depth into Eqs. (A1)–(A4), the wave elevations $\zeta_i^{(q)}$ are calculated with highly dense interval using Newton's method in the Appendix. The integral is numerically calculated by substituting the results into Eq. (15) as follows:

$$(k\eta_0)^{(q)} = -\frac{1}{2M} \sum_{i=1}^M (\zeta_i^{(q)} + \zeta_{i+1}^{(q)}) \quad (35)$$

where (q) stands for the q^{th} step of the secant method, and $\zeta_i = \zeta(\beta_i)$. ζ is an even function. Hence, $\beta_1 = 0$; $\beta_i = (i-1)\pi/M$; and $\beta_{M+1} = \pi$. In Fenton (1988), Eq. (35) must be calculated using only N data of X_i because Eq. (35) is coupled to the other equations. Therefore, $M = N$ in Fenton (1988). On the other hand, M is independent of N in this study. Eq. (35) can be calculated accurately compared to Fenton (1988) because M can be freely increased in this study. The water depth is calculated as follows:

$$h^{(q)} = \frac{1}{k} \{D^{(q)} - (k\eta_0)^{(q)}\} \quad (36)$$

The reference depth is calculated using the secant method as follows.

$$D = \lim_{q \rightarrow \infty} D^{(q+1)} \quad (37)$$

where

$$D^{(q+1)} = D^{(q-1)} + \frac{D^{(q)} - D^{(q-1)}}{h^{(q)} - h^{(q-1)}} \{h - h^{(q-1)}\} \quad (38)$$

where $D^{(0)}$ is determined using the regression result in Shin (2019), and h is the actual water depth. The actual value is in the vicinity of $D^{(0)}$. Hence, $D^{(1)}$ is selected with a value close to $D^{(0)}$, e.g., $D^{(1)} = 1.001D^{(0)}$. For each step, the error in the water depth is as follows:

$$\text{Error}^{(q)} = \frac{|h - h^{(q)}|}{h} \quad (39)$$

5. Calculation Procedure and Results

5.1 Calculation Procedure

Fig. 2 presents a flowchart. While there is only one do-loop in Fenton's method, the chart comprises three do-loops. The outer do-loop implements the secant method for calculating the reference depth, as described in Ch. 4. The first inner do-loop implements the Newton method for calculating the coefficients and steepness, as described in Ch. 3. The other inner do-loop implements Newton's method for calculating the wave profile, as described in the Appendix.

Initial approximations of the shape factor, steepness, and reference depth are first calculated by substituting the period, height, and depth into the regression analysis results presented by Shin (2019). The initial approximations of the wave profile are calculated using Eq. (34).

The first inner do-loop is performed. The coefficients, $c_n^{(r,q)}$, are calculated using Eq. (19), where "r" represents the step of the Newton method in Ch. 3 and "q" represents the step of the secant method in Ch. 4. Substituting $c_n^{(r,q)}$ and $D^{(q)}$ into Eqs. (20) and (25), $\Delta X_i^{(r,q)}$ are calculated using Eq. (23) and then $X_i^{(r+1,q)}$ are calculated using Eq. (24). The MSE is calculated with Eq. (33). If the MSE is greater than the tolerance, $X_i^{(r,q)}$ is replaced with $X_i^{(r+1,q)}$. The do-loop continues until Newton's method converges to the complete solution within the specified tolerance.

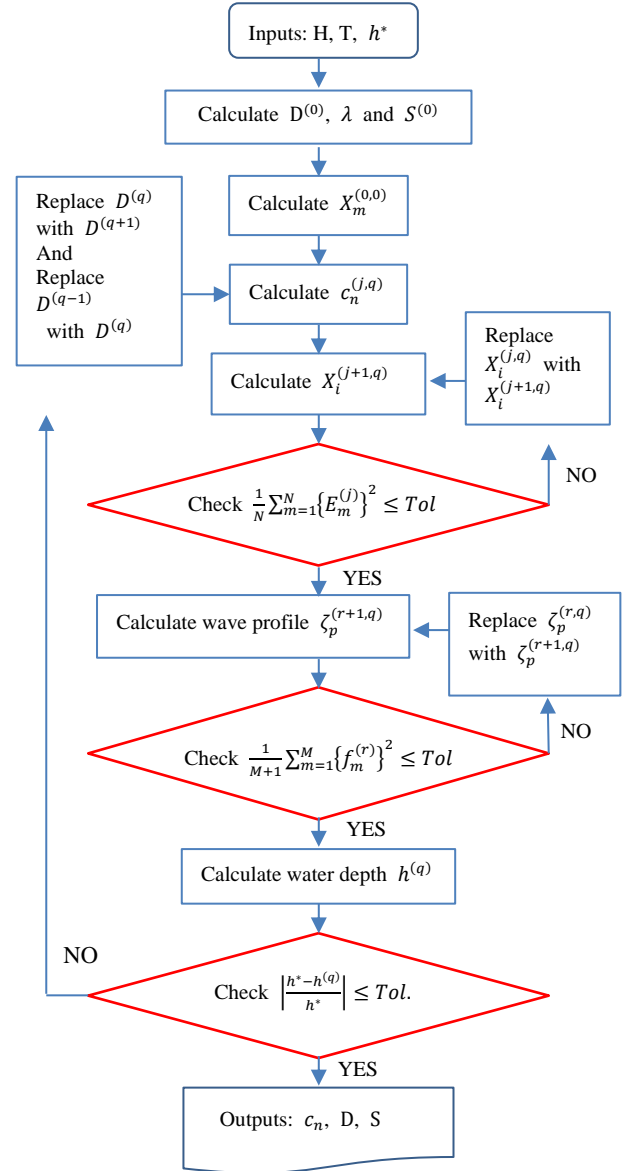


Fig. 2 Calculation procedure

The second inner do-loop is then performed to calculate the free surface elevations at more phases than those considered in the first inner do-loop. The elevations, $\zeta_i^{(r+1,q)}$, are calculated using Newton's method in the Appendix, where "r" represents the step of Newton's method.

By substituting $\zeta_i^{(q)} (: \lim_{r \rightarrow \infty} \zeta_i^{(r+1,q)})$ into Eq. (35), the water depth $h^{(q)}$ is calculated using Eq. (36). The reference depth $D^{(q+1)}$ is calculated using Eq. (38). Replacing $D^{(q)}$ with $D^{(q+1)}$, the outer do-loop should be repeated until the calculated depth converges to the actual depth. The first step solution of Newton's method in the $q+1$ step of the secant method, $X_m^{(0,q+1)}$ is determined using the converged value, $X_m^{(\infty,q)} \stackrel{\text{def}}{=} \lim_{r \rightarrow \infty} X_m^{(r,q)}$ in the q step of the secant method, i.e., $X_m^{(0,q+1)} = X_m^{(\infty,q)}$. Because $D^{(0)}$ is accurate, the secant method converges within three steps to the acceptable value whose error is less than 10^{-4} percent. The outputs are the coefficients, the reference depth, and the steepness.

5.2 Application Range of this Study

The coefficients and wave properties are functions of two variables: the reference depth and the linear steepness. The functions are presented with closed-form solutions in Shin (2019), which are the regression results determined using numerically calculated data for 2091 waves, as shown below. The domain of the functions is $\{(\theta, D) \mid 0 \leq \theta < 1 \text{ and } 0 < D\}$. A subset of the domain, $\{(\theta, D) \mid 0 \leq \theta < 1 \text{ and } 0 < D < 5\}$, was considered instead of the entire domain because waves are similar to deep water waves when $D > 5$. Seventeen cases of the reference depth were considered by dividing the domain by $D = 0.1, 0.15, 0.2, \dots, 1.0, 1.2, 1.5, 2, 3, 4, \text{ and } 5$. For each reference depth, the linear steepness was considered from 0 to 0.98 at 0.01 intervals, from 0.98 to 0.989 at 0.001 intervals, from 0.989 to 0.9899 at 0.0001 intervals, and from 0.9899 to 0.98997 at 0.00001 intervals, resulting in 123 cases of linear steepness. Therefore, $17 \times 123 = 2091$ irrotational waves were calculated with $N = 35$ and $M = 180$. The limits can be determined easily because the Newton method presented in the Appendix diverges at the crest when the steepness reaches its limit. These limits were represented by 17 red solid circle symbols in Fig. 3, which are calculated with $D = 0.1, 0.15, 0.2, \dots, 1.0, 1.2, 1.5, 2, 3, 4, \text{ and } 5$ in sequence from left to right. The solid curve is the regression analysis result determined using the 17 data. As shown in Fig. 3, the breaking limit is in good accordance with the Miche formula. Because the 2091 waves are dimensionless waves, they represent all waves below the breaking limit. Therefore, this study confirms stable convergence characteristics for all water waves.

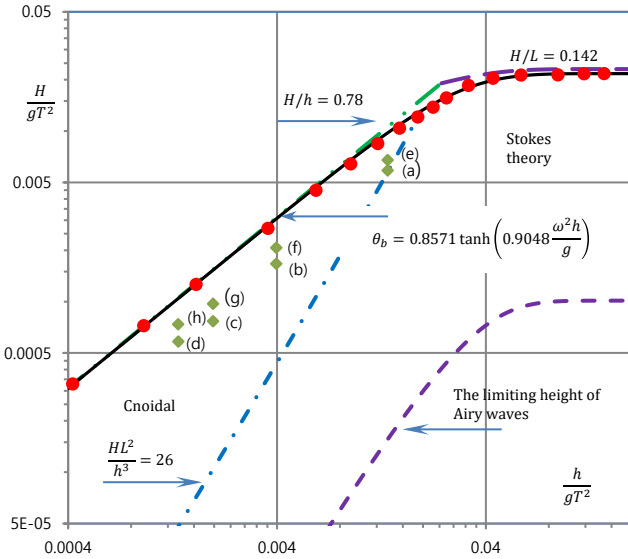


Fig. 3 Application range of this study cited from Shin (2019)

5.3 Water Particle Velocities Under the Crest

The eight waves considered in Le Méhauté et al. (1968) were calculated. Fig. 3 and Table 1 present the waves with solid diamond symbols. The results were compared with experimental data in Fig. 2 by Shin (2022). Fig. 4 shows the wave (h) during the eight waves. Referring to Fig. 2 of Shin (2022), the other waves give the same pattern, as shown in Fig. 4. The irrotational results were calculated with $\varepsilon = 0$. The regression analysis results were calculated by Shin (2019).

Rienecker and Fenton (1981) also calculated the waves, as shown in Fig. 2 of that work. The waves were also calculated by Fenton (1990), and the results are shown in Fig. 3(c) of that work. The cnoidal theory

Table 1 Eight waves considered in Le Méhauté et al. (1968)

Wave	(a)	(b)	(c)	(d)
H/h	0.434	0.420	0.389	0.433
$T\sqrt{g/h}$	8.590	15.870	22.490	27.240
Wave	(e)	(f)	(g)	(h)
H/h	0.499	0.522	0.493	0.548
$T\sqrt{g/h}$	8.590	15.870	22.502	27.270

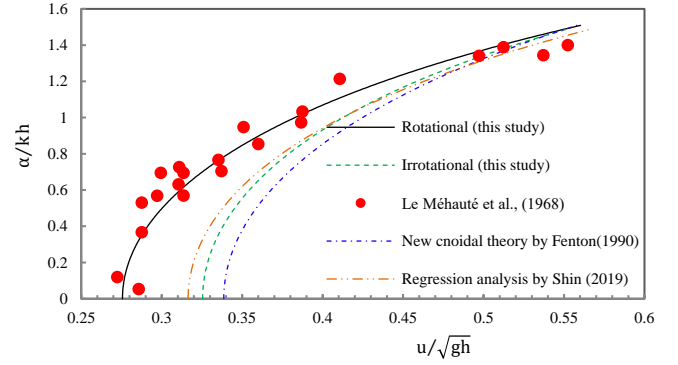


Fig. 4 Water particle velocities under the crest of the wave (h)

is the new cnoidal theory by Fenton (1990), which closely agrees with the Fourier approximation by Fenton (1988). Tao et al. (2001) also calculated the waves; the results are shown in Fig. 2 of that work. HAM (Homotopy analysis method) by Tao et al. (2001) results closely agree with the Fourier approximation reported by Rienecker et al. (1981). Therefore, the Fourier approximation and HAM results are not presented in Fig. 4. This study agrees with the experimental data, unlike those obtained using HAM or Fenton's method.

5.4 Dispersion Relation

Table 3 of Tao et al. (2007) provides a detailed comparison of the HAM solutions of waves in finite water depth and the results of Cokelet (1977) and Rienecker and Fenton (1981). The results are given in terms of the non-dimensional phase speed squared kC^2/g at various values of H/h , for a constant value of $\exp(-kR/C) = 0.5$ (R is the unit span denoting the total volume rate of flow underneath the steady wave per unit length in a direction normal to the x, z plane), corresponding to a wavelength to water depth ratio of $L/h \approx 9$ (Tao et al., 2007). Table 1 of Rienecker and Fenton (1981) presents the same comparison between the solutions of Rienecker and Fenton (1981) for $N = 16, 32, \text{ and } 64$, the results of Cokelet (1977), and the results of Vanden-Broeck & Schwartz.

The non-dimensional phase kC^2/g is presented with physical quantities defined in this study as follows:

$$\frac{kC^2}{g} = \frac{k}{g} \left(\frac{\omega}{k} \right)^2 = \frac{\omega^2}{gk} = \frac{\theta}{kH} = \frac{\theta}{S} \quad (40)$$

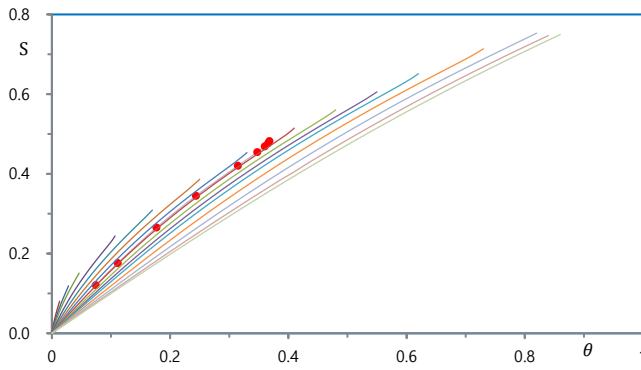
H/h is also presented with physical quantities defined in this study.

$$\frac{H}{h} = \frac{kH}{kh} = \frac{S}{kh} \quad (41)$$

$kh = 2\pi/9$ in Eq. (41) because $L/h \approx 9$. Therefore, the comparison shows the relationship between steepness, S , and linear

Table 2 Dispersion relation by Rienecker and Fenton (1981)

kc^2/g	H/h	θ	S
0.1729974	0.615059	0.074284	0.120775
0.2526308	0.631112	0.111309	0.176370
0.3802643	0.666501	0.176939	0.265475
0.4944549	0.706443	0.243860	0.345195
0.6024470	0.748230	0.314696	0.420587
0.6512510	0.764403	0.347543	0.454659
0.6721430	0.767760	0.360267	0.469244
0.6832000	0.767030	0.365845	0.476964
0.6908000	0.763000	0.367972	0.482269

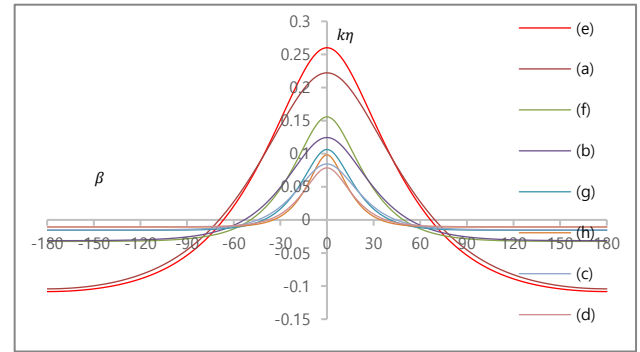
**Fig. 5** Dispersion relation for irrotational waves in the reference depths, $D = 0.1, 0.15, 0.2, \dots, 1.0, 1.2, 1.5, 2$, and ∞ in sequence from left to right

steepness, θ for the relative water depth, $kh = 2\pi/9$. Hence, the comparison shows the dispersion relation of waves in a finite water depth, $kh = 2\pi/9$. Table 2 lists the relation. The data in the first and second columns were cited from Rienecker and Fenton (1981), which are the results calculated using $N = 64$. The data in the fourth column was obtained by multiplying the data in the second column by $2\pi/9$, as stated in Eq. (41). The data in the third column was obtained by multiplying the data in the first column by the data in the fourth column, as stated in Eq. (40). Shin (2018, 2019) also calculated the relation for various water depths, $D = 0.1, 0.15, 0.2, \dots, 1.0, 1.2, 1.5, 2$, and ∞ . For a given reference depth, the linear steepness θ was considered with a highly dense interval from 0 to the application limit of this study. Fig. 5 presents the calculation results. The 15 curves are the results calculated with $D = 0.1, 0.15, 0.2, \dots, 1.0, 1.2, 1.5, 2$, and ∞ in sequence from left to right. The peaks of each curve represent the limit of wave breaking. The nine data in Table 2 are also presented with solid circles in Fig. 5, which agree with the curve for $D = 0.7$. The small difference results from the difference between $kh = 2\pi/9$ and $D = 0.7$. The relative depth for $D = 0.7$, is presented as $kh = D - k\eta_0 = 0.7 - k\eta_0 > 2\pi/9$, because $D = kh + k\eta_0$ and $k\eta_0$ is negative. Therefore, the $D = 0.7$ curve lies slightly to the right of the eight data because $k\eta_0$ is very small.

5.5 Error Check of this Study

The numerical method focuses on minimizing the errors in the DFSBC defined in Eq. (20) and the water depth conditions defined in Eq. (15). The convergence of this study according to the series order

was analyzed by calculating the eight waves considered in Le Méhauté et al. (1968) using $N = 8, 10, 16$, and 35 . Fig. 6 presents the calculated wave profiles for the waves. The abscissa represents the phase $\beta = kx - \omega t$ in $-180^\circ \leq \beta \leq 180^\circ$, while the ordinate represents the dimensionless elevation, $k\eta$. The errors are summarized in Tables 3 and 4. The first step is the result of Shin (2019). Table 3 lists the error of Shin (2019). There are three steps for calculating the water depth condition using the secant method and three steps for the Newton method at each secant step. Therefore, there are 10 steps; Table 4 presents the errors for step 10. The blanks indicate that they are unsuitable. The series order, $N = 8$, is unsuitable for waves (c) and (d), and the series order, $N = 10$, is unsuitable for wave (d) because they do not satisfy the condition for regular waves. Hence, there is no local extrema between the crest and the trough in a regular wave. The deeper the water depth and the lower the wave height, the smaller the number of series orders required. If the series order is increased beyond the optimal number, the convergence of this study decreases, as presented by Shin (2023). Even for very long waves, the convergence is very stable, unlike other methods.

**Fig. 6** Wave profiles (The legend was arranged in descending order of the crest height. The wave with the highest crest is wave (e), and the wave with the lowest crest is wave (d).)**Table 3** Errors of the first step

Wave	Root mean square error in the DFSBC (%)			
	$N = 8$	$N = 10$	$N = 16$	$N = 35$
a	2.30E-04	2.31E-04	2.31E-04	2.31E-04
b	4.03E-03	4.00E-03	4.00E-03	4.00E-03
c		1.19E-03	1.18E-03	1.18E-03
d			1.18E-03	1.19E-03
e	1.14E-03	1.14E-03	1.14E-03	1.14E-03
f	3.66E-03	3.57E-03	3.55E-03	3.55E-03
g		1.91E-03	1.57E-03	1.58E-03
h			1.68E-03	1.77E-03
Wave	Relative error in the water depth condition (%)			
	$N = 8$	$N = 10$	$N = 16$	$N = 35$
a	1.35E-04	5.50E-07	9.45E-11	2.73E-12
b	-3.32E-01	-3.30E-01	-3.29E-01	-3.29E-01
c		5.54E-03	-1.57E-05	-1.76E-08
d			-8.19E-04	3.32E-06
e	2.79E-04	-2.74E-06	7.34E-10	2.62E-11
f	-1.05E-02	-5.16E-03	1.36E-05	-9.90E-12
g		2.40E-02	-6.74E-04	-2.79E-07
h			-8.60E-03	4.36E-05

Table 4 Errors of the step 10

Wave	Root mean square error in the DFSBC (%)			
	$N = 8$	$N = 10$	$N = 16$	$N = 35$
a	1.78E-09	2.88E-14	8.27E-20	1.02E-21
b	5.19E-07	2.41E-07	6.85E-12	3.62E-25
c		5.02E-06	8.41E-10	1.78E-19
d			6.11E-08	3.11E-15
e	2.37E-08	6.18E-11	2.69E-15	8.91E-21
f	1.44E-05	4.17E-07	7.85E-10	3.28E-20
g		1.01E-04	6.97E-09	1.83E-16
h			3.63E-08	1.19E-12

Wave	Relative error in the water depth condition (%)			
	$N = 8$	$N = 10$	$N = 16$	$N = 35$
a	9.60E-05	9.59E-05	9.60E-05	9.60E-05
b	2.12E-04	2.25E-04	2.09E-04	2.09E-04
c		2.11E-04	4.20E-04	4.20E-04
d			2.75E-05	2.68E-05
e	1.54E-05	1.51E-05	1.51E-05	1.51E-05
f	1.57E-04	7.80E-05	9.23E-05	9.26E-05
g		2.18E-05	4.08E-04	4.05E-04
h			9.40E-05	8.56E-05

6. Conclusions

This paper reported a numerical method to calculate the Fourier coefficient, steepness, and reference depth parameter. The method is much simpler than Fenton's method or HAM. The partial derivatives with respect to wavelength and reference depth, as well as certain parameters, were eliminated utilizing a dimensionless coordinate system. The water depth condition was calculated independently using the shooting method in this study.

Conflict of Interest

The authors declare that they have no conflict of interest.

References

- Baddour, R. E., & Song, S. W. (1988). The rotational flow of finite amplitude periodic water waves on shear currents. *Applied Ocean Research*, 20(3), 163–171. [https://doi.org/10.1016/S0141-1187\(98\)00015-7](https://doi.org/10.1016/S0141-1187(98)00015-7)
- Chaplin, J. R. (1979). Developments of stream-function wave theory. *Coastal Engineering*, 3, 179–205. [https://doi.org/10.1016/0378-3839\(79\)90020-6](https://doi.org/10.1016/0378-3839(79)90020-6)
- Chappelear, J. E. (1961). Direct numerical calculation of wave properties. *Journal of Geophysical Research*, 66(2), 501–508. <https://doi.org/10.1029/JZ066i002p00501>
- Cokelet, E. D. (1977). Steep gravity waves in water of arbitrary uniform depth. *Philosophical Transaction of the Royal Society of London. Series A, Mathematical and Physical Sciences*, 286(1335), 183–230. <https://doi.org/10.1098/rsta.1977.0113>
- Dean, R. G. (1965). Stream function representation of nonlinear ocean waves. *Journal of Geophysical Research*, 70(18), 4561–4572. <https://doi.org/10.1029/JZ070i018p04561>

- Dean, R. G., & Dalrymple, R. A. (1984). *Water wave mechanics for engineers and scientists*. Prentice-Hall, Inc., 368 pp.
- Fenton, J. D. (1988). The numerical solution of steady water wave problems. *Computers & Geosciences*, 14(3), 357–368.
- Fenton, J. D. (1990). Nonlinear wave theories. In B. Le Méhauté & D. M. Hanes (Eds.), *The Sea, Vol. 9: Ocean Engineering Science, Part A*. Wiley.
- Le Méhauté, B., Divoky, D., & Lin, A. (1968). Shallow water waves: A comparison of theories and experiment. *Proceedings of 11th Conference Coastal Engineering*, London, UK, ASCE, 1, 86–107.
- Rienecker, M. M., & Fenton, J. D. (1981). A fourier approximation method for steady water waves. *Journal of Fluid Mechanics*, 104, 119–137. <https://doi.org/10.1017/S0022112081002851>
- Shin, J. (2018). An analytical approximation and a numerical method to progressing periodic water waves on irrotational flow over a horizontal bed. *The 28th ISOPE Conference, Sapporo, Japan* (ISOPE-I-18-567).
- Shin, J. (2019). A regression analysis result for water waves on irrotational flow over a horizontal bed. *International Journal of Offshore and Polar Engineering*, 29(4), 461–466. <https://doi.org/10.17736/ijope.2019.hc17>
- Shin, J. (2022). Solution for water waves with a shear current and vorticity over a flat bed. *International Journal of Offshore and Polar Engineering*, 32(4), 418–423. <https://doi.org/10.17736/ijope.2022.hc29>
- Shin, J. (2023). Newton's method to determine Fourier coefficients and wave properties for deep water waves. *Journal of Ocean Engineering and Technology*, 37(2), 49–57. <https://doi.org/10.26748/KSOE.2022.037>
- Tao, L., Song, H., & Chakrabarti, S. (2007). Nonlinear progressive waves in water of finite depth -an analytic approximation. *Coastal Engineering*, 54(11), 825–834. <https://doi.org/10.1016/j.coastaleng.2007.05.008>
- Vanden-Broeck J. M., & Schwartz, L. W. (1979). Numerical computation of steep gravity waves in shallow water. *Physic and Fluids*, 22(10), 1868–1871. <https://doi.org/10.1063/1.862492>

Appendix

Newton's Method for the Wave Profile

Note that the coefficient c_n and the reference depth D are known in this Appendix. An implicit function $f(\beta, \zeta) = 0$ can be considered as an equation with respect to the dependent variable ζ because the independent variable β is known. Thus, using Newton's method, the explicit representation of the function is

$$\zeta(\beta) = \lim_{r \rightarrow \infty} \zeta^{(r+1)}(\beta) \quad (\text{A1})$$

where (r) stands for the step of Newton's method in this Appendix and

$$\zeta^{(r+1)}(\beta) = \zeta^{(r)}(\beta) - \frac{f(\beta, \zeta^{(r)})}{f'(\beta, \zeta^{(r)})} \quad (\text{A2})$$

where $f(\beta, \zeta)$ is defined as follows using Eq. (3):

$$f(\beta, \zeta) = -\frac{c_0(\sin \sigma \gamma - \sin \sigma D)}{\sigma} \quad (\text{A3})$$

$$+ \sum_{n=1}^N c_n \left\{ \frac{\sinh \langle n \rangle \gamma}{\cosh \langle n \rangle D} \cos n\beta - \tanh \langle n \rangle D \cos \frac{n\pi}{2} \right\}$$

Because $0 \leq |\zeta| < 1$ for all waves, the first step solution $\zeta^{(1)}$ is calculated with the power series expansion of f in ζ and ignoring the higher order terms than the second order. As $f(\beta, \zeta) = 0$, the power series expansion is a quadratic equation with respect to ζ . Then we have

$$\zeta^{(1)} = \frac{-f'(\beta, 0) - \sqrt{\{f'(\beta, 0)\}^2 - 2\{f''(\beta, 0)\}\{f(\beta, 0)\}}}{f''(\beta, 0)} \quad (\text{A4})$$

The other root of the quadratic equation is trivial. Eq. (A4) has the limit that is determined with the discriminant of the quadratic equation. On the other hand, the limit is greater than the wave-breaking limit. Therefore, Eq. (A4) is valid for all waves. Iso-streamlines and iso-vorticity lines are calculated by applying the method presented in this Appendix to Eq. (1) and Eq. (2), respectively. An iso-streamline for the specified value of $\bar{\psi} = \text{constant}$ can be obtained by applying Eq. (A5) to the Newton

method instead of Eq. (A3) and replacing ζ with α .

$$f(\beta, \alpha) = -\bar{\psi} + \alpha - \frac{c_0 \sinh \langle 0 \rangle \alpha}{\langle 0 \rangle} + \sum_{n=1}^N c_n \frac{\sinh \langle n \rangle \alpha}{\cosh \langle n \rangle D} \cos n\beta \quad (\text{A5})$$

The iso-vorticity line for the specified value of $\bar{\Omega} = \text{constant}$ can also be obtained by applying Eq. (A6) to the Newton method instead of Eq. (A3) and replacing ζ with α .

$$f(\beta, \alpha) = -\bar{\Omega} + \varepsilon \left\{ \frac{c_0 \sinh \langle 0 \rangle \alpha}{\langle 0 \rangle} - \sum_{n=1}^N c_n \frac{\sinh \langle n \rangle \alpha}{\cosh \langle n \rangle D} \cos n\beta \right\} \quad (\text{A6})$$

Author ORCID

Author name

Shin, JangRyong

ORCID

0000-0002-0144-2084

Economic Feasibility Analysis According to Seam Location of Ship Pieces

Hyun-Seong Do¹ and Tak-Kee Lee²

¹Graduate student, Department of Naval Architecture & Ocean Engineering, Graduate School,
Gyeongsang National University, Tong-Yeong, Korea

²Professor, Department of Naval Architecture & Ocean Engineering, Gyeongsang National University, Tong-Yeong, Korea

KEYWORDS: Steel price, Pieces, Scrap, Welding cost, Cost reduction, Main plate

ABSTRACT: The structure of a ship is completed by processing various steel plates and welding these plates. This butt welding of plates is defined as a seam in shipyards, and this study seeks to find a way to decrease costs by reducing the utilization of steel through effective seam arrangement. Seams were defined and classified according to purpose, and examples of “pieces” and “main plates” where seam creation had an economical saving effect were selected. For “pieces,” the change in the weight of steel utilized depending on the presence or absence of a seam was calculated, and the resulting change in cost increase was presented. In the case of the “main plate,” the quantity of seams does not change, but an example of cost variation due to the appropriate placement of seams is presented. Hence, a large difference was found in the costs of “pieces” depending on seam location. Thus, it was advantageous to create additional seams. For the “main plate,” it was found that narrow-width and wide-width materials incur more costs. This study demonstrates that creating seams is economically advantageous but may not be preferred owing to the increased workload from a production perspective.

1. Introduction

1.1 Overview

The structure of a ship generally comprises steel plates made of various materials. Specifically, the structural properties for building a ship structure involve cutting and shaping multiple plates to fit the form, and then processed materials are welded in a T or butt-joint form. This study examined the optimal arrangement of seams, which are closely related to butt welding, from the economic perspective.

Steel plate accounts for a large portion of ship components, thus being closely associated with production costs. Significant benefits can be achieved for a shipyard by reducing the amount of steel utilized in shipbuilding. Thus, most shipyards are adopting various methods for reducing the amount of steel utilized, and one of them is creating seams.

Typically, steel plates entail sub-constraints depending on steel manufacturer. Here, sub-constraints are commonly associated with thickness and material grade of the steel, as well as width, length, and weight. Butt welds are inevitable when building a large ship with steel

plate manufactured under such constraints, and these butt welds are defined as seams at shipyards.

Even the pieces cut to have the same area may have different steel scrap rates depending on the arrangement of seams. The steel scrap rate refers to the remaining portion, or unusable scrap metal pieces, after producing steel parts from the original steel plate manufactured by a steel company. For instance, if each company has one sheet of steel weighing 5 t, Company A may utilize 4 t and process 1 t as scraps, while Company B may utilize 4.5 t and process 0.5 t as scraps. Then, the steel scrap rate of Company A is 20%, while that of Company B is 10%. In such a case, company B has higher price competitiveness. Because the production cost of steel accounts for approximately 30% of the shipbuilding cost, the scrap rate of steel directly affects the cost competitiveness of shipyards.

1.2 Related Work

For shipyards to survive the expensive steel market conditions, efficient seam arrangement should be established considering the constraints of steel manufacturers and production costs of shipyards.

Received 10 August 2023, revised 27 September 2023, accepted 18 October 2023

Corresponding author Tak-Kee Lee: +82-55-772-9193, tklee@gnu.ac.kr

It is noted that this paper is revised edition based on proceedings of KSOE 2022 in Daejeon (Do and Lee, 2022) and KAOSTS 2023 in Busan (Do and Lee, 2023).

© 2023, The Korean Society of Ocean Engineers

This is an open access article distributed under the terms of the creative commons attribution non-commercial license (<http://creativecommons.org/licenses/by-nc/4.0>) which permits unrestricted non-commercial use, distribution, and reproduction in any medium, provided the original work is properly cited.

Against this backdrop, there has been an increasing interest in scraps among shipyards, companies developing related programs, and shipbuilding/marine-related departments, and extensive research has been ongoing in the relevant fields.

Lee and Ryu (2013) classified nesting algorithms largely into no-fit polygon (NFP) and grid representation according to the shape representation technique, where the arrangement process and results and the time required are sensitive to the configuration of the fitness function in both approaches. Specifically, the above study focused on the grid representation and applied various fitness functions to compare the arrangement results of each case. It further proposed the fitting function that produces the most efficient arrangement results appropriate for the characteristics of parts for the shipbuilding industry. Kim et al. (2013) introduced the simulated annealing (SA) algorithm and described the methods for finding optimal solutions. Furthermore, they defined five items to consider when arranging seams of the main plate, which were then reflected in the program developed for the study to output optimal solutions and verified its close association with production costs.

Lee et al. (2004) defined an algorithm for part arrangement of a flat bar of ship reinforcements and proposed a method for generating an efficient processing path for efficient arrangement and numerical control cutting utilizing common or continuous cutting. Sheen (2012) attempted to solve the nesting problem without constraints on the shapes being arranged or the boundary shapes of the materials being arranged, utilizing an expert system, which is a knowledge-based inference system. Sheen further provided solutions for four sample cases of nesting, including block puzzles with different characteristics, general nesting, nesting of shipbuilding steel materials, and nesting of materials with heterogeneous boundary shapes employing the proposed method. Elkeran (2013) suggested a guided cuckoo search algorithm, which differs from conventional nesting algorithms. He proposed a novel solution for nesting problems while focusing on optimizing search and generating good layouts based on a hybrid algorithm that integrates a search feature. It further explored methods to enhance the efficiency of nesting through grouping.

Lee et al. (2011) defined the properties of steel areas and studied the part arrangement that can minimize scraps. They proposed methods for bitmap-based sliding part arrangement, steel shape-based rearrangement, and part arrangement and demonstrated the changes in the scrap rate by applying the algorithm to the actual hull nesting. Shim et al. (2009) explained the background and method for reducing the scrap rate. Particularly, the research described the types of feature shapes of parts and examined group arrangements by extracting feature shapes considering cutting efficiency and then collecting and grouping similar patterns. Ryu and Kim (2004) explained several genetic algorithms and performed nesting arrangements employing the NFP method. The optimal solution was found by applying the arrangement order of crossbreeding, mutation, and reproduction. The identified optimal solution was then compared with existing results to find any issues.

Na et al. (2021) attempted a different approach by applying deep learning technology to the part pairing stage of ship parts nesting. A dataset was constructed for training the deep learning network utilizing geometric information of the parts. The geometric information of the parts was input as coordinates to classify and pair similar parts utilizing the NFP-based arrangement method, ultimately improving the performance of the ship parts nesting algorithm.

In addition, related research efforts are continuously put forth in studies by Park et al. (1997), Park and Lee (1997), Park and Kim (1999), and Ryu et al. (2006). Similarly, studies are ongoing to find methods for lowering steel scrap rates, where nesting program developers and shipyards jointly research to develop programs for determining the optimal arrangement of cut parts. The relevant programs include the CADMATIC (n.d.) plate nesting module, an automatic steel-cutting nesting program E-NEST (CACAM, n.d.), and Dr. Nesting (n.d.).

While research has actively been conducted on nesting algorithms, there is a lack of research on efficient seam creation for ships. Therefore, conducting research on efficient seam creation and expanding the research outcomes horizontally to other fields will be advantageous for reducing the overall cost of shipbuilding. This study compared the economic feasibility of arranging seams on pieces with many irregular shapes, which significantly increases steel scrap rates, and of a specific case where scrap rates remain unchanged but the production cost decreases.

2. Seam Types and Correlation with Pieces

This section distinguishes seams according to purpose and introduces the factors influencing seam creation in ship pieces.

2.1 Type of Seams

A seam is classified as follows according to purpose.

- (1) Main plate seams created by considering width extra or constraints arising from the facility and production efficiency of a steel manufacturer
 - The main plate refers to the steel sheet that forms the foundation of the blocks comprising the ship (e.g., deck or bulkhead).
 - Width extra refers to additional costs incurred when ordering steel that is wider or narrower than the typical material produced by the steel manufacturer.
 - Seams can be additionally created depending on a shipyard's production facility (cutting, pre-processing, etc.).
- (2) Piece seams created by considering the steel scrap rate
 - Pieces correspond to this type, which is the main focus of this study.
- (3) Processing seams created to prevent interference between blocks or parts during assembly and mounting
 - Seams can be appropriately created in the interference area or installed afterward, depending on the assembly order.

- Seams can be created and installed afterward when they do not necessarily cause interference but entail extent-related issues.

(4) Seam type which locally increases the thickness of the insertion plate from requiring reinforcement depending on whole ship analysis or local analysis results.

- When heavy structures protrude upwards on the corner or upper side
- When outfitting holes are drilled in major load-bearing parts

Items (1), (3), and (4) can be considered essential and indispensable (designs can consider other options, but standards cannot be changed), while Item (2) can be altered depending on the judgment of a designer (efficiency) within a shipyard. This study focused on the optimal seam location of ship pieces considering the economic feasibility of Item (2), which is the seam of ship pieces.

2.2 Factors Affecting Creation of Scrap Seams and Advantage/Disadvantage

Pieces generally refer to structures inside a ship's hull, comprising medium and large structures such as decks, girders, and floors, as well as small components, including brackets, collar plates, and flat bars. Therefore, ship pieces tend to have irregular shapes compared to shell shapes and various thicknesses, thus significantly increasing the steel scrap rate. Because it is a factor directly associated with the economic feasibility of a shipyard by increasing the production cost, efficient seam creation is mandatory for reducing the steel scrap rate.

The following factors affect the creation and quantity of seams in ship pieces.

- (1) Steel cost (the greatest influential factor)
 - For example, irregularly shaped materials are fabricated more closely to rectangles as the number of created seams increases, reducing the amount of wasted steel. Consequently, the steel usage efficiency increases.
- (2) Amount of welding in butt joints
 - As the seam lengthens, the weld length also increases, which results in increased workload.
- (3) Number of cut parts
 - An increased number of parts due to created seams results in an increased workload for material management.
- (4) Deformation due to cutting
 - There is a high probability of cutting deformation when cutting pieces that have a longer length than the width. Deformation can be minimized if seams are created in the width direction at appropriate intervals. In this case, the number of seams increases, but the reduction in field rework due to deformation has a more significant impact.

Table 1 summarizes the advantages and disadvantages with respect to the increased seam quantity.

Table 1 Comparison of increasing seam quantity

Seam quantity	Few seams	Many seams
Advantage	Increase in production efficiency (reduced weld length and inspection point)	Decrease in steel cost; Reduced deformation by cutting
Disadvantage	Increase in scrap >> Increase in steel cost	Decrease in production efficiency

3. Economic Feasibility of Seam Creation

3.1 Selection of Comparison Targets and Prerequisites

This study examines two cases where seam creation can induce economic savings. The cases entail the main plate and small pieces, which will be further explained in Section 3.2. In addition, the ship type was designated as a container ship, built in a series of five vessels. Because container ships have a large amount of curvature due to their linear characteristics and relatively heavy structural weight, they were selected for this study as the impact of steel savings is particularly pronounced.

For economic analysis, the following assumptions were made in terms of steel prices and welding-related costs (see, Table 2). First, the steel price was set at 1.1 million KRW per ton (Kwon, 2022). Furthermore, the welding-related costs were assumed based on the standards of welders in the construction industry, similar to the shipbuilding sector. It was set at 240,000 KRW per day and 40,000 KRW per hour (30,000 KRW per hour + facility usage amounting to 10,000 KRW per hour, which includes complex costs such as production time, increased number of managed parts, etc.; construction industry wages in the first half of 2023). Here, the welding efficiency was conservatively assumed based on practical standards. It was assumed to be 10 m per hour for automatic welding and 2 m per hour for manual welding.

Table 2 Target selection and prerequisites

Item	Precondition
Ship type	Container (5 ship series)
Steel cost	1,100,000 KRW/t
Welding & ETC cost	240,000 KRW/d 40,000 KRW / (man/h)
welding efficiency	SAW Welding 10 m/h CO ₂ Welding 2 m/h

3.2 Cases Where Seam Creation is More Economically Advantageous

3.2.1 Case 1: Economic seam creation of small pieces

The shape illustrated in Fig. 1 is predominantly found in a container ship. Almost every block incorporates structures in the shapes of “ㄱ,” “ㄴ,” and “ㄷ,” especially in T-Blocks (transverse bulkhead blocks). It is assumed that materials with these shapes are abundant in T-Blocks, with an average quantity of around 40 pieces per block.

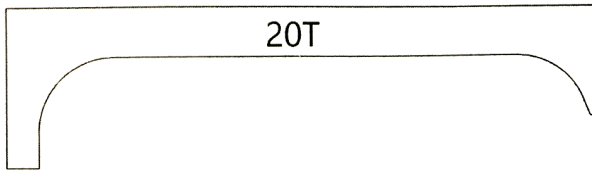


Fig. 1 Typical bracket shape in T-block of container ship

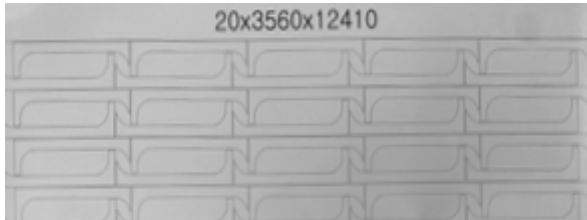


Fig. 2 General arrangement of 40 pieces in Case 1

Fig. 2 illustrates the arrangement of 40 target parts on a single circular steel plate, where the parts are repetitively arranged considering the geometric characteristics of the pieces. In this case, the estimated total weight of steel, considering the discarded steel, was 6.94 t. When converted into monetary value and considering a series construction of five vessels, the total cost of steel was approximately 38 million KRW. This case is defined as Case 1-1.

Here, a single seam was created in a piece having the shape illustrated in Fig. 1 to minimize the discarded steel, and the optimal location for creating the seam was identified.

Fig. 3 presents the detailed shape and dimension of the target piece where the thickness is 20 mm and the quantity is defined as 40. The efficient seam arrangement was determined by selecting various seam locations and comparing the resulting scrap rates. Because the area within 100 mm from the round end (R.END), which often receives

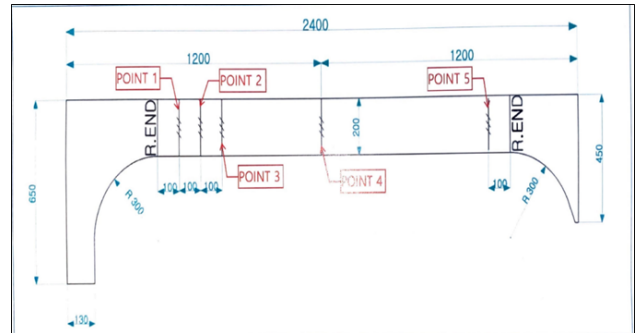


Fig. 3 Dimension of target piece and location of each point

shipowner/classification comments, was excluded, seam locations were defined as the minimum of R.END + 100 mm, and the locations of each seam were selected as Points 1–5 in the figure (Case 2-6).

The steel scrap rate can be calculated with the equation below.

$$\frac{\text{Used steel weight} - \text{pieces weight}}{\text{Used steel weight}} \times 100 \quad (1)$$

Based on the results at Points 1–4, the scrap rate decreased as the seam location approached the R.END and increased as it moved away. This result can be interpreted as the discarded steel area increasing as the seam location moves away from the R.END because the available options for arrangement decrease. Point 5 has the highest scrap rate due to the geometric characteristics at both left and right ends (refer to Fig. 4 and Table 3). Therefore, creating the seam at Point 1, which is closest to the R.END, is optimal from an economic aspect, and such a trend can be inferred for other similar structures.

If creating two seams is considered, simultaneously applying at both Points 1 and 5 will result in a very low scrap rate; Fig. 5 illustrates the

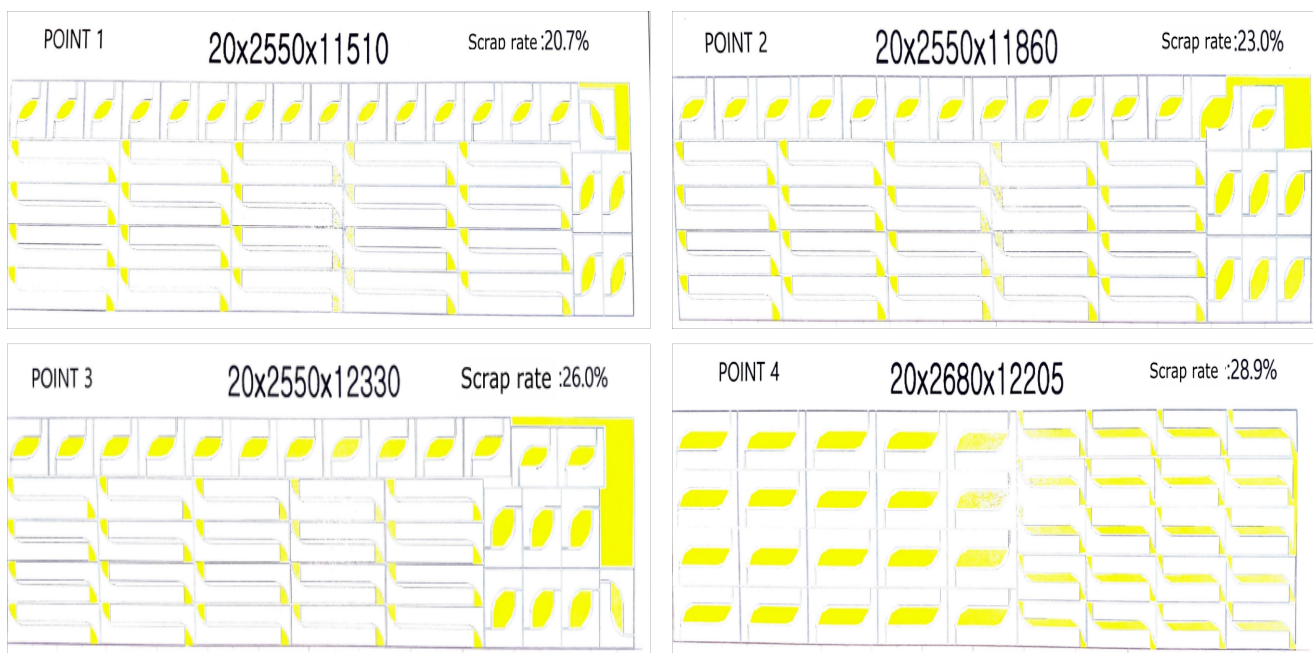
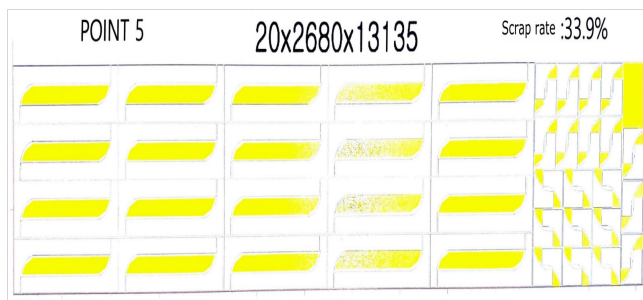
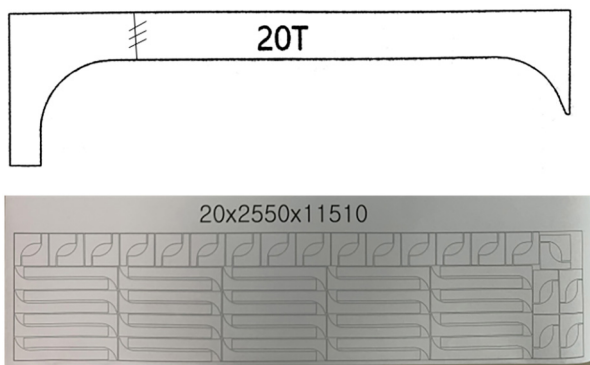


Fig. 4 Scrap rate of steel plates by Points 1–4

Table 3 Weight and scrap rate of steel utilized at each point

Case	Seam	Piece weight (t)	Steel weight (t)	Scrap rate (%)	Cost (KRW)	Reduced cost (Case 1-1 base)	ETC.
Case 1-1	None	3.65	6.94	-	38,150,000	-	
Case 1-2	Point 1	3.65	4.61	20.7	25,340,000	12,810,000	2
Case 1-3	Point 2	3.65	4.75	23.1	26,130,000	12,020,000	3
Case 1-4	Point 3	3.65	4.94	26.0	27,170,000	10,980,000	4
Case 1-5	Point 4 (Center)	3.65	5.14	29.0	28,270,000	9,880,000	5
Case 1-6	Point 5	3.65	5.53	33.9	30,420,000	7,730,000	6
Case 1-7	Point1+5	3.65	4.49	18.6	24,700,000	13,450,000	1

**Fig. 5** Scrap rate of case with two seams at Points 1 and 5**Fig. 6** Arrangement of 40 pieces with one seam in Case 1

part arrangement for this scenario and the calculated scrap rate. However, this case entails an increased number of welding joints from additional creation of seams, thus being an unfavorable choice in terms of production efficiency, especially for many parts.

Fig. 6 illustrates the location of a seam generated at Point 1, which was predicted to be the optimal seam location in the piece. When the inherent symmetry in the shape of the left side is considered, creating seams, as illustrated in the figure below, allows for a repetitive, rotationally symmetric arrangement of the small parts on the left-hand side.

For cost analysis, the target vessel was assumed to be a container ship with a series of five ships, with a steel price assumed at 1.1 million KRW per ton (Kwon, 2022). Because the steel weight per ship for the cutting arrangement presented in Fig. 6 is 4.61 t, the total steel cost amounts to approximately 25.36 million KRW. Approximately 8

m of welding length is added per ship due to the created seam, resulting in a total welding length of approximately 40 m for the five ships. Because manual welding is inevitable considering the installation location, an additional welding cost of approximately 800,000 KRW is incurred. Furthermore, the feasibility of manual or automatic welding was determined based on field practical guidelines. The welding cost was assumed adopting the standards of welding workers in the construction industry, which is similar to the shipbuilding sector, with 240,000 KRW per day and 40,000 KRW per day (30,000 KRW per hour + facility usage amounting to 10,000 KRW per hour; construction industry wages in the first half of 2023).

Comparing the cost of 38 million KRW when arranging materials in the shape of “ㄱ” without seams on the original steel plate against the cost of 25.36 million KRW when creating a seam at Point 1, the cost savings from the steel amount to 12.64 million KRW. Considering the additional welding cost of 800,000 KRW, the overall input cost for creating the seam is calculated to be 1.184 million KRW less. Therefore, generating the seam is advantageous in terms of cost if it results in utilizing less steel plate.

3.2.2 Economical seam creation for rectangular main plate type

It is hard to expect a reduction in scrap rate based on the seam location for rectangular and square-shaped steel sheets. Creating seams can lead to a slight increase in scraps due to the need to maintain gaps between the required parts during cutting and the margin for the outer outline of steel, thus resulting in decreased productivity.

However, adjusting the arrangement of existing seams rather than adding new seams may not reduce the final scrap. However, it can lower the overall steel cost and reduce the overall manufacturing cost of the ship. Determining effective seam location is closely associated with the width extra mentioned previously in Section 2.1. Width extra refers to the additional cost paid when ordering steel that falls outside the range of widths generally produced by the steel mill. The extra price increases as the narrow-width or wide-width sheet metal has the maximum value, and the thickness is higher.

The width of steel plates produced by domestic steel mills currently ranges from 3000 to 3600 mm. For analyzing the economic feasibility, it is assumed that the cost of width extra is 50,000 KRW per ton for both narrow- and wide-width. This study examined the main plate,

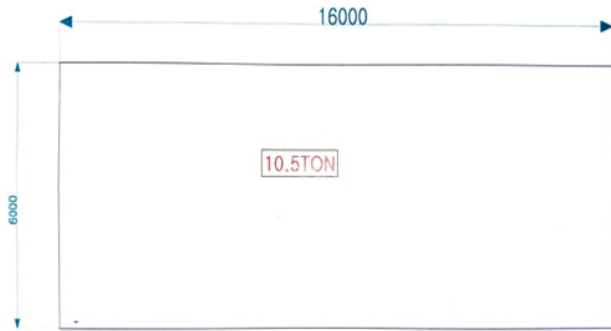


Fig. 7 Dimension of main plate

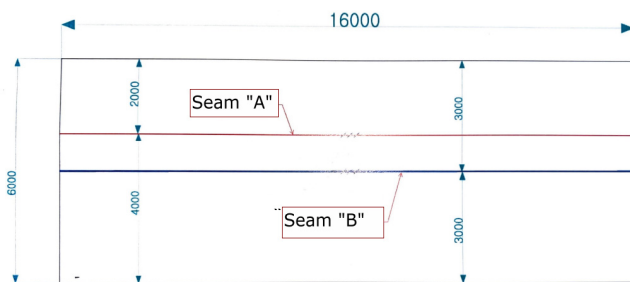


Fig. 8 Two cases of seam positions related with extra width

Table 4 Comparison of steel costs considering extra width

Breadth (mm)	Weight (t)	Steel price (KRW)	Extra width cost (KRW)	Sum (KRW)
2,000	10.5	11,550,000	525,000	12,075,000
4,000				
3,000	10.5	11,550,000	0	11,550,000
3,000				

which has a width of 6000 mm, as illustrated in Fig. 7. Seam creation is inevitable because the width of the target main plate is greater than the producible width of the steel mill. As illustrated in Fig. 8, it is assumed that Seam “A” has widths of 2000 and 4000 mm, while Seam “B” has a width of 3000 mm. Table 4 presents the comparison of steel costs for three steel sheets with respect to width.

4. Conclusion

From the perspective of higher economic feasibility, it was observed that creating seams in materials with small piece shapes is economically advantageous regardless of steel price. Furthermore, creating seams in the pieces closer to R.END is more advantageous to lower the scrap rate. This study has found that appropriately generating seams to reduce scrap rates is more advantageous than the increased welding costs due to seam creation in the current high-priced steel market. This outcome proves that there is ultimately a difference in the production cost. It was also found that adjusting the location of seams without adding additional seams can create economic benefits.

Most shipyards strive to lower production costs from many different perspectives (Na, 2018). In addition to the seam creation mentioned

previously, other efforts are put forth to minimize costs by placing small parts in scrap areas or through joint arrangements between blocks. Certain approaches are avoided from the production perspective because the welding amount increases. The reason is that seam creation results in cost savings in shipbuilding construction costs, but the increase in welding length and inspection points at actual worksites increases workload. From the perspective of economic feasibility, the advantage or disadvantage of seam creation varies depending on the fluctuation of raw material prices. This study requires further review if the fluctuation of steel prices becomes greater. The findings of this study are expected to facilitate shipyards to save costs as the steel price rises.

Our future research will involve finding the optimal seam location by incorporating nesting methods and programs. Because the effects of seam creation are insignificant for a single material, greater cost savings can be achieved by discovering other targets through which seam creation can be more advantageous depending on the nesting method and applying them horizontally to other fields. In addition, the scope will be expanded to investigate the effects of seam creation on a wider range of pieces having various shapes, as well as efficient seam arrangement in the shell. Ultimately, research extending beyond the efficient seam arrangements for determined shapes will be conducted to explore structural determination that induces optimal seam locations.

Conflict of Interest

Tak-Kee Lee serves as a member of journal publication committee of the Journal of Ocean Engineering and Technology. However, he had no role in the decision to publish this article. No potential conflict of interest relevant to this article was reported.

References

- CADMATIC. (n.d.). Plate nesting. <https://www.cadmatic.com/ko/marine/ship-design-software/plate-nesting/>
- Construction Association of Korea (CAK). (2023). Market wages in the construction industry in 2023. *The comprehensive market price information*. https://cmpi.or.kr/manage/noim_data.asp?part=noim&page=gong&n_type=gong&n_date=&ser
- CSCAM. (n.d.). E-NEST. http://www.cscam.co.kr/sub/sub06_0302.php?mode=view&idx=11
- Do, H. S., & Lee, T. K. (2022). Economic review on seam creation of pieces considering steel price. *Proceedings of the Korean Society of Ocean Engineers 2022 Fall Conference* (pp. 506–510), Daejeon, October.
- Do, H. S., & Lee, T. K. (2023). A study on optimal placement of internal seams considering economics. *Proceedings of the Korean Association of Ocean Science and Technology Societies 2023 Spring Conference*. Busan, April.
- Dr.Nesting. (n.d.). What is Dr.Nesting? <https://www.cadian.com/kr/product/nesting/drnesting.asp>

- Elkeran, A. (2013). A new approach for sheet nesting problem using guided cuckoo search and pairwise clustering. *European Journal of Operational Research*, 231(3), 757–769. <https://doi.org/10.1016/j.ejor.2013.06.020>
- Kim, Y. T., Han, M. K., Beak, G. D., Hwang, J. S., & Lee, D. H. (2013). An introduction to the optimization method for weld seam positions using SA. *Proceedings of the Korean Institute of Information and Communication Sciences Conference*, 540–543.
- Kwon, O. E. (2022, April 25). Steel production cuts around the world ... Steel prices soar]. *ChosunBiz*. <https://biz.chosun.com/industry/company/2022/04/25/G7ITY37RUBDNZAATAAWMGCY524/>
- Lee, C. S., Park, S. D., Park, G. R., Im, T. W., & Yang, Z. H. (2004). A study on layout method for effective NC cutting path of the flat-bar. *Korean Journal of Computational Design and Engineering*, 9(2), 102–111.
- Lee, C. S., Heo, E. Y., Kim, J. M., & Kim, D. S. (2011). A study of the efficient nesting considering scrap feature. *Proceedings of the Society of CAD/CAM Engineers*, 533–537.
- Lee, H. B., & Ryu, W. S. (2013). Determination of nesting algorithm fitness function through various numerical experiments. *Journal of Ocean Engineering and Technology*, 27(5), 28–35. <https://doi.org/10.5574/KSOE.2013.27.5.028>
- Na, K. H. (2018, January 14). Shipbuilding industry, It's a problem to win orders without cost reduction. *Mediapen*. <http://www.mediapen.com/news/view/324348>
- Na, G. Y., Cheon, S. U., & Yang, J. S. (2021). A deep learning-based part classification method for ship part pairing in nesting problems. *Korean Journal of Computational Design and Engineering*, 26(4), 514–524. <http://doi.org/10.7315/CDE.2021.514>
- Park, J. W., Han, C. B., & Lee, H. S. (1997). A study on the nesting S/W development of piece with PC-CADRA. *Journal of Ocean Engineering and Technology*, 11(4), 239–248.
- Park, J. W., & Lee, H. S. (1997). A study on the piece creation on hull-structure with PC-CADRA. *Journal of Ocean Engineering and Technology*, 11(3), 191–199.
- Park, M. K., & Kim, W. D. (1999). Construction of an automation system for hull part nesting and cutting. *Journal of the Industrial Technology Research Institute*, 17, Korea Maritime University. <http://repository.kmou.ac.kr/bitstream/2014.oak/6282/1/000002179813.pdf>
- Ryu, B. H. & Kim, D. J. (2004). A study on the irregular nesting problem using genetic algorithm and no fit polygon methodology. *Journal of Ocean Engineering and Technology*, 18(2), 77–82. <https://www.joet.org/journal/view.php?number=1723>
- Ryu, G. S., Choi, J. Y., & Kim, I. G. (2006). A design and implementation of web based integrated nesting system. *Journal of KIISE : Computer Systems and Theory*, 33(1), 44–51.
- Sheen, D. M. (2012). Nesting expert system using heuristic search. *Journal of Ocean Engineering and Technology*, 26(4), 8–14. <https://doi.org/10.5574/KSOE.2012.26.4.008>
- Shim, J. H., Lee, C. S., & Kim, D. S. (2009). Feature extract and auto nesting algorithms for cutting efficiency of ship building part. *Proceedings of the Society of CAD/CAM Engineers*, 383–389.

Author ORCIDs

Author name	ORCID
Do, Hyun-Seong	0009-0000-5464-1864
Lee, Tak-Kee	0000-0002-5944-156X

Structural Response Analysis for Multi-Linked Floating Offshore Structure Based on Fluid-Structure Coupled Analysis

Kichan Sim¹, Kangsu Lee^{2,3} and Byoung Wan Kim^{2,3}

¹Ph. D. Student, Department of Ship & Ocean Engineering, University of Science & Technology, Daejeon, Korea

²Professor, Department of Ship & Ocean Engineering, University of Science & Technology, Daejeon, Korea

³Principal researcher, Department of Eco-friendly Ocean Development Research Division, Korea Research Institute of Ships & Ocean Engineering., Daejeon, Korea

KEYWORDS: Multi-linked floating offshore structure, Fluid-structure coupled analysis, Connection condition, Pretension, Bending stress

ABSTRACT: Recently, offshore structures for eco-friendly energy, such as wind and solar power, have been developed to address the problem of insufficient land space; in the case of energy generation, they are designed on a considerable scale. Therefore, the scalability of offshore structures is crucial. The Korea Research Institute of Ships & Ocean Engineering (KRISO) developed multi-linked floating offshore structures composed of floating bodies and connection beams for floating photovoltaic systems. Large-scale floating photovoltaic systems are mainly designed in a manner that expands through the connection between modules and demonstrates a difference in structural response with connection conditions. A fluid-structure coupled analysis was performed for the multi-linked floating offshore structures. First, the wave load acting on the multi-linked offshore floating structures was calculated through wave load analysis for various wave load conditions. The response amplitude operators (RAOs) for the motions and structural response of the unit structure were calculated by performing finite element analysis. The effects of connection conditions were analyzed through comparative studies of RAOs and the response's maximum magnitude and occurrence location. Hence, comparing the cases of a hinge connection affecting heave and pitch motions and a fixed connection, the maximum bending stress of the structure decreased by approximately 2.5 times, while the mooring tension increased by approximately 20%, confirmed to be the largest change in bending stress and mooring tension compared to fixed connection. Therefore, the change in structural response according to connection condition makes it possible to design a higher structural safety of the structural member through the hinge connection in the construction of a large-scale multi-linked floating offshore structure for large-scale photovoltaic systems in which some unit structures are connected. However, considering the tension of the mooring line increases, a safety evaluation of the mooring line must be performed.

1. Introduction

The technology for utilizing maritime space has been consistently studied for purposes such as securing food resources through fisheries and developing ocean resources like seabed oil and natural gas. In particular, a recent focus on eco-friendly energy has resulted in active research into the development of offshore structures for renewable energy generation. Specifically, these offshore structures for renewable energy generation are generally operated as large-scale complexes. Thus, various numerical methods have been developed to analyze the entire system, and studies have also been conducted to improve the performance of these structures by analyzing their configuration and the effect of wave load conditions. Park and Choung

(2023) conducted a direct strength assessment with the main load factors of acceleration and nacelle thrust in a 10-MW offshore wind power system based on the internal code HydroQus (Yoon and Choung, 2023). They analyzed vulnerable parts of the substructure based on the assessment results. Song et al. (2014) analyzed the effect of initial conditions on the transient response characteristics of floating wind turbines. Chen et al. (2021) researched a method to predict fatigue life with approximately 2% error compared to the complete elastic model, utilizing aerodynamic decoupling and a mode-based order reduction method. Kim et al. (2022b) conducted a numerical analysis study, applying second order wave loads, nonlinear Froude-Krylov forces, and the damping force of the power take-off (PTO) system in a tension-leg platform (TLP)-based hybrid power generation

Received 9 August 2023, revised 27 September 2023, accepted 18 October 2023

Corresponding author Byoung Wan Kim: +82-42-866-3932, kimbw@kriso.re.kr

© 2023, The Korean Society of Ocean Engineers

This is an open access article distributed under the terms of the creative commons attribution non-commercial license (<http://creativecommons.org/licenses/by-nc/4.0>) which permits unrestricted non-commercial use, distribution, and reproduction in any medium, provided the original work is properly cited.

platform with excellent motion performance in waves.

Ghigo et al. (2022) selected Lampedusa Island as the case study and performed a performance assessment of a floating photovoltaic power generation system through numerical analysis of loads caused by waves and currents. Na et al. (2021) compared and analyzed the results of model tests and field performance test for the unit platforms designed to construct large-scale floating photovoltaic power generation systems, reviewing key performance parameters such as sway reduction and stability. The Korea Research Institute of Ships & Ocean Engineering (KRISO) developed multi-linked floating offshore structures composed of numerous floating bodies connected by beams, allowing for expansion through inter-unit connections. The characteristics of these multi-linked floating offshore structures vary according to several design elements, such as the size of the structure, initial tension of mooring lines, and method of unit structure connection. Among these design components, the magnitude of the initial tension in the mooring lines can significantly alter the wave loads acting on the structure and, consequently, the motion and structural response. Therefore, reviewing the structure's response to wave loads and designing sufficient initial mooring line tension is essential.

In addition, as the motion, structural response and the characteristics of the mooring line tension change according to the connection method between unit structures, it is necessary to analyze the response of structures for the safe design of super-large systems composed of multi-linked floating offshore structures. Thus, we performed a fluid-structure coupled numerical analysis to examine the impact of the connection condition (a major design element) on the motion and structural response of the multi-linked floating offshore structures developed by the KRISO. Considering multi-linked floating offshore structures have numerous floating bodies, they require extensive computational resources; hence, the wave loads were modeled as nodal forces to reduce the computational cost. Based on this fluid-structure coupled numerical analysis technique, various fluid-structure coupled numerical analyses were performed under different wave load conditions and three different connection conditions to analyze the effect of connection conditions on the expansion of the entire system. This analysis included a comparative study of six degrees of freedom motion characteristics, the maximum magnitude and occurrence location of the dominant bending stress in the multi-linked floating offshore structures, and the tension in the mooring lines.

2. Fluid-Structure Coupled Analysis for Multi-Linked Floating Offshore Structures

2.1 Multi-Linked Floating Offshore Structures for Photovoltaic Generation Systems

Offshore photovoltaic generation systems typically have multiple interconnected modules. As illustrated in Fig. 1, a numerical analysis was conducted on the multi-linked floating offshore structures composing a 2-MW-class offshore photovoltaic power generation

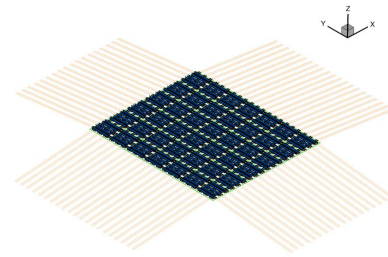


Fig. 1 Multi-linked floating offshore structure for 2-MW floating photovoltaic system

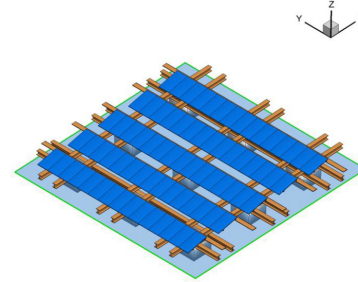


Fig. 2 Unit structure of multi-linked floating offshore structure

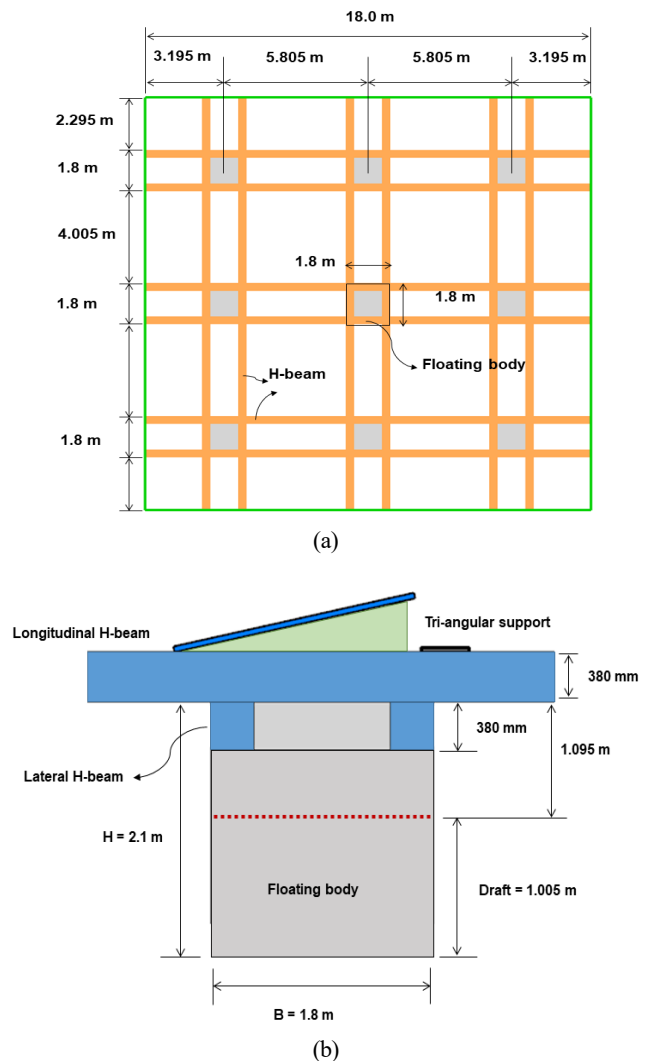


Fig. 3 Dimensions of unit structure: (a) top view of unit structure; (b) side view of buoy and beam connector

Table 1 Properties and dimensions for multi-linked floating offshore structures

Item	Property	
Buoy	Material	Aluminum
	Dimension (m)	$B \times L \times H \times t1 = 1.8 \times 1.8 \times 1.72 \times 0.01$
	Draft (m)	1.005
	Mass (kg)	593.957
	Center of gravity (m)	0.634
	Center of buoyancy (m)	-0.503
Connector	Material	Aluminum
	Elastic modulus (GPa)	69.60
	Shear modulus (GPa)	26.17
	Dimension (m)	$B \times H \times t2 \times t3 = 0.34 \times 0.38 \times 0.03 \times 0.03$
Mooring line	Material	Polyester rope
	Spring constant (N/m)	62,336.97
	Diameter (m)	0.044
Unit structure	Dimension (m)	$B \times L \times \text{Draft} = 18 \times 18 \times 1.005$
	Mass (kg)	30,041

Note. B = Breadth; L = Length; $t1$ = thickness of buoy; $t2$ = thickness of web; $t3$ = thickness of flange

system. The system in Fig. 1 is interconnected through 72 modules, installed in a sea area with a water depth of 9 m, and linked to 204 mooring lines in a taut mooring configuration. These multi-linked floating offshore structures can be expanded by joining unit structures, as depicted in Fig. 2, and each unit comprises 9 floats and 36 beam structural members. This study examined a structure's motion and structural responses based on numerical analyses and model testing results of a 2-MW-class offshore photovoltaic power generation system.

Furthermore, we researched structures with two-unit structures to analyze the effect of the mooring line tension and structural response, depending on the connection method between the unit structures of the multi-linked floating offshore structures. Detailed specifications of the

unit structures are presented in Fig. 3 and Table 1. For mooring lines, similar to the 2-MW-class system, 36 lines are connected in a taut mooring method.

2.2 Numerical Analysis of Fluid-Structure Interaction for Multi-Linked Floating Offshore Structures

In this research, a fluid-structure coupled numerical analysis was performed to consider the interactions among floating bodies, beam structural members, and mooring lines. Hydrodynamic analysis was initially conducted to calculate wave loads acting on the multi-linked floating offshore structures, employing a high-order boundary element method (HOBEM) that improves accuracy and convergence compared to conventional boundary element methods. The analysis considered the interaction between each buoyancy body. It included hydrodynamic characteristics, such as wave loads in the frequency domain, added mass, and damping, as calculated in Eq. (1) below (Kim et al., 2013).

$$(-\omega^2 [M_B + M_{add}(\omega)] - i\omega [C_B(\omega)] + [K_B])x(\omega) = f_{wave}(\omega) \quad (1)$$

Here, $[M_B]$ and $[M_{add}]$ represent the mass of the floating body and added mass, respectively, $[C_B]$ denotes hydrodynamic damping, and $[K_B]$ represents hydrodynamic restoring stiffness. $x(\omega)$ and $f_{wave}(\omega)$ signify the motion of the floating body and wave load, depending on the wave frequency (ω).

After converting the wave loads and hydrodynamic characteristics calculated in the frequency domain to the time domain, they were applied to a finite element model as load conditions. Finally, a structural analysis in the time domain was performed with the motion equation as in Eq. (2).

$$[M + M_B + M_{add}(\omega)]\ddot{u}(t) + [C + C_B(\omega)]\dot{u}(t) + [K + K_B]u(t) = f_{wave}(t) \quad (2)$$

Here, $[M]$, $[C]$, and $[K]$ denote the mass, damping, and stiffness of the structural analysis model for the multi-linked floating offshore

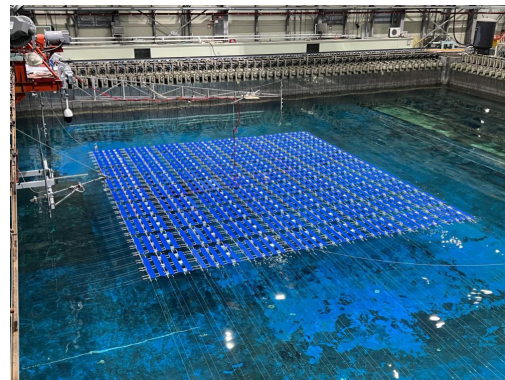
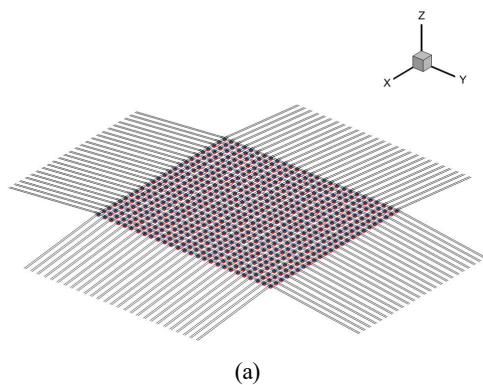


Fig. 4 (a) Numerical model and (b) structure model for model test for 2-MW photovoltaic system

structures, and $u(t)$ represents displacement in the time domain. The motion equation of Eq. 2 applied the representative implicit numerical method, the Newmark algorithm, for the numerical analysis.

Commencing with an analysis of a 2-MW-class offshore photovoltaic power generation system, numerical modeling was conducted as depicted in Fig. 4(a), followed by fluid–structure coupled analysis. In addition, model tests were conducted in the ocean engineering basin at KRISO, as depicted in Fig. 4(b), facilitating the measurement of the construction’s motion and structural responses (Kim, 2023). These model tests were executed at a 1/15 model scale; the floating bodies of the structure were fabricated with expanded polypropylene, and the beam connectors were made of aluminum. Furthermore, the stiffness of the mooring lines was simulated with springs, and a separate anchor system was fabricated and connected to the mooring lines. To measure the six degrees of freedom motion response at the center and edges of the entire structure and the

structural response, the bending stresses were scaled to record the strain on the beam connectors where maximum stress occurred. A series of regular, irregular wave tests for head seas, oblique seas, and beam seas was conducted to measure the structure’s response to compare with numerical analysis results. The numerical analysis and model test results for the motion and structural response of the target structure are illustrated in Figs. 4 and 5. The numerical analysis results did not significantly differ in response magnitude or overall trend compared to the model test results. The heave and roll motion responses in Fig. 5 represent the numerical and experimental measurement results at the system’s central position, the most significant translational and rotational movements among the six degrees of freedom motions. Unlike the heave response, which demonstrated a similar trend across all wave directions, the roll motion had the most significant response perpendicular to the wave direction. In the case of bending stress, as illustrated in Fig. 6, the model test

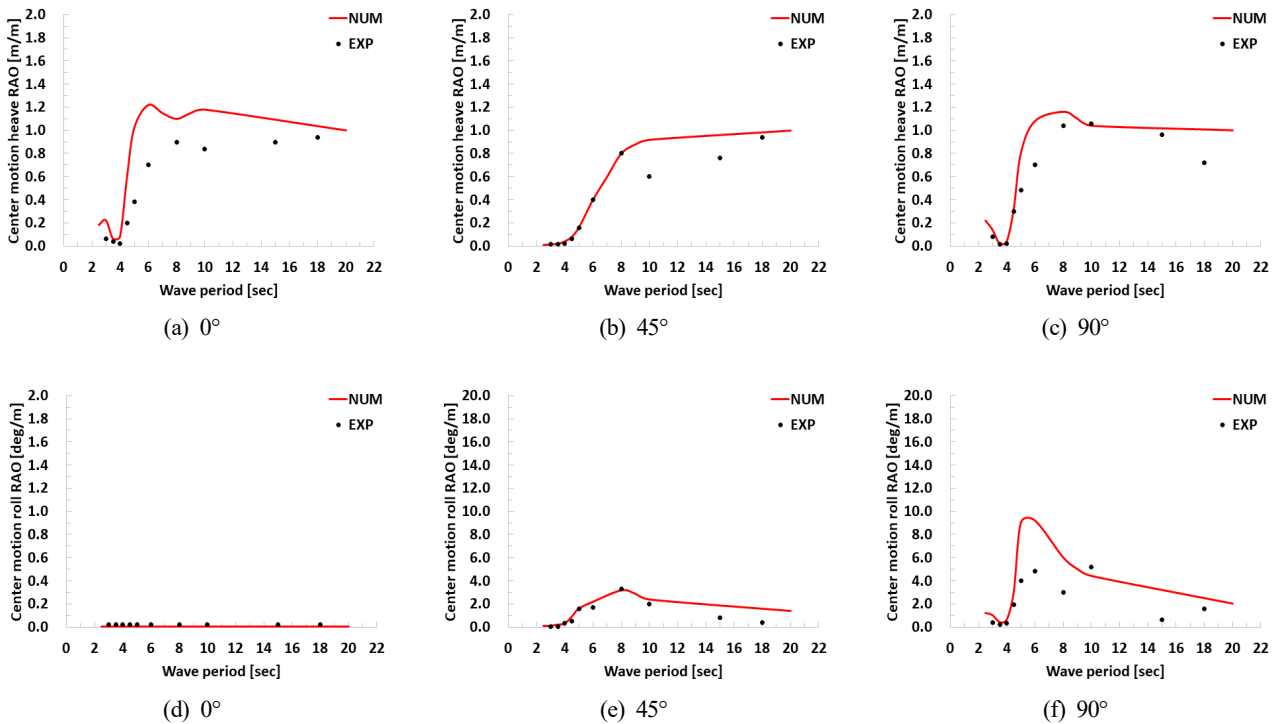


Fig. 5 Heave and roll motion response amplitude operator (RAO) for 2-MW photovoltaic system with heading angle (a), (d) (Kim, 2023)

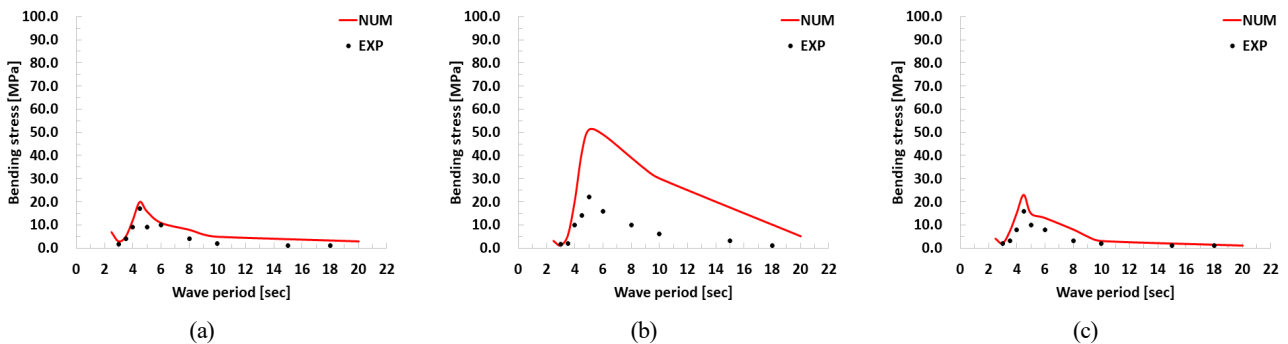


Fig. 6 Bending stress RAO of beam connector with heading angle (a) 0°, (b) 45°, and (c) 90° (Kim, 2023)

results were almost identical across all wave directions. However, a considerable discrepancy with numerical results was noted under oblique wave conditions at 45° , attributed to factors such as tolerances in the model fabrication process and limitations in realizing the ideal connection conditions at the joints.

Moreover, under oblique wave conditions, discontinuous stress occurred at the connections between the unit structures, leading to a significantly greater stress difference than other wave conditions. As the unit structures expanded, the cumulative error caused by the discontinuous stress at the connections became apparent, explaining the variation in the bending stress of the beams under the beam sea conditions in Fig. 6. As the above research findings indicate, the design of connections is critically important for the overall system of multi-linked floating offshore structures, which comprises numerous interconnected unit structures. Consequently, we conducted a numerical analysis on multi-linked floating offshore structures with two-unit structures to analyze the effects of movement and structural responses according to connection conditions, focusing specifically on variations in mooring line tensions and structural response differences based on the connection methods between unit structures.

2.3 Numerical Model

The numerical model for the multi-linked floating offshore structures can be divided into two parts: a panel model for calculating wave loads and hydrodynamic characteristics acting on the floating structures and a structural analysis model for computing the responses of structural beams and mooring lines. As illustrated in Fig. 7, the panel model includes 432 high-order elements with nine nodes each. The structural analysis model comprises 1056 beam elements representing structural members and mooring lines, as depicted in Fig. 8. In the case of the structural analysis model, the floating structure is modeled as a single node located at the center of the floating structure. The wave loads calculated through the hydrodynamic analysis are integrated over the area of high-order elements comprising the floating structure and applied as point loads to the node. In addition, to transmit the wave loads to the beam structural members without energy loss, each node is modeled with four beam elements, which has ver large

stiffness, effectively linking the beam elements to the node. This approach significantly reduces the computational cost of numerical calculations as the number of multi-linked floating offshore structures increases. The connections between unit structures were modeled with various connection conditions, such as hinges. In contrast, the mooring lines were modeled as beam elements incorporating design tensions and stiffness of the lines. Also, fixed translational degree of freedoms were applied to the nodes as boundary conditions representing the anchors of the mooring lines.

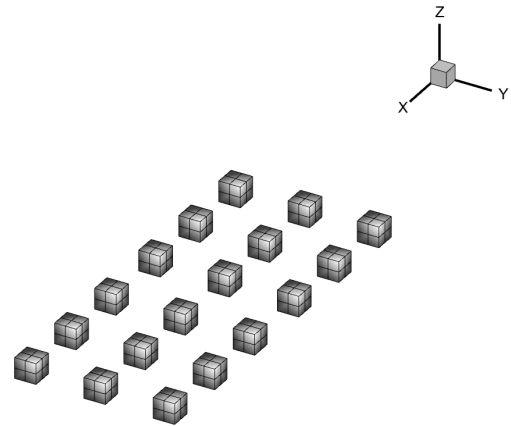


Fig. 7 Numerical model for hydrodynamic analysis

Table 2 Wave load condition

Item	
Heading angle ($^\circ$)	0, 45, 90
Wave period (s)	3.0, 3.25, 3.5, 3.75, 4.0, 4.25, 4.5, 4.75, 5.0, 5.25, 5.50, 5.75, 6.0, 6.25, 6.50, 6.75, 7.0, 7.25, 7.50, 7.75, 8.0, 9.0, 10.0, 20.0, 40.0
Wave spectrum	JONSWAP
Significant wave height (m)	1.0
Modal period (s)	4.0
Gamma	2.5

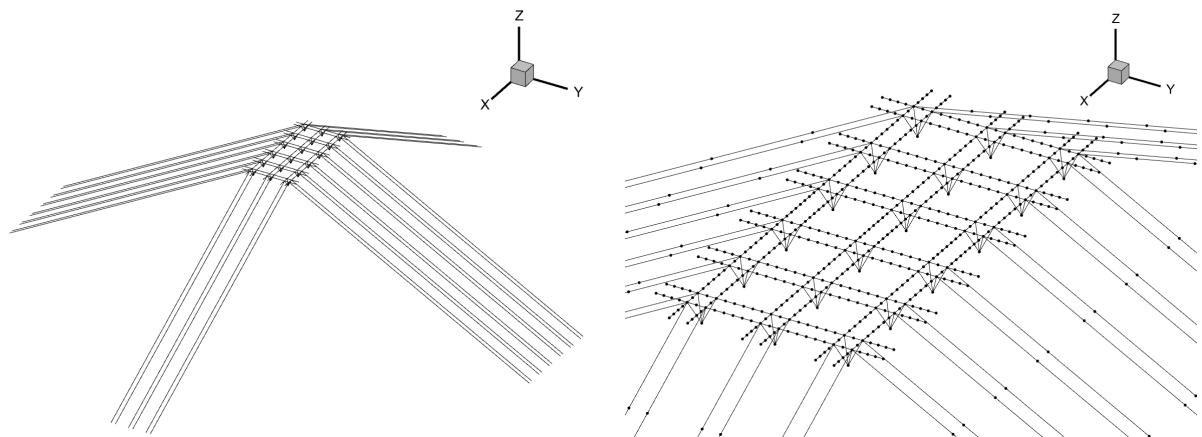


Fig. 8 Numerical model for structural analysis

3. Structural Safety Assessment of Multi-Linked Floating Offshore Structures

Through fluid-structure coupled analysis of the aforementioned numerical model, we calculated the motion and structural responses of the structures with wave load condition presented in Table 2. The response amplitude operator (RAO) for motion and structural response were derived and analyzed based on the analysis results under regular wave conditions. Furthermore, numerical analyses under irregular wave conditions were conducted to evaluate the structural safety based on maximum bending and shear stresses and mooring line tensions affecting the structural beam and mooring lines. We also reviewed the locations where each structural response was maximized.

3.1 Motion Response Characteristics of Multi-Linked Floating Offshore Structures

The motion response of multi-linked floating offshore structures was calculated from the center of gravity of each unit structure and is

represented in Fig. 9. Excluding the heave motion, all other motions exhibit their maximum response between 2.0 and 6.0 s, decreasing as the wave period lengthens. Heave demonstrates small variation with wave direction, converging towards a 0.5-m as the wave period extends into longer durations. Yaw motion was almost non-existent across all wave directions and periods.

3.2 Structural Response Characteristics and Safety Assessment of Structural Beams

For structural beams, numerical analyses under irregular wave conditions were conducted to determine the maximum values of bending stresses locations that the maximum value occurred. Furthermore, the maximum bending stress was utilized to assess the safety regarding the allowable stress and fatigue life of the multi-linked floating offshore structures. The maximum bending stress values for each wave direction, the element number where maximum bending stress occurred, and the fatigue life for these elements are presented in Table 3. The locations of these elements are presented in Fig. 10. All maximum bending stresses for each wave direction, as

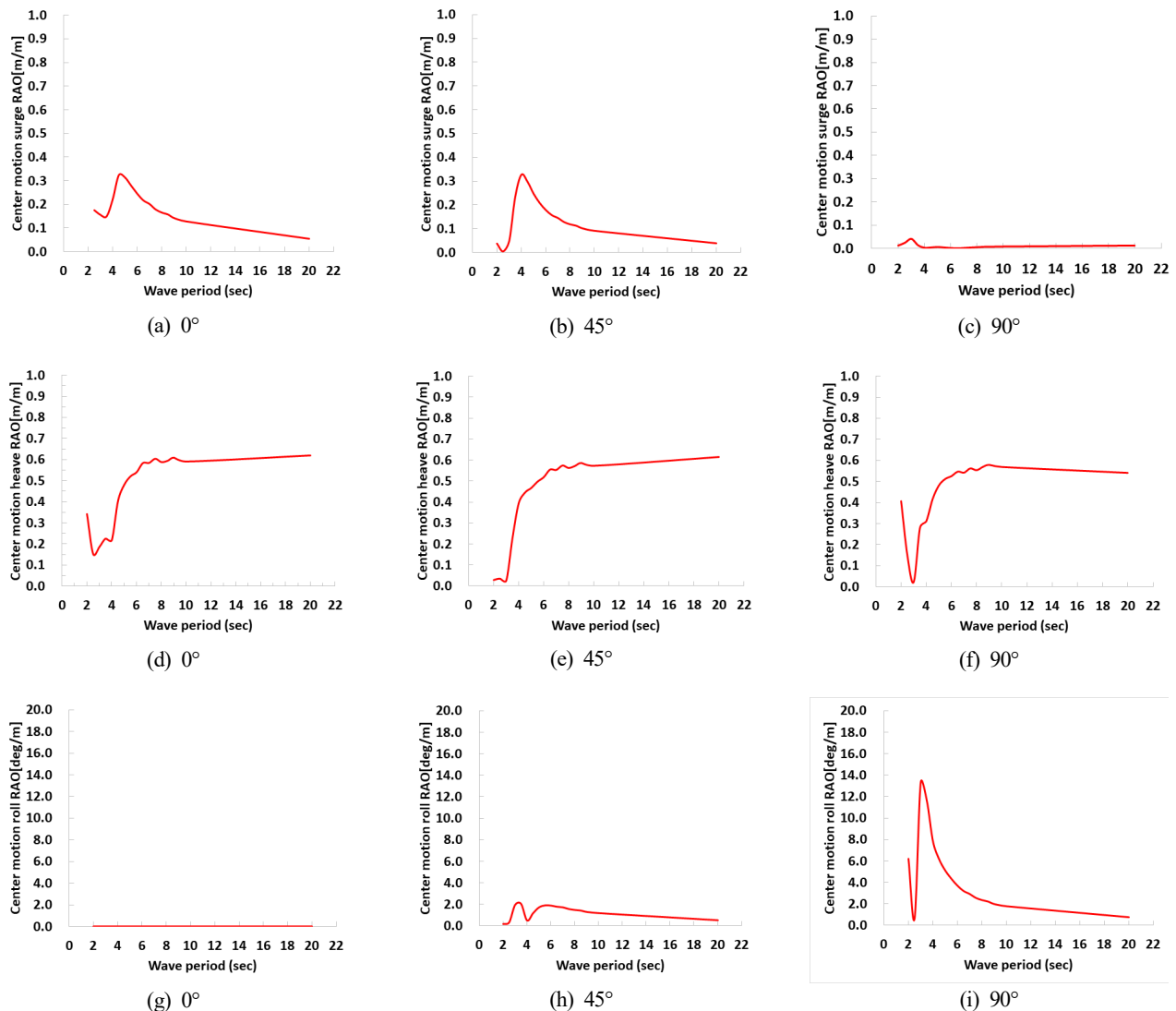


Fig. 9 Motion RAO of multi-linked floating offshore structure

depicted in Fig. 11, are below the allowable stress of 196 MPa for aluminum materials, thus satisfying the allowable stress criteria. For fatigue life calculated with the rain flow counting method from the time history under irregular waves, the results indicated an almost infinite fatigue life well within the 25-year standard. At 0° wave direction, the maximum bending stress was predominantly observed in the longitudinal structural beams located at the edges of the structure where mooring lines are connected. At 45° wave direction, it occurred in the beam structural members adjacent to the connection joints, and in both directions, it was found in the longitudinal structural beams. At 90° wave direction, the maximum bending stress appeared in the transverse structural beams. The smallest maximum bending stress

was at 0° , and the largest at 45° . The lower stress at 0° can be attributed to the greater rotational movement due to the hinged connections compared to other wave directions, affecting the constraint conditions of the beam.

4. Analysis of Effect of Connection Methods on Characteristics of Multi-Linked Floating Offshore Structures

4.1 Influence of Connection Methods Between Unit Structures on Bending Stress

Numerical simulations were conducted under irregular wave conditions progressing in the X direction with varying connection conditions to analyze the structural response characteristics depending on the connection methods at the joints between unit structures of multi-linked floating offshore structures. Three different types of connections were considered: 1) a fixed connection, which constrains all rotational degrees of freedom; 2) a hinge connection, which restricts all rotational freedoms except around the Y-axis; 3) a universal connection, which does not restrict any rotational freedoms. According to the results presented in Fig. 12, the maximum bending stress under fixed connection conditions was 15.6 MPa, approximately 2.5 times higher than the 6.1 MPa recorded under hinge conditions. In the case of a fixed connection, the mooring line tension supports both ends, leading to significant bending stress at the central connection point of the structure. However, for multi-linked floating offshore structures with multiple hinge connections, bending at the center was reduced because of the hinge joints, and greater bending stresses occurred at the ends where the mooring lines directly apply force. With a universal connection, the maximum bending stress was around 5.4 MPa, not significantly different from that under hinge conditions.

Furthermore, in the scenario where rotational freedoms were not constrained, the position of maximum bending stress shifted to near the structural beams connected to the mooring lines at the joint between unit structures, suggesting the necessity of evaluating structural safety at these locations. The observation that bending stress decreases with the application of a hinged joint indicates that wave loads primarily act on the vertical movement of the structure. Furthermore, because the maximum bending stress under unconstrained

Table 3 Maximum bending stress for beam connector

Heading angle	Structural response	
0°	No. element	632
	Max. bending stress (MPa)	6.11
	Fatigue life (year)	Infinite
45°	No. element	398
	Max. bending stress (MPa)	17.42
	Fatigue life (year)	Infinite
90°	No. element	692
	Max. bending stress (MPa)	9.20
	Fatigue life (year)	Infinite

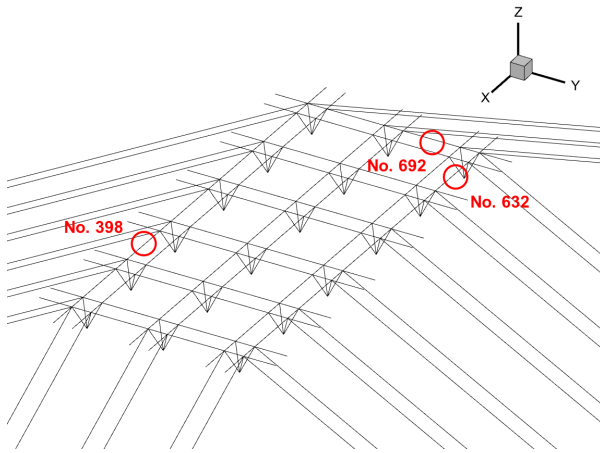


Fig. 10 Position of elements with max. bending stress

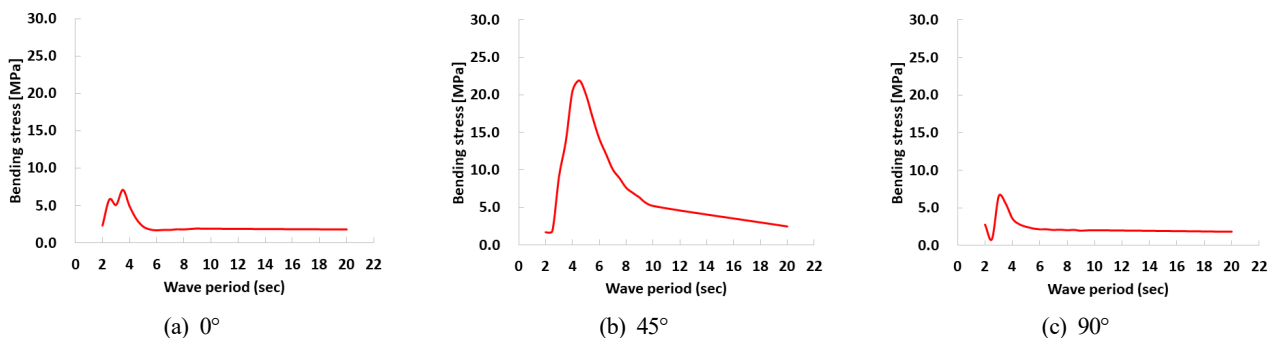


Fig. 11 Bending stress RAO of multi-linked floating offshore structure

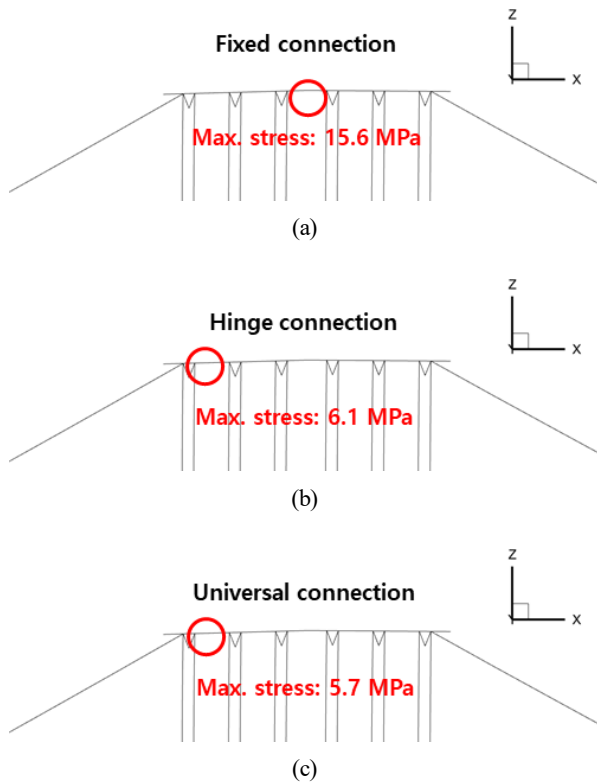


Fig. 12 Maximum bending stress with connection condition: (a) fixed, (b) hinge, and (c) universal connection

rotational freedom differed by less than 10% from that of the hinged joint, it can be inferred that loads acting in the vertical direction do not significantly contribute to the structural response. Consequently, as multi-linked floating offshore structures are extended into large-scale system, the resulting bending stress significantly increases; moreover, by applying connection conditions that do not constrain rotational freedoms at the joints, bending stress can be reduced.

4.2 Influence of Connection Methods Between Unit Structures on Mooring Line Tension

The size and position of maximum mooring line tension were examined to analyze the response of mooring line tension resulting from wave loads for various connection methods between unit structures of multi-linked floating offshore structures, similar to the bending stress analysis. The results indicate that the maximum tension occurs in the mooring lines connected at the frontal side in the X direction; this position remains unchanged despite alterations in the connection method. As presented in Table 4, unlike bending stress, which decreases as the number of constraint on rotational freedoms lessens, the maximum mooring line tension was lowest when all rotational degrees of freedom were constrained, attributed to the reduced deformation of the structure and increased response in rigid body motion, resulting in higher tension in the mooring lines as the number of constraint on rotational freedom decreased. Compared to a maximum tension of 14.2 kN under a fully constrained condition, the tension increased to 16.8 kN, an approximately 18.3% increase, under

Table 4 Maximum bending stress for beam connector

Connection condition	Response	
Fixed	Max. bending stress (MPa)	15.6
	Max. tension (kN)	14.2
Hinge	Max. bending stress (MPa)	6.1
	Max. tension (kN)	16.8
Universal	Max. bending stress (MPa)	5.4
	Max. tension (kN)	17.1

hinge connection conditions. When all rotational freedoms were unconstrained, the tension further increased to 17.1 kN, representing an approximately 20.4% increase. Similar to the case of bending stress, no significant differences were observed between the hinge connection and the condition where all rotational freedoms were unrestricted. Moreover, a change from a fixed connection to a hinge connection increased mooring line tension, unlike the decrease in bending stress, suggesting the necessity to thoroughly review the design tension of the mooring lines when changing the connection method.

5. Conclusion

We conducted a fluid–structure coupled analysis for multi-linked floating offshore structures. Wave loads and hydrodynamic characteristics acting on numerous floating structures were calculated with HOBEM. In addition, a time-domain structural analysis for the multi-linked floating offshore structures and mooring lines was performed using the finite element method. The wave loads were applied as nodal loads in the finite element model, significantly reducing the numerical analysis time. Furthermore, the analysis results were employed to perform a structural safety assessment in terms of allowable stress and fatigue life according to the classification standards, confirming the design's structural integrity. This study varied the connection conditions between the unit structures of the multi-linked floating offshore structures, analyzed response characteristics over different wave load conditions, identifying the size and location of maximum stresses, and reviewed the location and structural response of the structures under each connection condition.

The analysis revealed that the motion and structural RAO of the multi-linked floating offshore structures demonstrate heightened responses from 2.0 to 6.0 s. In the context of the irregular wave modal period between 2.0 and 6.0 s in the target installation area, reviewing the structural integrity is essential. The structural responses of the multi-linked floating offshore structures predominantly occurred in the structural beams connected to the mooring lines, thus necessitating verification of the structural integrity of the beam components at the edges of the structure when the multi-linked floating structure expanded. In addition, the study analyzed the changes in major structural responses, i.e., bending stress and mooring line tension, under different connection conditions between the unit structures. The results indicated that, compared to a fully constrained rotational

freedom scenario (fixed connection), employing hinge connection conditions, which do not constrain the Y-axis rotational freedom, led to an approximate reduction in bending stress by 2.5 times, while the tension in mooring lines due to wave loads increased by approximately 20%.

Furthermore, when all rotational freedoms were unconstrained, the difference in bending stress and mooring line tension compared to hinge connection conditions was negligible, i.e., approximately 0.7 MPa and 0.3 kN, respectively, implying that the sensitivity of the structural response of multi-linked floating offshore structures is predominantly influenced by the Y-axis rotational freedom, which affects heave and pitch motions. Consequently, the structural stress and mooring line tension exhibit an inverse relationship. Changes in structural responses based on the connection method suggest that hinge connection methods can potentially enable higher structural safety in the design of structural beams for large-scale multi-linked floating offshore structures complexes. However, these changes increase tension in the mooring lines, necessitating a thorough safety assessment to develop appropriate designs.

In future research, we plan to analyze and quantify the motion and structural response characteristics induced by the connectors and mooring line tension as the number of unit structures in the multi-linked floating offshore structure increases, particularly focusing on the effect for structures expanded to the scale of large complexes. Furthermore, variations in beam cross-section, length, size of buoyancy bodies, and spacing will be analyzed to understand their influence on the overall system's motion and structural responses. These insights will be instrumental in design for large-scale system utilizing multi-linked floating offshore structures tailored to the installation area's target scale and environmental conditions.

Conflict of Interest

Kangsu Lee serves as a journal publication committee member of the Journal of Ocean Engineering and Technology, but he had no role in the decision to publish this article. No potential conflict of interest relevant to this article was reported.

Funding

This research was supported by a grant from the Endowment Project of "Core Technology Development of Hydro-elasticity Based Structural Damage Assessment for Offshore Structures Considering Uncertainty (4/5)" funded by the Korea Research Institute of Ships and Ocean Engineering (PES4770).

References

Chen, C., Duffour, P., Fromme, P., & Hua, X. (2021). Numerically

- efficient fatigue life prediction of offshore wind turbines using aerodynamic decoupling. *Renewable Energy*, 178, 1421–1434. <https://doi.org/10.1016/j.renene.2021.06.115>
- Ghigo, A., Faraggiana, E., Sirigu, M., Mattiazzo, G., & Bracco, G. (2022). Design and analysis of a floating photovoltaic system for offshore installation: The case study of Lampedusa. *Energies*, 15(23), 8804. <https://doi.org/10.3390/en15238804>
- Kim, H.-S., Kim, B. W., & Lee, K. (2022a). Parametric Study on Effect of Floating Breakwater for Offshore Photovoltaic System in Waves. *Journal of the Computational Structural Engineering Institute of Korea*, 35(2), 109–117. <https://doi.org/10.7734/COSEIK.2022.35.2.109>
- Kim, H., Min, E.-H., Heo, S., & Koo, W. C. (2022b). Motion Analysis of A Wind-Wave Energy TLP Platform Considering Second-order Wave Forces. *Journal of Ocean Engineering and Technology*, 36(6), 390–402. <https://doi.org/10.26748/KSOE.2022.030>
- Kim, B. W., Sung, H. G., Kim, J. H., & Hong, S. Y. (2013). Comparison of linear spring and nonlinear FEM methods in dynamic coupled analysis of floating structure and mooring system. *Journal of Fluid & Structure*, 42, 205–227. <https://doi.org/10.1016/j.jfluidstructs.2013.07.002>
- Kim, H.-S. (2023). *Efficient wave load calculation methods for estimating structural responses of highly numerous floating bodies with connection beams* [Doctoral dissertation, University of Science & Technology].
- Na, K. W., Choo, J. H., & Lee, B. J. (2021). Field performance test of unit platform development for offshore floating photovoltaic power structure. *New & Renewable Energy*, 17(3), 16–23. <https://doi.org/10.7849/ksnre.2021.0012>
- Park, S., & Choung, J. (2023). Structural design of the substructure of a 10 MW floating offshore wind turbine system using dominant load parameter. *Journal of Marine Science and Engineering*, 11(5), 1048. <https://doi.org/10.3390/jmse11051048>
- Song, J.-S., Rim, C. -W., Moon, S.-J. & Nam, Y.-Y. (2014). Effect of initial conditions on transient response in dynamic simulation of FOWT. *Journal of Ocean Engineering and Technology*, 28(4), 288–293. <https://doi.org/10.5574/KSOE.2014.28.4.288>
- Yoon, D. H. & Choung, J. (2023). Collision simulation of a floating offshore wind turbine considering ductile fracture and hydrodynamics using hydrodynamic plug-in HydroQus. *Journal of Ocean Engineering and Technology*, 37(3), 111–121. <https://doi.org/10.26748/KSOE.2023.004>

Author ORCIDs

Author name	ORCID
Sim, Kichan	0000-0002-5933-9805
Lee, Kangsu	0000-0002-9505-6802
Kim, Byoung Wan	0000-0001-7325-1546

Corrigendum to: Investigation of Applying Technical Measures for Improving Energy Efficiency Design Index (EEDI) for KCS and KVLCC2

Jun-Yup Park¹, Jong-Yeon Jung¹ and Yu-Taek Seo²

¹Graduate student, Department of Naval Architecture and Ocean Engineering, Seoul National University, Seoul, Korea

²Professor, Department of Naval Architecture and Ocean Engineering, Seoul National University, Seoul, Korea

Corroendum to: Journal of Ocean Engineering and Technolog, 37(2), 58-67, April, 2023
<https://doi.org/10.26748/KSOE.2023.001>

This corrects the article “Investigation of Applying Technical Measures for Improving Energy Efficiency Design Index (EEDI) for KCS and KVLCC2” in Volume 37 on page 58.

There is an error in Funding section in the article “Investigation of Applying Technical Measures for Improving Energy Efficiency Design Index (EEDI) for KCS and KVLCC2”, and it should be corrected as follows. The authors apologize for any inconvenience this mistake have caused.

Funding

This work was supported by KIMST (Program No. 20220631) funded by the Ministry of Oceans and Fisheries (MOF, Korea).

Author ORCIDs

Author name	ORCID
Park, Junyup	0000-0002-6747-1806
Jeong, Jongyeon	0000-0002-7557-6587
Seo, Yutaek	0000-0001-8537-579X

Received 6 December 2023, revised 7 December 2023, accepted 14 December 2023

Corresponding author Yutaek Seo: +82-2-880-7329, yutaek.seo@snu.ac.kr

© 2023, The Korean Society of Ocean Engineers

This is an open access article distributed under the terms of the creative commons attribution non-commercial license (<http://creativecommons.org/licenses/by-nc/4.0>) which permits unrestricted non-commercial use, distribution, and reproduction in any medium, provided the original work is properly cited.

Instructions for Authors

General information

To submit a manuscript to the Journal of Ocean Engineering and Technology (JOET), it is advised to first carefully read the aims and the scope section of this journal, as it provides information on the editorial policy and the category of papers it accepts. Unlike many regular journals, JOET usually has no lag in acceptance of a manuscript and its publication. Authors that find a match with the aims and the scope of JOET are encouraged to submit as we publish works from all over the world. JOET adheres completely to guidelines and best practices published by professional organizations, including Principles of Transparency and Best Practice in Scholarly Publishing (joint statement by COPE, DOAJ, WAME, and OASPA (<http://doaj.org/bestpractice>) if otherwise not described below. As such, JOET would like to keep the principles and policies of those professional organizations during editing and the publication process.

Research and publication ethics

Details on publication ethics are found in <http://joet.org/authors/ethics.php>. For the policies on research and publication ethics not stated in the Instructions, Guidelines on Good Publication (<http://publicationethics.org/>) can be applied.

Requirement for membership

One of the authors who submits a paper or papers should be member of the Korean Society of Ocean Engineers (KSOE), except a case that editorial board provides special admission of submission.

Publication type

Article types include scholarly monographs (original research articles), technical articles (technical reports and data), and review articles. The paper should have not been submitted to other academic journal. When part or whole of a manuscript was already published to conference papers, research reports, and dissertations, then the corresponding author should note it clearly in the manuscript.

Copyright

After published to JOET, the copyright of manuscripts should belong to KSOE. A transfer of copyright (publishing agreement) form can be found in submission website (<http://www.joet.org>).

Manuscript submission

Manuscript should be submitted through the on-line submission website (<http://www.joet.org>). The date that manuscript was received through on-line website is the official date of receipt. Other correspondences can be sent by an email to the Editor in Chief or secretariat. The manuscript must be accompanied by a signed statement that it has been neither published nor currently submitted for publication elsewhere. The manuscript should be written in English or Korean. Ensure that online submission are in a standard word processing format. Corresponding author must write the manuscript using the JOET template provided in Hangul or MS Word format. Ensure that graphics are high-resolution.

Be sure all necessary files have been uploaded/ attached.

Authors' checklist

Please refer to "Authors' Checklist" for details.

Article structure

Manuscript must be edited in the following order: (1) Title, (2) Authors' names and affiliations, (3) Keywords, (4) Abstract, (5) Nomenclature (optional), (6) Introduction, (7) Main body (analyses, tests, results, and discussions), (8) Conclusions, (9) Conflict of interest, (10) Funding (optional), (11) Acknowledgements (optional), (12) References, (13) Appendices (optional), (14) Author's ORCIDs.

Abstract

A concise and factual abstract is required. The abstract should state briefly the background, purpose and methods of the research, the principal results and conclusions. An abstract should be written in 150-200 words. References are not cited in abstract whenever possible. Also, non-standard or uncommon abbreviations should be avoided, but if essential they must be defined at their first mention in the abstract itself.

Keywords

Immediately after the abstract, provide a maximum of 5 or 6 keywords.

Unit

Use the international system units(SI). If other units are mentioned, please give their equivalent in SI.

Equations

All mathematical equations should be clearly printed/typed using well accepted explanation. Superscripts and subscripts should be typed clearly above or below the base line. Equation numbers should be given in Arabic numerals enclosed in parentheses on the right-hand margin.

Tables

Tables should be numbered consecutively with Arabic numerals. Each table should be fully titled. All tables should be referred to in the texts.

Figures

Figures should be numbered consecutively with Arabic numerals. Each figure should be fully titled. All figures should be referred to in the texts. All the illustrations should be of high quality meeting with the publishing requirement with legible symbols and legends.

Conflict of interest

It should be disclosed here according to the statement in the Research and publication ethics regardless of existence of conflict of interest. If the authors have nothing to disclose, please state: "No potential

conflict of interest relevant to this article was reported.”

Funding

Funding to the research should be provided here. Providing a FundRef ID is recommended including the name of the funding agency, country and if available, the number of the grant provided by the funding agency. If the funding agency does not have a FundRef ID, please ask that agency to contact the FundRef registry (e-mail: fundref.registry@crossref.org). Additional detailed policy of FundRef description is available from <http://www.crossref.org/fundref/>. Example of a funding description is as follows: The study is supported by the Inha University research fund (FundRef ID: 10.13039/501100002632), and the Korea Health Personnel Licensing Examination Institute research fund (FundRef ID: 10.13039/501100003647).

Acknowledgments

Any persons that contributed to the study or the manuscript, but not meeting the requirements of an authorship could be placed here. For mentioning any persons or any organizations in this section, there should be a written permission from them.

References in text

References in texts follow the APA style. Authors can also see how references appear in manuscript text through the ‘Template’.

Reference list

Reference list follows the APA style. Authors can see how references should be given in reference section through the ‘Template’.

Appendices

The appendix is an optional section that can contain details and data supplemental to the main text. If there is more than an appendix, they should be identified as A, B, C, etc. Formulae and equations in appendices should be given separate numbering: Eq. (A1), Eq. (A2), etc.; in a subsequent appendix, Eq. (B1) and so on. Similarly for tables and figures: Table A1; Fig. A1, etc.

ORCID (Open Researcher and Contributor ID)

All authors are recommended to provide an ORCID. To obtain an ORCID, authors should register in the ORCID web site: <http://orcid.org>. Registration is free to every researcher in the world. Example of ORCID description is as follows:

Joonmo Choung: <https://orcid.org/0000-0003-1407-9031>

Peer review and publication process

The peer review process can be broadly summarized into three groups: author process, review process, and publishing process for accepted submissions. General scheme is presented in Figure 1.

Check-in process for review

If the manuscript does not fit the aims and scope of the Journal or does not adhere to the Instructions to Authors, it may be rejected immediately after receipt and without a review. Before reviewing, all submitted manuscripts are inspected by Similarity Check powered by iThenticate (<https://www.crossref.org/services/similarity-check/>), a plagiarism-screening tool. If a too high degree of similarity score is found, the Editorial Board will do a more profound content screening.

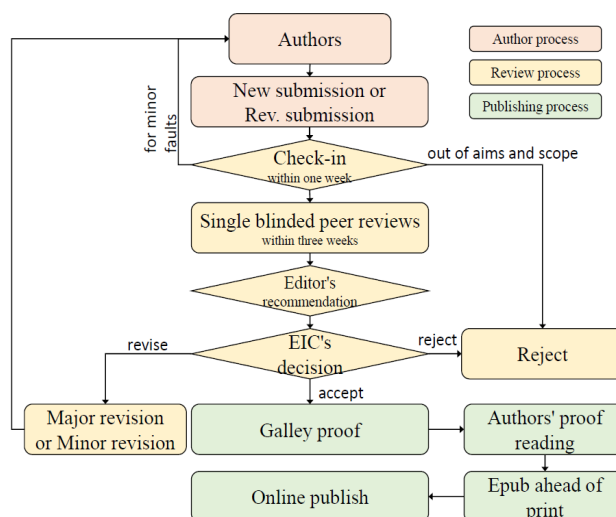


Figure 1 Flow chart of the peer review and publication process of JOET

The criterion for similarity rate for further screening is usually 15%; however, rather than the similarity rate, the Editorial Board focuses on cases where specific sentences or phrases are similar. The settings for Similarity Check screening are as follows: It excludes quotes, bibliography, small matches of 6 words, small sources of 1%, and the Methods section.

Number of reviewers

Reviewers will be selected from the list of reviewers. Manuscripts are then peer reviewed by at least 2 experts in the corresponding field, usually by 2.

Peer review process and the author response to the reviewer comments
JOET adopts single blind review, which means that the authors do not know the identity of the reviews. All papers, including those invited by the Editor, are subject to peer review.

The review period is 4 weeks. Usually the first decision is made within a week after completion of the review. The Editorial Board's decision after the review will be one of followings: Accept, Minor revision, Major revision, or Rejection. The Editorial Board may request the authors to revise the manuscript according to the reviewers' comments. If there are any requests for revision of the manuscript by the reviewers, the authors should do their best to revise the manuscript. If the reviewer's opinion is not acceptable or is believed to misinterpret the data, the author should reasonably indicate that. After revising the manuscript, the author should upload the revised files with a separate response sheet to each item of the reviewer's commentary. The author's revisions should be completed within 3 months after the request. If it is not received by the due date, the Editorial Board will notify the author. To extend the revision period beyond 3 months, the author should negotiate that with the Editorial Board. The manuscript review process can be provided for up two rounds. If the authors wish further review, the Editorial Board may consider it. The Editorial Board will make a final decision on the approval of the submitted manuscript for publication and can request any further corrections, revisions, and deletions of the article text if necessary. Statistical editing is also performed if the data requires professional statistical review by a statistician.

Processing after acceptance

If the manuscript is finally accepted, the galley proof will be sent to the corresponding author after professional manuscript editing and English proofreading. Proofreading should be performed for any misspellings or errors by the authors. Proofreading manuscript for publication is provided to the corresponding author, and the corresponding author must review the proofreading manuscript. Corresponding authors are responsible for the content of the proofreading manuscript and any errors. After final proofreading, the manuscript may appear at the journal homepage as an article in press with a unique DOI number for rapid communication. All published articles will be replaced by the replacement XML file and a final PDF.

Feedback after publication

If the authors or readers find any errors, or contents that should be revised, it can be requested from the Editorial Board. The Editorial Board may consider erratum, corrigendum or a retraction. If there are any revisions to the article, there will be a CrossMark description to announce the final draft. If there is a reader's opinion on the published article with the form of Letter to the editor, it will be forwarded to the authors. The authors can reply to the reader's letter. Letter to the editor and the author's reply may be also published.

How the journal handle complaints and appeals

The policy of JOET is primarily aimed at protecting the authors, reviewers, editors, and the publisher of the journal. If not described below, the process of handling complaints and appeals follows the guidelines of the Committee of Publication Ethics available from: <https://publicationethics.org/appeals>

- Who complains or makes an appeal?

Submitters, authors, reviewers, and readers may register complaints and appeals in a variety of cases as follows: falsification, fabrication, plagiarism, duplicate publication, authorship dispute, conflict of interest, ethical treatment of animals, informed consent, bias or unfair/inappropriate competitive acts, copyright, stolen data, defamation, and legal problem. If any individuals or institutions want to inform the cases, they can send a letter via the contact page on

our website: <https://www.joet.org/about/contact.php>. For the complaints or appeals, concrete data with answers to all factual questions (who, when, where, what, how, why) should be provided.

- Who is responsible to resolve and handle complaints and appeals?

The Editorial Board or Editorial Office is responsible for them. A legal consultant or ethics editor may be able to help with the decision making.

- What may be the consequence of remedy?

It depends on the type or degree of misconduct. The consequence of resolution will follow the guidelines of the Committee of Publication Ethics (COPE).

Article processing charge

Payment due

Article processing charge (APC) covers the range of publishing services JOET provides. This includes provision of online tools for editors and authors, article production and hosting, and customer services. Upon editorial acceptance of an article for the regular review service and upon submission of an article for the fast review service, the corresponding author will be notified that payment is due.

APC

The APC up to 6 pages is ₩300,000 (or \$300) and ₩650,000 (or \$650) for the regular and fast review services, respectively. An extra APC of \$100 per page is charged for papers longer than 6 pages. No taxes are included in this charge. For the fast review service, an advance fee of ₩250,000 (\$250) should be paid on submission.

Payment methods

Credit card payment can be made online using a secure payment form as soon as the manuscript has been editorially accepted. We will send a receipt by email once payment has been processed. Please note that payment by credit card carries a surcharge of 10% of the total APC.

Invoice payment is due within 7 days of the manuscript receiving editorial acceptance. Receipts are available on request.



Title of Article

Firstname Lastname¹, Firstname Lastname² and Firstname Lastname³

¹Professor, Department of OO, OO School, OO University, Busan, Korea

²Graduate Student, Department of OO, OO University, Seoul, Korea

³Senior Researcher, Department of OO, OO Engineering Corp., Seoul, Korea

KEYWORDS: Lumped mass line model, Explicit method, Steel lazy wave riser (Provide a maximum of 5 or 6 keywords.)

ABSTRACT:

****Abstract Construction Guidelines****

- 1) Describe the research background and aims in 1-2 sentences
- 2) Describe the research/analysis method (method section) in 2-3 sentences.
- 3) Describe the research/analysis results (results) in 2-3 sentences.
- 4) Describe the research conclusion in 1-2 sentences.

****Abstract Editing Guidelines****

- 1) Review English grammar.
- 2) Describe in 150-200 words.
- 3) When using an abbreviation or acronym, write the acronym after full words.
- 4) Abbreviations (acronyms) used only once should be written in full words only, and no acronyms.
- 5) References are not included in the abstract.

Nomenclature (Optional)

$ITOC$	Increment of total operating cost (\$/yr)
LHV	Lower heating value (kJ/kg)
P_w	Power (kW)
T	Temperature (K)
V	Volume (m ³)
ρ	Density (kg/m ³)

1. Introduction

The introduction should briefly place the study in a broad context and highlight why it is important. It should define the purpose of the work and its significance. The current state of the research field should be reviewed carefully and key publications cited. Please highlight controversial and diverging hypotheses when necessary. Finally, briefly mention the main aim of the work and highlight the principal conclusions. As far as possible, please keep the introduction comprehensible to scientists outside your particular field of research.

Received 00 February 2100, revised 00 October 2100, accepted 00 October 2100

Corresponding author Firstname Lastname: +82-51-759-0656, e-mail@e-mail.com

It is a recommended paper from the proceedings of 2019 spring symposium of the Korea Marine Robot Technology (KMRTS).

© 2100, The Korean Society of Ocean Engineers

This is an open access article distributed under the terms of the creative commons attribution non-commercial license (<http://creativecommons.org/licenses/by-nc/4.0>) which permits unrestricted non-commercial use, distribution, and reproduction in any medium, provided the original work is properly cited.

2. General Information for Authors

2.1 Research and Publication Ethics

Authorship should be limited to those who have made a significant contribution to the conception, design, execution, or interpretation of the reported study. All those who have made significant contributions should be listed as co-authors. Where there are others who have participated in certain substantive aspects of the research project, they should be acknowledged or listed as contributors.

The corresponding author should ensure that all appropriate co-authors and no inappropriate co-authors are included on the paper, and that all co-authors have seen and approved the final version of the paper and have agreed to its submission for publication.

Details on publication ethics are found in the journal's website (<http://joet.org/authors/ethics.php>). For the policies on research and publication ethics not stated in the Instructions, Guidelines on Good Publication (<http://publicationethics.org/>) can be applied.

2.2 Requirement for Membership

One of the authors who submits a paper or papers should be member of The Korea Society of Ocean Engineers (KSOE), except a case that editorial board provides special admission of submission.

2.3 Publication Type

Article types include scholarly monographs (original research articles), technical articles (technical reports and data), and review articles. The paper should have not been submitted to another academic journal. When part or whole of a manuscript was already published to conference papers, research reports, and dissertations, then the corresponding author should note it clearly in the manuscript.

Example: It is noted that this paper is revised edition based on proceedings of KAOST 2100 in Jeju.

2.4 Copyright

After published to JOET, the copyright of manuscripts should belong to KSOE. A transfer of copyright (publishing agreement) form can be found in submission website (<http://www.joet.org>).

2.5 Manuscript Submission

Manuscript should be submitted through the on-line submission website (<http://www.joet.org>). The date that manuscript was received through on-line website is the official date of receipt. Other correspondences can be sent by an email to the Editor in Chief or secretariat. The manuscript must be accompanied by a signed statement that it has been neither published nor currently submitted for publication elsewhere. The manuscript should be written in English or Korean. Ensure that online submission is in a standard word processing format. Corresponding author must write the manuscript using the JOET template provided in Hangul or MS Word format. Ensure that graphics are high-resolution. Be sure all necessary files have been uploaded/ attached.

2.5.1 Author's checklist

Author's checklist and Transfer of copyright can be found in submission homepage (<http://www.joet.org>).

3. Manuscript

Manuscript must be edited in the following order: (1) Title, (2) Authors' names and affiliations, (3) Keywords, (4) Abstract, (5) Nomenclature (optional), (6) Introduction, (7) Main body (analyses, tests, results, and discussions), (8) Conclusions, (9) Conflict of interest, (10) Funding (optional), (11) Acknowledgements (optional), (12) References, (13) Appendices (optional), (14) Author's ORCID.

3.1 Unit

Use the international system units (SI). If other units are mentioned, please give their equivalent in SI.

3.2 Equations

All mathematical equations should be clearly printed/typed using well accepted explanation. Superscripts and subscripts should be typed clearly above or below the base line. Equation numbers should be given in Arabic numerals enclosed in parentheses on the right-hand margin. The parameters used in equation must be defined. They should be cited in the text as, for example, Eq. (1), or Eqs. (1)–(3).

$$G_{GEV}(x;\mu,\sigma,\xi) = \begin{cases} \exp[-(1+\xi(x-\mu)/\sigma)^{-1/\xi}] & \xi \neq 0 \\ \exp[-\exp(-(x-\mu)/\sigma)] & \xi = 0 \end{cases} \quad (1)$$

in which μ , σ , and ξ represent the location (“Shift” in figures), scale, and shape parameters, respectively.

3.3 Tables

Tables should be numbered consecutively with Arabic numerals. Each table should be typed on a separate sheet of paper and be fully titled. All tables should be referred to in the texts.

Table 1 Tables should be placed in the main text near to the first time they are cited

Item	Buoyancy riser
Segment length ¹⁾ (m)	370
Outer diameter (m)	1.137
Inner diameter (m)	0.406
Dry weight (kg/m)	697
Bending rigidity (N·m ²)	1.66E8
Axial stiffness (N)	7.098E9
Inner flow density (kg·m ³)	881
Seabed stiffness (N/m/m ²)	6,000

¹⁾Tables may have a footer.

3.4 Figures

Figures should be numbered consecutively with Arabic numerals. Each figure should be fully titled. All the illustrations should be of high quality meeting with the publishing requirement with legible symbols and legends. All figures should be referred to in the texts. They should be referred to in the text as, for example, Fig. 1, or Figs. 1–3.

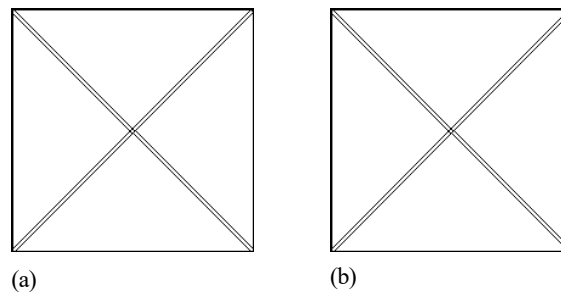


Fig. 1 Schemes follow the same formatting. If there are multiple panels, they should be listed as: (a) Description of what is contained in the first panel; (b) Description of what is contained in the second panel. Figures should be placed in the main text near to the first time they are cited

3.5 How to Describe the References in Main Texts

- JOET recommends to edit authors' references using MS-Word reference or ZOTERO plug-in
- How to add a new citation and source to a document using MS-Word is found in MS Office web page: <https://support.microsoft.com/en-us/office/add-citations-in-a-word-document-ab9322bb-a8d3-47f4-80c8-63c06779f127>
- How to add a new citation and source to a document using ZOTERO is found in zotero web page: <https://www.zotero.org/>

4. Results

This section may be divided by subheadings. It should provide a concise and precise description of the experimental results, their interpretation as well as the experimental conclusions that can be drawn. Tables and figures are recommended to present the results more rapidly and easily. Do not duplicate the content of a table or a figure with in the Results section. Briefly describe the core results related to the conclusion in the text when data are provided in tables or in figures. Supplementary results can be placed in the Appendix.

5. Discussion

Authors should discuss the results and how they can be interpreted in perspective of previous studies and of the working hypotheses. The findings and their implications should be discussed in the broadest context possible. Future research directions may also be highlighted

6. Conclusions

This section can be added to the manuscript.

Conflict of Interest

It should be disclosed here according to the statement in the Research and publication ethics regardless of existence of conflict of interest. If the authors have nothing to disclose, please state: “No potential conflict of interest relevant to this article was reported.”, “The authors declare no potential conflict of interest.”, “The authors declare that they have no conflict of interests.”

Funding (Optional)

Please add: “This research was funded by Name of Funder, grant number XXX” and “The OOO was funded by XXX”. Check carefully that the details given are accurate and use the standard spelling of funding agency names at <https://search.crossref.org/funding>

Acknowledgments (Optional)

In this section you can acknowledge any support given which is not covered by the author contribution or funding sections. This may include administrative and technical support, or donations in kind (e.g., materials used for experiments). For mentioning any persons or any organizations in this section, there should be a written permission from them.

References

JOET follows the American Psychological Association (APA) style.

- Some samples are found in following web pages: <https://apastyle.apa.org/style-grammar-guidelines/references/examples> or <https://www.ntnu.edu/viko/apa-examples>
- JOET recommends editing authors' references using MS-Word reference or ZOTERO plug-in
- How to add a new citation and source to a document using MS-Word is found in MS Office web page: <https://support.microsoft.com/en-us/office/add-citations-in-a-word-document-ab9322bb-a8d3-47f4-80c8-63c06779f127>
- How to add a new citation and source to a document using ZOTERO is found in ZOTERO web page: <https://www.zotero.org/>

Appendix (Optional)

The appendix is an optional section that can contain details and data supplemental to the main text. For example, explanations of experimental details that would disrupt the flow of the main text, but nonetheless remain crucial to understanding and reproducing the research shown; figures of replicates for experiments of which representative data is shown in the main text can be added here if brief, or as Supplementary data. Mathematical proofs of results not central to the paper can be added as an appendix.

All appendix sections must be cited in the main text. In the appendixes, Figures, Tables, etc. should be labeled starting with ‘A’, e.g., Fig. A1, Fig. A2, etc.

Examples:

<https://doi.org/10.26748/KSOE.2019.022>

<https://doi.org/10.26748/KSOE.2018.4.32.2.095>

Author ORCIDs

All authors are recommended to provide an ORCID. To obtain an ORCID, authors should register in the ORCID web site: <http://orcid.org>. Registration is free to every researcher in the world. Example of ORCID description is as follows:

Author name	ORCID
So, Hee	0000-0000-000-00X
Park, Hye-Il	0000-0000-000-00X
Yoo, All	0000-0000-000-00X
Jung, Jewerly	0000-0000-000-00X

Authors' Checklist

The following list will be useful during the final checking of a manuscript prior to sending it to the journal for review. Please submit this checklist to the KSOE when you submit your article.

< Checklist for manuscript preparation >

- ☐ I checked my manuscript has been 'spell-checked' and 'grammar-checked'.
- ☐ One author has been designated as the corresponding author with contact details such as
 - E-mail address
 - Phone numbers
- ☐ I checked abstract 1) stated briefly the purpose of the research, the principal results and major conclusions, 2) was written in 150–200 words, and 3) did not contain references (but if essential, then cite the author(s) and year(s)).
- ☐ I provided 5 or 6 keywords.
- ☐ I checked color figures were clearly marked as being intended for color reproduction on the Web and in print, or to be reproduced in color on the Web and in black-and-white in print.
- ☐ I checked all table and figure numbered consecutively in accordance with their appearance in the text.
- ☐ I checked abbreviations were defined at their first mention there and used with consistency throughout the article.
- ☐ I checked all references mentioned in the Reference list were cited in the text, and vice versa according to the APA style.
- ☐ I checked I used the international system units (SI) or SI-equivalent engineering units.

< Authorship checklist >

JOET considers individuals who meet all of the following criteria to be authors:

- ☐ Made a significant intellectual contribution to the theoretical development, system or experimental design, prototype development, and/or the analysis and interpretation of data associated with the work contained in the article.
- ☐ Contributed to drafting the article or reviewing and/or revising it for intellectual content.
- ☐ Approved the final version of the article as accepted for publication, including references.

< Checklist for publication ethics >

- ☐ I checked the work described has not been published previously (except in the form of an abstract or as a part of a published lecture or academic thesis).
- ☐ I checked when the work described has been published previously in other proceedings without copyright, it has clearly noted in the text.
- ☐ I checked permission has been obtained for use of copyrighted material from other sources including the Web.
- ☐ I have processed Plagiarism Prevention Check through reliable web sites such as www.kci.go.kr, <http://www.ithenticate.com/>, or <https://www.copykiller.org/> for my submission.
- ☐ I agree that final decision for my final manuscript can be changed according to results of Plagiarism Prevention Check by JOET administrator.
- ☐ I checked one author at least is member of the Korean Society of Ocean Engineers.
- ☐ I agreed all policies related to 'Research and Publication Ethics'
- ☐ I agreed to transfer copyright to the publisher as part of a journal publishing agreement and this article will not be published elsewhere including electronically in the same form, in English or in any other language, without the written consent of the copyright-holder.
- ☐ I made a payment for reviewing of the manuscript, and I will make a payment for publication on acceptance of the article.
- ☐ I have read and agree to the terms of Authors' Checklist.

Title of article :

Date of submission : DD/MM/YYYY

Corresponding author :

signature

Email address :

※ E-mail this with your signature to ksoehj@ksoe.or.kr

Publishing Agreement

ARTICLE DETAILS

Title of article :
Corresponding author :
E-mail address :
DOI : <https://doi.org/10.26748/KSOE.2XXX.XXX>

YOUR STATUS

I am one author signing on behalf of all co-authors of the manuscript.

ASSIGNMENT OF COPYRIGHT

I hereby assign to the Korean Society of Ocean Engineers, the copyright in the manuscript identified above and any tables, illustrations or other material submitted for publication as part of the manuscript (the "Article"). This assignment of rights means that I have granted to Korean Society of Ocean Engineers the exclusive right to publish and reproduce the Article, or any part of the Article, in print, electronic and all other media (whether now known or later developed), in any form, in all languages, throughout the world, for the full term of copyright, and the right to license others to do the same, effective when the Article is accepted for publication. This includes the right to enforce the rights granted hereunder against third parties.

SCHOLARLY COMMUNICATION RIGHTS

I understand that no rights in patents, trademarks or other intellectual property rights are transferred to the Journal owner. As the author of the Article, I understand that I shall have: (i) the same rights to reuse the Article as those allowed to third party users of the Article under the CC-BY-NC License, as well as (ii) the right to use the Article in a subsequent compilation of my works or to extend the Article to book length form, to include the Article in a thesis or

dissertation, or otherwise to use or re-use portions or excerpts in other works, for both commercial and non-commercial purposes. Except for such uses, I understand that the assignment of copyright to the Journal owner gives the Journal owner the exclusive right to make or sub-license commercial use.

USER RIGHTS

The publisher will apply the Creative Commons Attribution-Noncommercial Works 4.0 International License (CC-BY-NC) to the Article where it publishes the Article in the journal on its online platforms on an Open Access basis.

The CC-BY-NC license allows users to copy and distribute the Article, provided this is not done for commercial purposes and further does not permit distribution of the Article if it is changed or edited in any way, and provided the user gives appropriate credit (with a link to the formal publication through the relevant DOI), provides a link to the license, and that the licensor is not represented as endorsing the use made of the work. The full details of the license are available at <http://creativecommons.org/licenses/by-nc/4.0/legalcode>.

REVERSION OF RIGHTS

Articles may sometimes be accepted for publication but later rejected in the publication process, even in some cases after public posting in "Articles in Press" form, in which case all rights will revert to the author.

☒ I have read and agree to the terms of the Journal Publishing Agreement.

Corresponding author:

name

signature

※ E-mail this with your signature to ksoehj@ksoe.or.kr (Papers will not be published unless this form is signed and returned)

(사)한국해양공학회 특별회원

한국해양공학회의 특별회원은 다음과 같으며, 귀사의 찬조에 진심으로 감사드립니다.(순서: 입회순)

한국선급 / HD현대중공업(주) / 한화오션(주) / 선박해양플랜트연구소 /
대양전기공업(주) / (주)대영엔지니어링 / 한국조선해양기자재연구원 /
한국조선해양플랜트협회 / (주)파나시아 / 선보공업(주) / SK에코플랜트(주) /
삼성중공업(주) / (주)유에스티21 / (주)해양정보기술 / (주)이앤코 / (주)포스코



한국해양공학회 특별회원 가입방법은 학회홈페이지(www.ksoe.or.kr)의
입회안내를 참고하시고, 기타사항은 학회 사무국으로 연락주시기 바랍니다.

Research and Publication Ethics

Journal of Ocean Engineering and Technology (JOET) adheres to the guidelines published by professional organizations, including Committee on Publication Ethics (COPE; <https://publicationethics.org/>)

1. Authorship

JOET considers individuals who meet all of the following criteria to be authors:

- 1) Made a significant intellectual contribution to the theoretical development, system or experimental design, prototype development, and/or the analysis and interpretation of data associated with the work contained in the article.
- 2) Contributed to drafting the article or reviewing and/or revising it for intellectual content.
- 3) Approved the final version of the article as accepted for publication, including references.

Contributors who do not meet all of the above criteria may be included in the Acknowledgment section of the article. Omitting an author who contributed to your article or including a person who did not fulfill all of the above requirements is considered a breach of publishing ethics.

Correction of authorship after publication: JOET does not correct authorship after publication unless a mistake has been made by the editorial staff.

2. Originality and Duplicate Publication

All submitted manuscripts should be original and should not be in consideration by other scientific journals for publication. Any part of the accepted manuscript should not be duplicated in any other scientific journal without permission of the Editorial Board, although the figures and tables can be used freely if the original source is verified according to the Creative Commons Attribution License (CC BY-NC). It is mandatory for all authors to resolve any copyright issues when citing a figure or table from other journal that is not open access.

3. Conflict-of-Interest Statement

Conflict of interest exists when an author or the author's institution, reviewer, or editor has financial or personal relationships that inappropriately influence or bias his or her actions. Such relationships are also known as dual commitments, competing interests, or competing loyalties. These relationships vary from being negligible to having a great potential for influencing judgment. Not all relationships represent true conflict of interest. On the other hand, the potential for conflict of interest can exist regardless of whether an individual believes that the relationship affects his or her scientific judgment. Financial relationships such as employment, consultancies, stock ownership, honoraria, and paid expert testimony are the most easily identifiable conflicts of interest and the most likely to undermine the credibility of the journal, the authors, or of the science itself. Conflicts can occur for other reasons as well, such as personal relationships, academic competition, and intellectual passion. If there are any conflicts of interest, authors should disclose them in the manuscript. The conflicts of interest may occur during the research process as well; however, it is important to provide disclosure. If there is a disclosure, editors, reviewers, and reader can approach the manuscript after understanding the situation and the background of the completed research.

4. Management Procedures for the Research and Publication Misconduct

When JOET faces suspected cases of research and publication misconduct such as a redundant (duplicate) publication, plagiarism, fabricated data, changes in authorship, undisclosed conflicts of interest, an ethical problem discovered with the submitted manuscript, a reviewer who has appropriated an author's idea or data, complaints against editors, and other issues, the resolving process will follow the flowchart provided by the Committee on Publication Ethics (<http://publicationethics.org/resources/flowcharts>). The Editorial Board of JOET will discuss the suspected cases and reach a decision. JOET will not hesitate to publish

errata, corrigenda, clarifications, retractions, and apologies when needed.

5. Editorial Responsibilities

The Editorial Board will continuously work to monitor and safeguard publication ethics: guidelines for retracting articles; maintenance of the integrity of the academic record; preclusion of business needs from compromising intellectual and ethical standards; publishing corrections, clarifications, retractions, and apologies when needed; and excluding plagiarism and fraudulent data. The editors maintain the following responsibilities: responsibility and authority to reject and accept articles; avoiding any conflict of interest with respect to articles they reject or accept; promoting publication of corrections or retractions when errors are found; and preservation of the anonymity of reviewers.

6. Hazards and human or animal subjects

If the work involves chemicals, procedures or equipment that have any unusual hazards inherent in their use, the author must clearly identify these in the manuscript. If the work involves the use of animal or human subjects, the author should ensure that the manuscript contains a statement that all procedures were performed in compliance with relevant laws and institutional guidelines and that the appropriate institutional committee(s) has approved them. Authors should include a statement in the manuscript that informed consent was obtained for experimentation with human subjects. The privacy rights of human subjects must always be observed.

Ensure correct use of the terms sex (when reporting biological factors) and gender (identity, psychosocial or cultural factors), and, unless inappropriate, report the sex and/or gender of study participants, the sex of animals or cells, and describe the methods used to determine sex and gender. If the study was done involving an exclusive population, for example in only one sex, authors should justify why, except in obvious cases. Authors should define how they determined race or ethnicity and justify their relevance.

7. Secondary publication

It is possible to republish manuscripts if the manuscripts satisfy the conditions of secondary publication. These are:

- The authors have received approval from the Editorial Board of both journals (the editor concerned with the secondary publication must have access to the primary version).
- The priority for the primary publication is respected by a publication interval negotiated by editors of both journals and the authors.
- The paper for secondary publication is intended for a different group of readers
- The secondary version faithfully reflects the data and interpretations of the primary version.
- The secondary version informs readers, peers, and documenting agencies that the paper has been published in whole or in part elsewhere, for example, with a note that might read, "This article is based on a study first reported in the [journal title, with full reference]"
- The title of the secondary publication should indicate that it is a secondary publication (complete or abridged republication or translation) of a primary publication.

8. Complaints and Appeals

The process of handling complaints and appeals follows the guidelines of the COPE available from: <https://publicationethics.org/appeals>

9. Post-publication discussions and corrections

The post-publication discussion is available through letter to editor. If any readers have a concern on any articles published, they can submit letter to editor on the articles. If there found any errors or mistakes in the article, it can be corrected through errata, corrigenda, or retraction.



The Korean Society of Ocean Engineers